Growth And Characterization of Si-Ge-Sn Semiconductor Thin Films using a Simplified PECVD Reactor

by

Jignesh Viresh Vanjaria

A Dissertation Presented in Partial Fulfillment
of the Requirements for the Degree of
Doctor of Philosophy

Approved April 2020 by the
Graduate Supervisory Committee:

Hongbin Yu, Chair
Terry Alford
Arul Chakkaravarthi Arjunan

ARIZONA STATE UNIVERSITY

May 2020

ABSTRACT

The realization of Silicon based photonic devices will enable much faster data transmission than is possible today using the current electronics based devices. Group IV alloys germanium tin (GeSn) and silicon germanium tin (SiGeSn) have the potential to form an direct bandgap material and thus, they are promising candidates to develop a Si compatible light source and advance the field of silicon photonics. However, the growth of the alloys is challenging as it requires low temperature growth and proper strain management in the films during growth to prevent tin segregation. In order to satisfy these criteria, various research groups have developed novel chemical vapor deposition (CVD) reactors to deposit the films. While these reactors have been highly successful in depositing high crystal quality high Sn concentration films, they are generally expensive set-ups which utilize several turbomolecular/cryogenic pumps and/or load-lock systems. An more economical process than the state-of-the art to grow group IV materials will be highly valuable. Thus, the work presented in this dissertation was focused on deposition of group IV semiconductor thin films using simplified plasma enhanced CVD (PECVD) reactors.

Two different in-house assembled PECVD reactor systems, namely Reactor No. 1 and 2, were utilized to deposit Ge, GeSn and SiGeSn thin films. PECVD technique was used as plasma assistance allows for potentially depositing the films at growth temperatures lower than those of conventional CVD. Germane (GeH_4) and Digermane (Ge_2H_6) were used as the Ge precursor while Disilane (Si_2H_6) and tin chloride ($SnCl_4$) were used as the precursors for Si and Sn respectively. The growth conditions such as growth temperature, precursor flow rates, precursor partial pressures, and chamber pressure were varied in a wide range to optimize the growth conditions for the films. Polycrystalline Ge films and SiGeSn films with an Sn content upto 8% were deposited using Reactor No. 1 and 2. Development of epitaxial Ge buffers and GeSn films was accomplished using a modified Reactor No. 2 at temperatures <400°C without the aid of ultra-high vacuum conditions or a high temperature substrate pre-deposition bake thereby leading to a low economic and thermal budget for the deposition process.

ACKNOWLEDGMENTS

I would like to thank my Ph.D. advisor Dr. Hongbin Yu for his guidance and support during my Ph.D. I would like to thank Dr. Arul Chakkaravarthi Arjunan, Dr. Gary Tompa, Mr. Tom Salagaj and everybody at Structured Materials Industries Inc. for providing me the opportunity to work at SMI and for their guidance and help during my internship there. I would like to thank Siddhesh Gajare, Todd Houghton, Haokai Yang, Yanze Wu, Ali Azhar and all my friends and colleagues at ASU for their help and companionship. I would like to thank David Wright, Mark Magnus, Karl Weiss, Tim Karcher, Emmanuel Soignard, Stefan Myhajlenko and the technical staff at ASU for their help and patience whenever I needed assistance using the research facilities. I would like to thank Dr. Terry Alford, Dr. Michael Goryll, Dr. Qing Hua Wang and all the professors at ASU who were kind enough to help me with my research analysis and let me use their research labs. I would like to thank Jenna Snowberger, Sabrina Beck and the office staff for their timely assistance and cheerful conversations. I would like to thank the ASU community for providing a safe and nurturing environment. Lastly, I would like to thank my parents Mr. Viresh Vanjaria and Mrs. Minaxi Vanjaria, family and friends for their love and support.

I would like to gratefully acknowledge that the funding for this dissertation work was provided by the U.S Department of Energy, the National Aeronautics and Space Administration and the National Science Foundation. I would also like to gratefully acknowledge the Eyring Materials Center and the Center for Solid State Electronics Research for the use of the research facilities at Arizona State University.

TABLE OF CONTENTS

Page

LIST OF TABLES

Table Page

LIST OF FIGURES

Figure Page

Figure Page

Figure Page

Figure Page

Figure Page

Figure Page

Figure Page

Chapter 1 Introduction

1.1 Motivation for Group IV thin films

Silicon based technology has been used by industry for fabrication of microelectronic devices since the 1970s. This is exceptional advantages offered by silicon as a material, such as capability to be easily doped, high oxide quality and easy availability. Driven by the ever-increasing demand for computers and smart devices, the microelectronics industry has made tremendous progress, all the way from its advent till the present day (Wirths, Buca, and Mantl 2016). However, as the number of transistors in an integrated microelectronic chip has kept on rising steadily to be keep up with Moore's law, this has led to a dramatic increase in the power consumption by the chips. Furthermore, the passive elements of ICs, such as Cu interconnects, are also identified as source of vast power dissipation via heating. One solution which has been promulgated to counter this issue to replace electrons with photons as the medium of data transfer in the chips. This technology, which is based on the science of light generation, transmission, detection and signal processing, is known as photonics. The devices that are used to source, detect and manipulate light are known as optoelectronic devices. These devices generally include electrical-to-optical transducers, optical-to-electrical transducers and optical waveguides. The development of a single material system which can be used for both electronic and photonic devices will help realize the ultimate vision of the reduction of power consumption for the next generation of integrated chips.

However, the indirect bandgap of Si limits its' application in optoelectronic devices. As a result, researchers are looking into different approaches to monolithically grow these devices on Si. One such approach is the growth of direct bandgap III-V materials on Si. III-V materials offer a huge potential due to their exceptionally electron mobility. The main challenge of this approach is incompatibility of growth with the current complementary metal oxide semiconductor (CMOS) processing. Since the current CMOS technology is based around silicon, developing optoelectronics devices employing a group IV material system would be highly advantageous and economical, as it could readily be integrated with the current chip processing technology. Optoelectronic devices which are based on silicon (Si) and germanium (Ge) are known as Group IV photonics. The realization of photonic devices in group-IV semiconductors will create a wealth of opportunities in the areas of free space communication, thermal and biomedical imaging, optical sensing, chemical spectroscopy, astronomy and military applications such as missile guidance and countermeasures (Thomson et al. 2015; Huang et al. 2011).

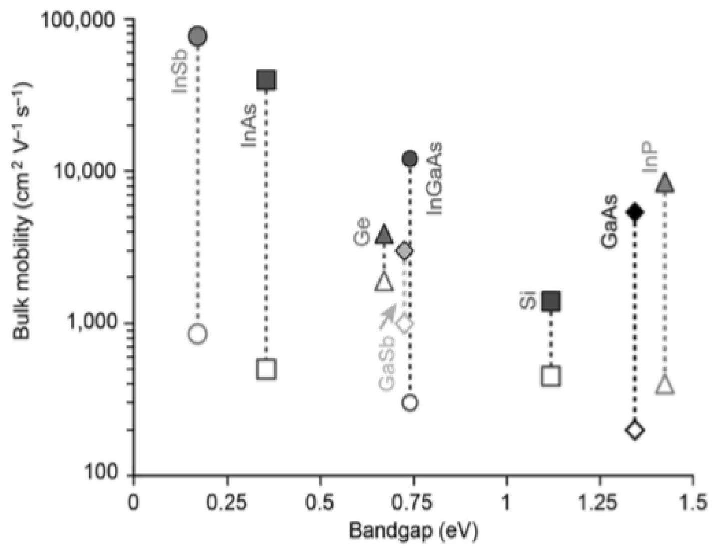

FIG. 1.1.1. Bulk Carrier mobility as a function of bandgap for common semiconductor materials

Germanium is an important semiconducting material for accomplishing the goal of electronic–photonic integration on the silicon platform. Germanium has several attractive features such as higher carrier mobility than Si, a pseudo direct bandgap (the direct Ge Γ-valley is only 136 meV higher than the indirect L-valley), longer cut-off wavelength than Si (at 1.55 μm) and compatibility with well-developed silicon CMOS processing technology. Germanium thin films can be fabricated to act as passive components such as waveguides and amplifiers in integrated photonic circuits. Ge thin films also act as buffers for the growth of group IV alloys such as GeSn and SiGeSn on Si substrates to counter the issue of the large lattice mismatch between the alloys and Si substrate. These group IV alloys can then be bandgap and lattice engineered by varying the composition of the alloys to achieve active photonic components such as light emitting diodes, lasers and detectors. Thus, the heteroepitaxial growth of Ge on Si is a crucial step and improvement in germanium growth and processing can impact a lot of different fields such opto-electronics, fiber optics and photovoltaics.

However, similar to Si, Ge is also an indirect bandgap semiconductor, with a bandgap at 0.67 eV. Thus, optoelectronic devices based on pure Si or Ge would result in low efficiency and poor performance (Fischer et al. 2015; von den Driesch et al. 2017; Chang, Chang, and Chuang 2010). While techniques such as heavy n – doping or strain engineering can be employed to convert Ge into a pseudo direct band gap material, these techniques are expensive and time-consuming (Camacho-Aguilera et al. 2012). Thus, substantial research effort has been dedicated in the past decade to developing group IV semiconductor alloys for applications in photonics (Harris et al. 2014).

Amongst the material systems being looked into, germanium tin (GeSn) and silicon germanium tin (SiGeSn) alloys are appearing as one of the most promising candidates for photonic circuits. The Si–Ge–Sn system with its two degrees of freedom for strain engineering, namely, alloying and strain, might provide a Si-based material platform for both n- and p-MOSFETs that is CMOS compatible, hence, suitable for large-scale and low-cost integration (Roucka et al. 2015; Zheng et al. 2015). This is due to the fact that with these alloys, there is a possibility of achieving a fundamental direct bandgap in a group IV semiconductor. Ge only has a small difference of 140 meV between the direct and indirect bandgap (Fournier-Lupien et al. 2014; Attiaoui and Moutanabbir 2014; Moontragoon, Soref, and Ikonic 2012). The group IV element α-Sn is a semimetal with an inverted band structure i.e. the conduction and valence bands are bent downwards and upwards, respectively. This electronic band structure with a negative bandgap of -0.41 eV at the center of the Brillouin zone differs significantly from those of other group IV elements Si or Ge.

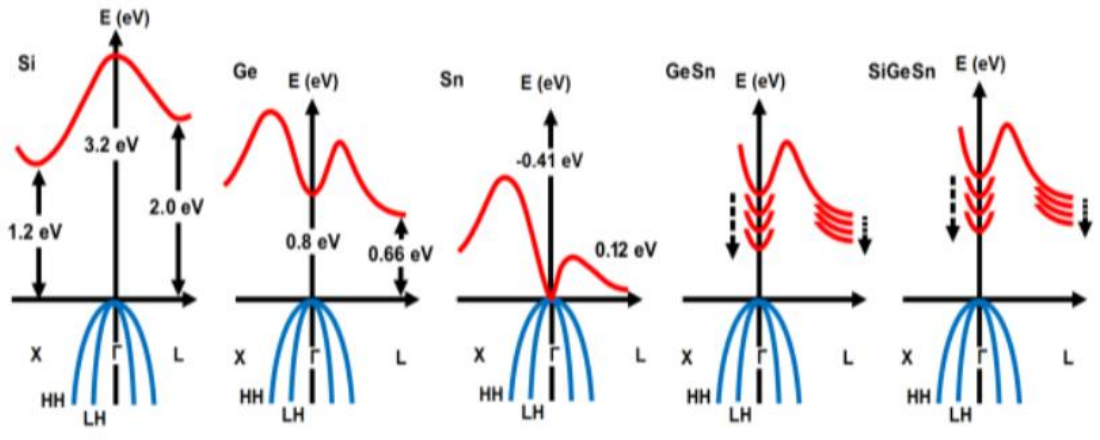

FIG. 1.1.2. Electronic band diagrams of group IV elements Si, Ge and Sn and of Group IV alloys GeSn and SiGeSn showing transition from indirect to direct bandgap

Thus, alloying Ge with Sn causes Γ valley to reduce faster than the L valley thereby reducing the difference between the indirect and direct bands and leading to a transition from indirect to direct bandgap semiconductor above certain Sn percentages. Accordingly, Sn containing group IV materials such as GeSn and SiGeSn open the pathway for efficient on-chip integration of photonics and electronics. Consisting entirely of group IV elements, the alloys have the capability to expand the field of group IV optoelectronics via band gap and strain engineering. The band gap of the alloy can be varied in a wide range (at present from 0.6 eV to 1.1 eV) and also be switched from indirect to direct with the appropriate concentration of Si and Sn. The band gap of this material can then be calculated using the following expression provided by Ranjan (2016).

$$E_{i\_Si_xGe_ySn_z} = E_{i\_Si} * x + E_{i\_Ge} * y + E_{i\_Sn} * z - b_{SiGe} * x * y - b_{GeSn} * y * z - b_{SiSn} * x * z \text{.....(1)}$$

Where E_i is the band gap of the material at the critical points (Γ, L or X), b is the bowing parameter for the binary alloy and x, y, z are the fraction of Si, Ge and Sn in the thin film respectively.

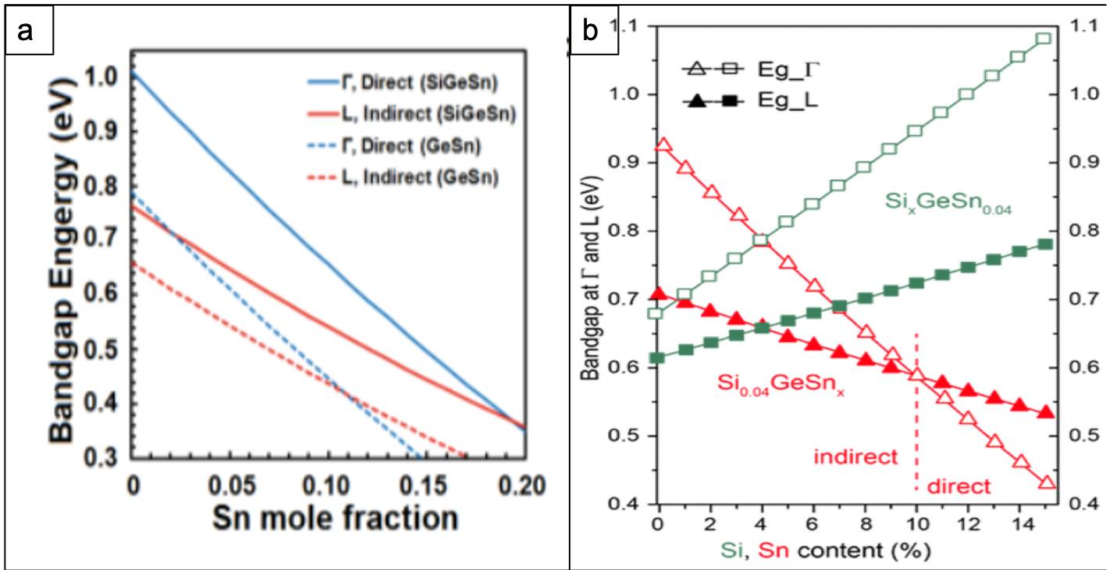

FIG. 1.1.3. Bandgap energies for GeSn and SiGeSn alloys as a function of the Sn and Si concentrations

Figure 1.1.3 shows the change in the Γ and L bandgap of GeSn and SiGeSn for different as a result of increase in the Sn incorporation. For GeSn alloys, the cross over from indirect to direct bandgap occurs at ~0.6eV with a Sn concentration of ~10%. Thus, the binary alloy can be employed for fabrication of devices in the mid-infra-red region i.e. 3-5 μm. Addition of Si with a direct bandgap of 3.2 eV to the alloy enables SiGeSn alloy with a higher direct bandgap energy. Thus, the ternary alloy becomes useful for application in the near infra-red region i.e. 2-3 μm. Also, the lattice constant of the alloys can be engineered independent of the bandgap energy (Zaima et al. 2015; Wirths et al. 2014; Asano et al. 2015; Beeler et al. 2012). The alloys also exhibit several other appealing features such as higher carrier mobility compared to silicon, and the potential to be grown lattice matched to various substrates, acting as the active layer or as a buffer layer. Additionally, the ternary SiGeSn exhibits an enhanced thermodynamic stability relative to the binary analogues due to its increased mixing entropy from the Sn and Si content (Aella et al. 2004; Jiang et al. 2014; Xie et al. 2010; Aboozar Mosleh, Alher, Cousar, et al. 2016). Thus, the group IV alloys GeSn and SiGeSn can be used to design a multitude of optoelectronic devices including broad-range photodetectors, light sources, quantum cascade lasers, solar cells, photodiodes, and transistors (Du et al. 2016; Roucka et al. 2016; Soref 2014; Schulte-Braucks et al. 2016). In fact, the binary Ge1-xSnx alloys have been investigated and demonstrated in device applications. For example, Ge1-xSnx films with Sn incorporation of 12.6% and 9.0% have been demonstrated to provide lasing at temperatures ≤ 90K and 110K, respectively, with relatively low threshold voltage. While the photonic applications of Group IV alloys requires epitaxial growth of the material, polycrystalline thin films of the semiconductors are also useful for diverse applications. Polycrystalline GeSn and SiGeSn thin films have demonstrated higher carrier mobility than crystalline Si and are thus being researched for use in thin film transistors and tandem solar cells (Takeuchi et al. 2015; Moto et al. 2019; Ohmura et al. 2015). Polycrystalline SiGeSn thin films have also displayed low thermal conductivity values and thus are a promising candidate for use in thermoelectric generators (Takahashi et al. 2019; Peng et al. 2019). Thus, the growth of polycrystalline SiGeSn is also worth exploring.

1.2 Growth Techniques for Group IV thin films

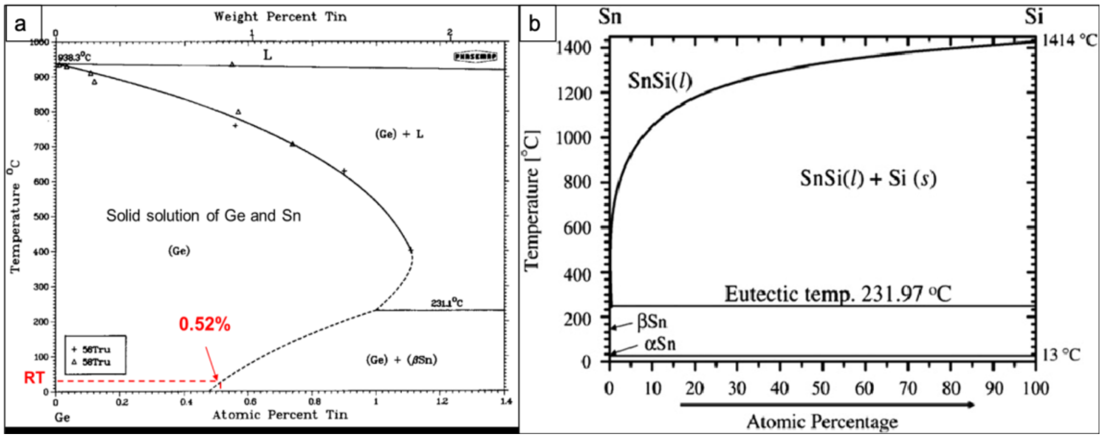

FIG. 1.2.1. Phase diagrams for (a) Ge-Sn and (b) Si-Sn binary systems showing low solubility of Sn in Si and Ge

There are several issues that arise in the deposition of GeSn and SiGeSn thin films. The first issue is the lattice mismatch between elemental Si, Ge and Sn. The lattice constant of Sn is 6.493 Å compared to 5.658 Å of Ge and 5.431 Å of Si, that is 14.7% to Ge and even 19.8% to Si (Wirths, Buca, and Mantl 2016). This hampers the growth of smooth and high-quality Si–Ge–Sn alloys since so-called Stranski–Krastanov (SK) or 3D growth mode occurs. The 3D growth mode starting right after the wetting layer (a few 2D monolayers) results in severe surface roughening just as in the case of Ge heteroepitaxy on Si(001) with a lattice mismatch of 4.2%. As a result, the deposited films turn polycrystalline or amorphous after exceeding a critical epitaxial thickness. The second major issue is the low solubility of α-Sn in Ge and Si. The thermodynamic solubility of Sn in Ge is approx. 1.1 at.% and decreases below 1 at.% toward the eutectic temperature (231.1 °C) while it is 0.1% in Si at room temperature as shown in the phase diagrams in

Fig 1.2.1. Thus, the Sn solubility in the alloy significantly decreases with increasing Si concentration within the alloy. The third major issue is that the semiconducting form of tin (i.e. α-Sn) is unstable at room temperature and phase transforms into the metallic form (i.e. β-Sn). Because of the low solubility and the instability of α-Sn, Sn tends to precipitate out of the epilayer passing through a phase transition from its semiconducting so-called α-Sn (gray tin) phase with diamond cubic lattice structure to a metallic phase (β-Sn or white tin) with a body-centered tetragonal structure and segregate at the surface during growth or thermal processing. Thus, non-equilibrium growth techniques along with a low temperature process have to be employed to deposit GeSn and SiGeSn thin films with Sn concentrations which exceed the solid solubility in Ge or SiGe and which are scientifically and technologically relevant.

Diverse approaches have been used to grow SiGeSn thin films, such as such as pulsed laser deposition, sputtering, molecular beam epitaxy and chemical vapor deposition. The first monocrystalline and single phase GeSn epilayers were grown via bias sputtering deposition on Ge(100) and GaAs(100) with Sn concentrations up to 15 at.% in diamond structured polycrystalline GeSn and a maximum Sn content of 8 at.% in single crystal layers. SiGeSn thin films with Sn content upto 10% have been deposited using magnetron sputtering at a temperature of 150^{o}C (Zheng et al. 2015). The films were observed to be thermodynamically stable upto temperatures as high as 500^{o}C during post deposition annealing. Pulsed laser induced epitaxy has been used to deposit GeSn and SiGeSn epitaxial films with graded composition on Si substrate achieving a maximum tin content of 1% (Stefanov et al. 2012). Different levels of intermixing have been achieved by varying the number of laser pulses. However, a high Sn content has not yet been achieved using this technique. However, the highest material quality films achieved have been obtained by using MBE and CVD techniques. For MBE, both solid source and gas source methods have been used by different groups to deposit GeSn and SiGeSn thin films (Fischer et al. 2015; Asano et al. 2015; Shimura et al. 2017; Talochkin et al. 2017). Initial attempts to deposit GeSn films with conventional thermal MBE resulted in polycrystalline, diamond lattice structured GeSn with a Sn concentration of <30% at a growth temperature of 170^{o}C. Ion assisted MBE enabled the growth of pseudomorphic Ge1-xSnx epilayers on Ge with $0.035 < x < 0.115$ and layer thicknesses between 50 nm and 200 nm. SiGeSn epitaxial layers with Sn content of 4-15% and Si content of 20-45% have also been reported by MBE technique. Growth temperatures of 100-250^{o}C were employed during these processes. However, while MBE offers the advantage of low growth temperature and better composition control, CVD is the technique most commonly used currently to deposit SiGeSn thin films. This is because the low growth temperatures in MBE results in limited layer thicknesses while CVD offers various advantages such as high growth rates, possibility of selective growth and uniform deposition over large scale wafers in a cost effective manner.

For the deposition of Si–Ge–Sn alloys, very low growth temperatures are required where the rate is governed by surface reactions on the surface of the substrate; this growth regime is called *kinetic growth regime*. Since deposition occurs at low temperature, the film growth rate and achieved composition strongly depend on the process parameters such as precursor flow rates, temperature and pressure. The growth kinetics also depend on the design of the CVD tool employed to grow the group IV films.

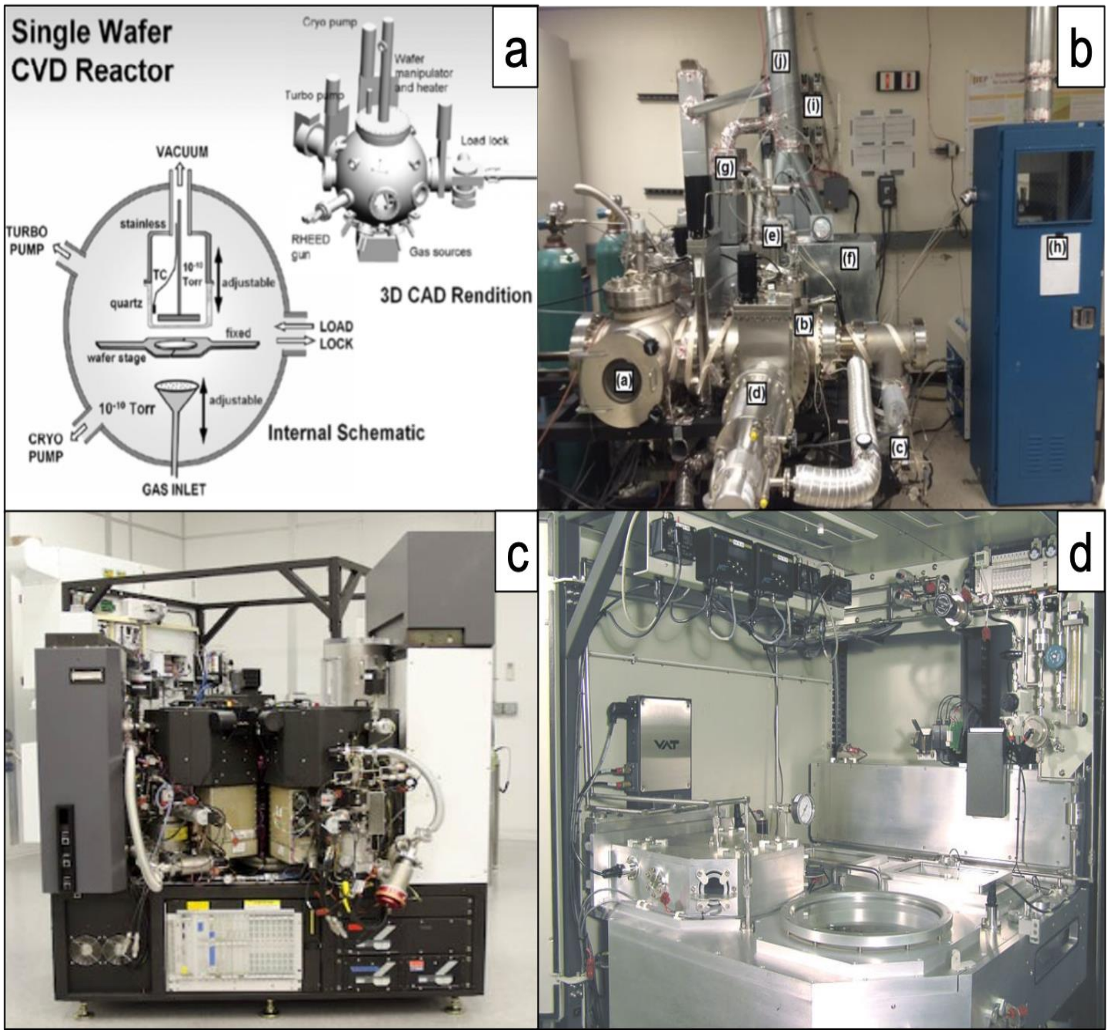

FIG. 1.2.2. CVD growth reactor for deposition of Group IV thin films developed by (a) Arizona State University (b) University of Arkansas (c) Applied Materials (d) ASM

By choosing and precisely controlling the appropriate growth parameters in different types of CVD reactors, several groups have succeeded in growing metastable, supersaturated intrinsic and doped GeSn and SiGeSn alloys on Si(001), Ge(001) substrates as well as on Ge- or GeSn- virtual substrates. Initial attempts to deposit group

IV thin films were initiated by researchers at Arizona State University. They developed a hot wall ultra-high vacuum CVD system to deposit the films using higher order silanes and germanes along with stannane (SnD_4) as the precursors for Si, Ge and Sn (Bauer et al. 2003; Gallagher et al. 2013; D’Costa et al. 2007). Sn-hydride precursors could not have been employed, owing to the low Sn-H bond energy making these precursors unstable at room temperature. Starting with GeSn films with 3% Sn using Ge_2H_6 and SnD_4 precursors, films with >10% Sn were eventually attained using Ge_3H_8 and SnD_4 precursors and a Ge virtual substrate. The first growth of SiGeSn ternaries was also enabled by using GeSn/Si(001) buffers under UHV conditions and a precursor combination of SiH_3GeH_3 and SnD_4. In order to grow on Si(001) directly and on Ge-VS a novel precursor combination had to be introduced, namely $SnD_4/Ge_2H_6/Si_3H_8$ and at low growth temperatures $SiGeH_6$ was added to fine-tune the Si concentration. Post this, efforts were made to use silane, germane and tin chloride ($SnCl_4$) instead of the higher order gases to lower the economical budget of the process. These efforts have recently proved successful by the design and utilization of unique CVD reactors, such as cold wall ultra-high vacuum CVD (as demonstrated by researchers at University of Arkansas), reduced pressure CVD systems (as demonstrated by research groups from Germany and Canada) and atmospheric pressure CVD systems (Aboozar Mosleh, Alher, Du, et al. 2016; Alharthi et al. 2017; Wirths et al. 2014; Attiaoui and Moutanabbir 2014). By careful control of the growth parameters such as substrate temperature and input precursor gas flow rates, GeSn and SiGeSn films have been successfully deposited on Si and Ge substrates. Films with Sn % as high as 20% have been deposited using techniques such as composition graded deposition. High quality deposition has been obtained by using chamber pressures ranging from 10^{-7} to 1 bar and substrate temperature ranging from 250 to 475^{o}C and a wide variety of precursors. Because of the achievements in Si–Ge–Sn CVD in the past 2 decades, these alloys now represent a novel and technologically relevant material platform for Si photonics and microelectronics.

The reactors employed by the previous mentioned research groups are generally expensive set-ups which utilize several turbomolecular/cryogenic pumps (to achieve a low background pressure) and/or load-lock systems. Also, techniques such as exotic precursors (like higher-order hydrides) and high temperature pre-deposition substrate is employed to attain high film growth rates and low defect densities in the films. However, these techniques invariably lead to increase in the economical and thermal budget, and therefore cost of fabrication. A more economical reactor which can deposit group IV thin films and does not require expensive parts would be highly beneficial. Additionally, plasma enhanced CVD (PECVD) has not yet been explored thoroughly for the deposition of Group IV alloys. Use of PECVD can prove beneficial as it allows for potentially depositing the films at a lower substrate temperature and faster deposition rates as compared to other techniques by providing additional energy for precursor bond dissociation through collisions with plasma ions. Thus, in this dissertation, simplified PECVD reactors were assembled in-house and used to deposit group IV semiconductors. Germane (GeH_4) and Digermane (Ge_2H_6) were used as the Ge precursor while Disilane (Si_2H_6) and tin chloride ($SnCl_4$) were used as the precursors for Si and Sn respectively. The growth conditions were optimized to vary the composition of the deposited thin films.

1.3 Outline of Dissertation

The goal of this dissertation is to provide a foundation for a low cost thin film deposition technology to enable PECVD of Group IV semiconducting materials. In Chapter 2, the chemical vapor deposition systems that were used to grow the materials are explained. Two different reactor systems were assembled to deposit the group IV materials: Reactor No. 1 and Reactor No. 2 with the second one being an updated system of the first one based on the results obtained from the growth runs preformed using the first system. In Chapter 3, plasma enhanced CVD growth of polycrystalline SiGeSn thin films using Reactor No. 1 is presented. In Chapter 4, growth and characterization of polycrystalline Ge and GeSn films using Reactor No.2 are presented. Chapter 5 discusses the growth and characterization of epitaxial Ge and GeSn thin films achieved using a modified Reactor No. 2. Simulation results for Ge and GeSn based devices done using Silva Atlas for thickness and composition optimization purposes are presented in Chapter 6. The conclusion and future work of this research are presented in Chapter 7.

Chapter 2 PECVD reactors used for material deposition

Two different deposition systems were used in this research for the growth of Si-Ge-Sn materials: Reactor No. 1 and Reactor No. 2. Reactor No. 2 was modified in later stages to achieve epitaxial growth of Group IV films. The reactors were designed and assembled at Stuctured Materials Industries Inc. The details of each system are discussed in the following sections.

2.1 Reactor No. 1 design and film growth procedure using Reactor No. 1

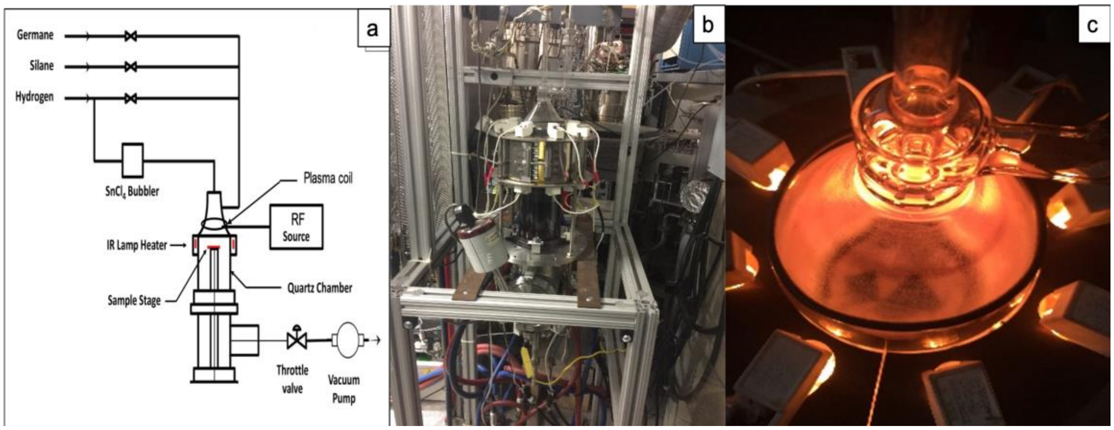

FIG. 2.1.1. (a) Schematic and (b) Photograph of Reactor No.1 assembly. (c) Photograph of susceptor being heated by IR lamp apparatus

Reactor No. 1 consists of a cylindrical quartz reactor (with two inlets at the top for the precursors), a gas delivery system and a vacuum exhaust system connected through flanges. The quartz chamber had a 3 inch inner diameter and was 1 and a half feet in length. The substrates for film deposition were placed on a circular molybdenum susceptor within the quartz chamber. The susceptor was 2 and a inch diameter and 1 inch thick. It could hold silicon wafer upto 2 inch in dimension. Once the substrates had been placed on the susceptor, the bottom flange was attached and the chamber was then evacuated with the use of a mechanical pump. The mechanical pump was a rotary vane pump boosted by a roots blower pump. It could pump the chamber down to a background pressure of $1*10^{-2}$ Torr. The pumping rate achieved with the mechanical pump is in the range of 750-850 cm^3/sec (this was calculated by measuring the time taken for the chamber pressure to drop from 100 Torr to 0.5 Torr). Once adequate vacuum was established in the growth chamber, the susceptor was heated using an infra-red (IR) lamp heating arrangement. 8 lamps arranged in a circle around the susceptor were used for heating. The susceptor temperature was measured using external pyrometers. Once the desired film deposition temperature had been reached, the precursors were introduced into the reactor through the gas inlets. The Si and Ge precursor gases were delivered from the gas cabinet to the reactor chamber using quarter inch pipes. The flow of the precursor gases to the quartz chamber was controlled using mass flow controllers calibrated for each gas. As $SnCl_4$ is a liquid at room temperature, a bubbler system was designed such that a carrier gas bubbles through the liquid and transports the vapors of $SnCl_4$ to the chamber. Plasma was generated in the chamber during film growth using a plasma induction copper wire wrapped around the quartz chamber powered by a 250kHz 1kW RF power source. The schematic and picture of the reactor are shown in Fig 2.1.1.

2.2 Reactor No. 2 design and Film growth procedure using Reactor No. 2

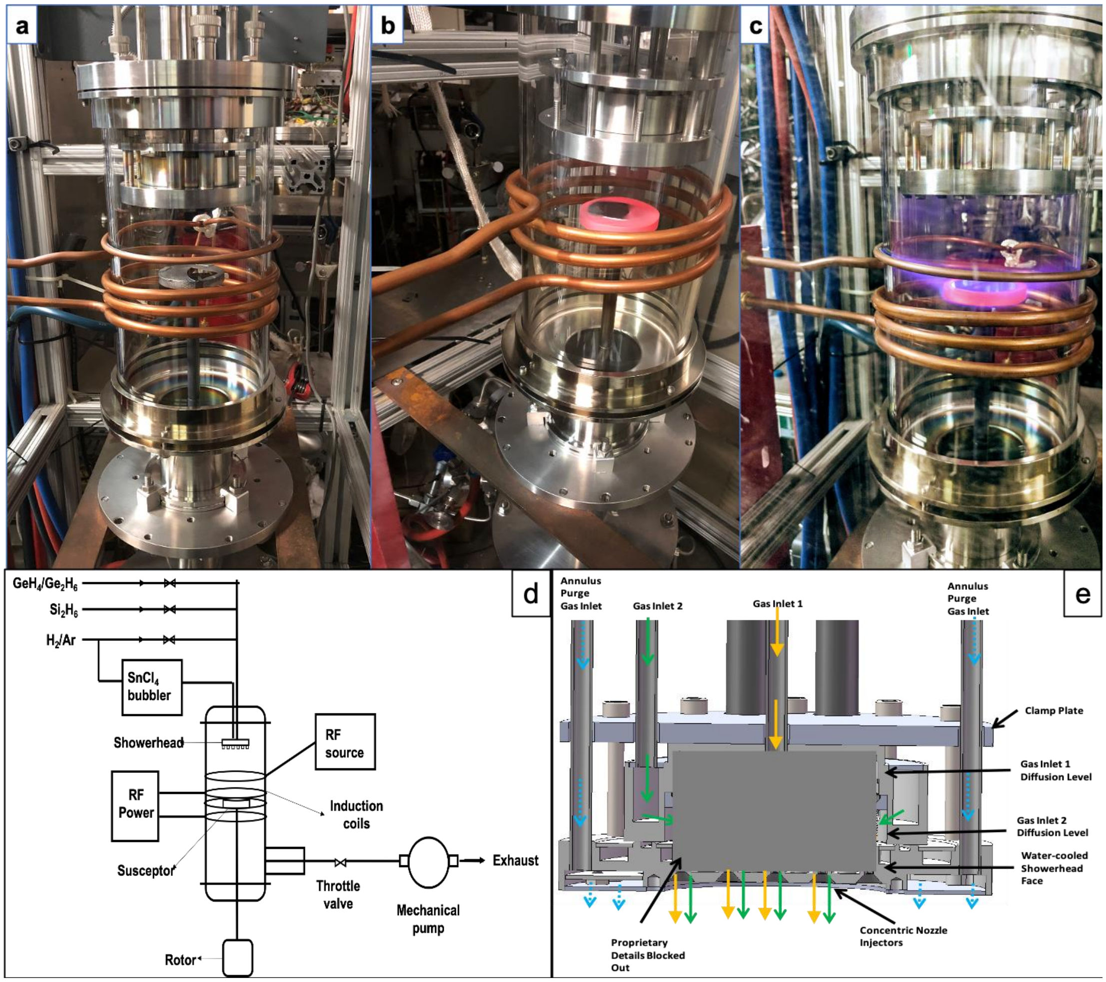

FIG. 2.2.1. Photographs of (a) Reactor No. 2 assembly (b) Susceptor being heated using induction heating (c) Plasma generated in the chamber using induction plasma. Schematics of (d) Reactor No.2 assembly (e) Industrial showerhead installed in Reactor No. 2

Reactor No. 2 consists of a cylindrical quartz reactor, a gas delivery system and a vacuum system connected through flanges. The quartz cylinder is 317.5 mm in length and has a diameter of 140 mm. The substrates for film deposition were placed on a molybdenum susceptor within the reactor. The susceptor was 2 and a inch diameter and 1 inch thick. It could hold silicon wafer upto 2 inch in dimension. The susceptor was connected to a molybdenum shaft was in turn was connected to a rotor assembly. The susceptor could be rotated up to speeds of 1000 rpm using the rotor assembly. After placing the substrates on the susceptor, the flanges were clamped to the quartz chamber. The reaction chamber was then pumped down mechanical pump. The mechanical pump was a rotary vane pump boosted by a roots blower pump. It could pump the chamber down to a background pressure of $1*10^{-2}$ Torr. Once adequate vacuum has been established in the reactor, the susceptor was heated using induction heating. For induction, one inch diameter copper coils were wrapped around the quartz chamber outside the susceptor and current was flown through the coils using an external RF power supply. The induction heating confined the heating to the susceptor and avoids heating of the other parts of the reactor limiting the degassing from other parts. The substrate temperature was measured using an external pyrometer and it was controlled by varying the RF power to the induction coils. Once the desired temperature had been reached, the precursors were introduced into the reactor through an industrial design showerhead. The partial pressure of the precursor is varied either by changing the precursor flow or carrier gas flow rates as required. The Si and Ge precursor gases were delivered from the gas cabinet to the reactor chamber using quarter inch pipes. The flow of the precursor gases to the quartz chamber was controlled using mass flow controllers calibrated for each gas. As $SnCl_4$ is a liquid at room temperature, a bubbler system was designed such that a carrier gas bubbles through the liquid and transports the vapors of $SnCl_4$ to the chamber. Plasma was generated in the chamber during film growth using a plasma induction copper quarter inch pipe wrapped around the quartz chamber powered by a 250kHz 1kW RF power source. The induction and plasma copper pipes were cooled by flowing cold water through them so as to prevent their overheating during susceptor heating and film deposition. The schematic and picture of the reactor are shown in Fig 2.2.1.

Table 2.2.1. Salient differences between Reactor No. 1 and Reactor No.2 for the deposition of SiGeSn films

No.	Reactor No. 1	Reactor No. 2
1	3” inner diameter	5.75” inner diameter
2	Hydride and alkyl flows introduced separately in chamber	Hydride and alkyl flows being mixed in showerhead before being introduced in chamber
3	IR heating by lamp	Induction heating by induction coils
4	No susceptor rotation	Susceptor rotation present
5	Thin copper wire for induction plasma generation	Hollow copper coil with water cooling for induction plasma generation

2.3 Film growth procedure using modified Reactor No. 2

In order to deposit films epitaxially on Si substrates, the vacuum system of Reactor No. 2 was modified by attaching a turbomolecular pump to further decrease the background pressure in the growth chamber. This was done to reduce the background

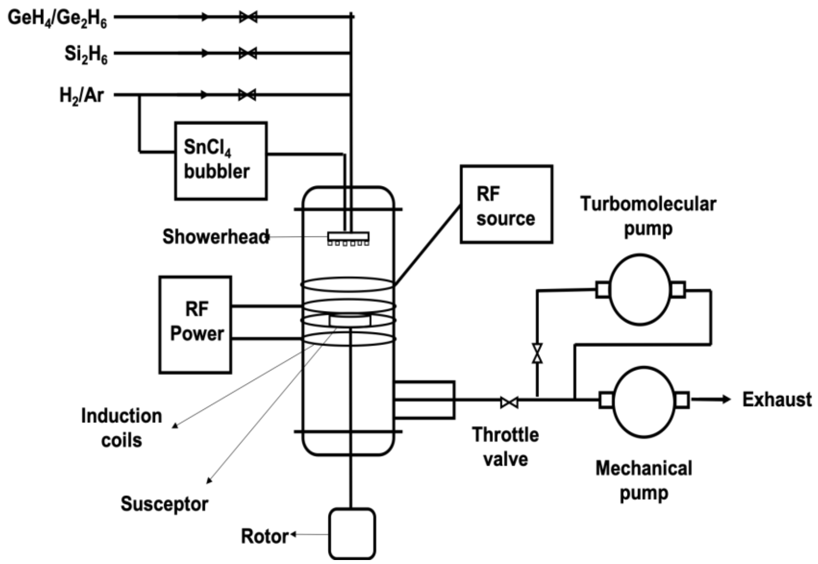

FIG. 2.3.1. Schematic of modified Reactor No.2 assembly

partial pressure of oxygen and water vapor in the reaction chamber. By the addition of the turbomolecular pump to the vacuum system, the background pressure in the growth chamber could be reduced to $<5*10^{-5}$ Torr. This helps to prevent the oxidation of the Si substrate which is crucial to attain epitaxial film deposition.

The need for ultra-high vacuum conditions during film growth was circumvented by employing an rigorous ex-situ chemical cleaning procedure comprising of HF solution and H_2SO_4-H_2O_2 solution baths to etch away the native oxide and get a hydrogen-terminated surface. The H-terminated surface prevented the re-oxidation of the Si surface during exposure to oxygen and water vapor while transferring the substrates to the susceptor, pumping down the chamber and heating the substrate. Thus the films could be deposited at a higher chamber background pressure ($>10^{-6}$ Torr) and background oxygen.

The details of the ex-situ chemical cleaning process employed to achieve epitaxial films are as follows. Phosphorus doped n-type Si (100) wafers (resistivity 4-16 Ω-cm) were used as the substrates. A chemical cleaning procedure as described by Carroll et al (2000) was adopted to remove the native oxide. This cleaning process allows to efficiently etch away the native oxide from the Si surface without the need for an in-situ pre-deposition H_2 bake. Initially, the substrates were cleaned by acetone, isopropyl alcohol and DI water to remove any organic residue on the surface. Then, the substrates were placed in a 1:100 HF (50% In DI water) aqueous solution for ~ 5 min to remove the native oxide. The surface was then chemically oxidized and the metal contaminants on the surface removed by placing the substrates in a H_2SO_4:H_2O_2 (35%) 1:1 bath at 70^{o}C for ~20 min. The substrates were then immersed back in the HF bath for ~20 min to remove the oxide formed and leave the surface hydrogen terminated. Finally, the substrates were washed with DI water, blow dried with nitrogen and immediately transferred to the growth chamber.

For film deposition, once the substrates had been placed inside the growth chamber and the flanges secured, the reaction chamber was then pumped down using a turbomolecular pump for ~20 minutes. The chamber pressure was measured using a wide range pressure gauge. Once adequate vacuum had been established in the reactor ($<5\times10^{-5}$ Torr), the turbo pump was cut-off using valves and the reactor was then pumped using the mechanical pump for the duration of the growth process. The film growth was then carried out by following the same procedure as for Reactor No. 2. The schematic of the modified reactor is shown in Fig 2.3.1.

Chapter 3 Growth of SiGeSn films using Reactor No. 1

3.1 Effect of temperature on SiGeSn film properties

Buffer-free polycrystalline SiGeSn thin films were deposited on Si using Reactor No. 1 at susceptor temperatures in the range of 350-450ºC and chamber pressure of 1 Torr. The films were deposited using commercially available GeH_4 (5% in Ar), Si_2H_6 (10% in H_2) and $SnCl_4$ (99.999%). Structural and optical properties of the deposited films were studied by Rutherford back scattering (RBS), X-ray diffraction (XRD), and Raman spectroscopy.

3.1.1 Experimental section

Phosphorus doped n-type Si (100) wafers (resistivity 10^{-3} Ω-cm and thickness 280 μm) were used as the substrates. The wafers were cut into 1inch by 1inch pieces for growth purposes. The substrates were placed in a buffered HF bath for ~ 5min, washed with DI water, blow dried with nitrogen and immediately transferred to the growth chamber. The germane, disilane, $SnCl_4$ flow rates were maintained at 100 sccm, 100 sccm and 20 sccm (with the partial pressures being 10 mTorr, 20 mTorr and 1.3 mTorr) respectively for the film growth. Films were deposited for a duration of 30 minutes.

The crystalline quality of the films were analyzed from XRD spectra obtained from PANalytical XPert Pro MRD diffractometer with Cu Kα radiation. The elemental profile of the deposited thin films was measured by using RBS measurements. The RBS measurements were carried out using a 1.7 MV Cockroft-Walton, gas-insulated high-frequency Tandem accelerator with a beamline and analysis chamber. 2MeV He^{2+} ions were used as the ion source and data collected at 10^5 rotating random counts with 8^o offset between ion beam and sample surface. SEM images of the cross section of the films were obtained using a Hitachi S-4700-II scanning electron microscope. Raman spectroscopy studies were performed at room temperature using a 532 nm 50 mW green laser coupled to a WiTec Alpha300R Confocal Raman Imaging system and a Princeton Instruments Acton SP2300 imaging spectrograph to analyze the nature of bonding and strain present in the films.

3.1.2 Results and Discussions

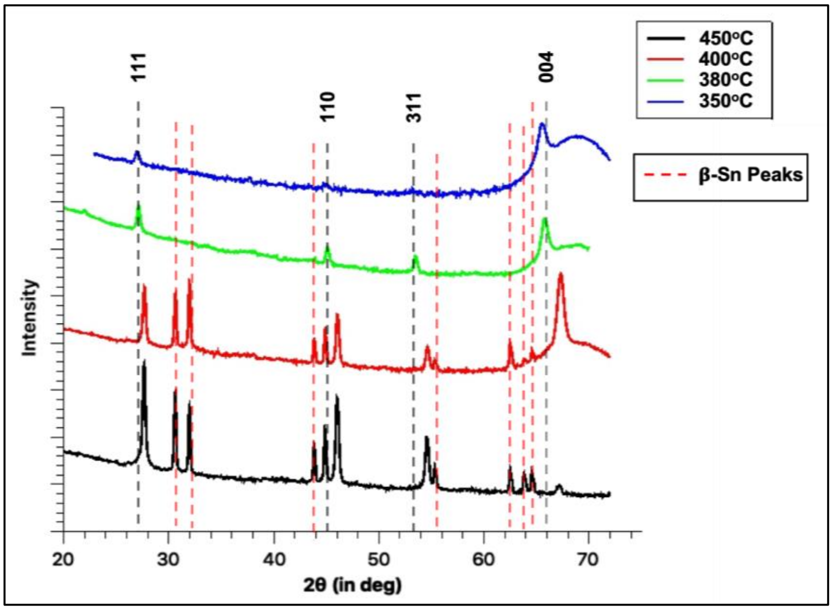

FIG. 3.1.1. XRD spectra of SiGeSn films showing Sn segregation in films grown at temperatures ≥400°C and no segregation in films grown at lower temperatures

Fig. 3.1.1 shows the XRD spectra of the deposited SiGeSn films. The spectra have been obtained between the angles of 20-75^o to locate peaks belonging to the Ge cubic lattice system. A 2^o ω offset was used during the scans. This was done to prevent the strong signal from the single crystalline Si substrate from saturating the detector. As a result, the peak belonging to the Si (100) plane at 69.12^o is observed as a broad peak in the scans instead of as a sharp peak. Diffraction peaks corresponding to the (111), (110), (311) and (004) SiGeSn planes are observed for the all the films (as marked in the Fig. 3.1.1.) (Ohmura et al. 2015; Wirths et al. 2014). This indicates that the films are polycrystalline in nature. The peak intensity profile for the polycrystalline films is similar to that of powder Ge (except the (004) peak intensity is higher on account of the Si (100) substrate used for film growth) (Khazaka et al. 2018). This indicates that the film has a nearly randomly oriented structure. The reason for the polycrystallinity is the non-UHV atmosphere during the deposition of the thin films (Alharthi et al. 2018). The vacuum established by the mechanical pump is not adequate to lower the partial pressure of oxygen and water vapor inside the chamber which is essential for epitaxial film growth at low temperatures (Schwartz 1992). This leads to the formation of SiO_2 islands on top of the silicon surface which impede epitaxial growth resulting in polycrystalline films. Segregated Sn (i.e. β-Sn) peaks can be observed in the XRD spectrum of the film grown at 450^{o}C and 400^{o}C (Oehl et al. 2015). Thus attempting to deposit films at high process temperatures (≥ 400^{o}C) resulted in Sn-segregation. The cause for this behavior is the low surface energy of Sn compared to Ge and the low thermodynamic solubility of Sn in Ge (Fournier-Lupien et al. 2014; Dou, Benamara, et al. 2018). The thermal energy at higher temperatures is sufficient for Sn to diffuse across the depositing film and undergo Ostwald ripening leading to phase separation (Khazaka et al. 2018; Kasper et al. 2012). However, no peaks belonging to β-Sn can be observed in the spectra for the films grown at temperatures less than 400^{o}C confirming that no Sn segregation had taken place during film growth at the lower growth temperatures. It can be seen that the SiGeSn (004) peaks shift significantly to the right relative to the Ge (004) peak (located at 66^o) for the films grown at temperatures ≥ 400^{o}C while the films grown below 400^{o}C do not exhibit this behavior. This is because at higher temperatures, the Si precursor Si_2H_6 has a higher rate of cracking than the Ge precursor which results in a higher Si content in the film relative to Ge (this will be confirmed by RBS analysis as discussed in the following section) (Hartmann, Aubin, and Barnes 2016). The higher Si content causes a shift of the (004) peak towards the Si (004) peak (located at 69.12^o). The FWHM of the XRD peaks were obtained by fitting a modified Gaussian model and the values were then used to calculate the grain size using the Debye Scherrer formula (Yamaha et al. 2015).

$$t = \frac{k * \lambda}{\beta * \cos\theta} \qquad (3.1.1)$$

where t is the average grain size, k is a dimensionless constant, λ is the X-ray wavelength (1.5405 Å for Cu Kα_1 line), β is the FWHM corrected for instrument broadening (in radians) and θ is the Bragg angle. The value of k was taken as 0.9 for simplification. It was observed that the grain size was in the range of 20-25 nm for all the attempted films which did not exhibit Sn segregation. The small size of the domains imply that deposited films have a high density of grains pointing to a high nucleation rate. This is most likely brought about by the plasma assisted high cracking rate of the precursors. The grain size was found to increase with increase in the growth temperature which is due to a higher surface diffusion rate at higher temperature resulting in grains coalescing to form fewer and larger grains (Asafa 2013).

The top section SEM images of the films are shown in Fig. 3.1.2. The films which have undergone Sn segregation have large droplet-like structures on the surface. These are the Sn atoms which have phase separated out of the SiGeSn film and coalesced at the surface. Nano-sized grains can be seen on the surface of the films grown in Runs 3 and 4 which corroborate with the grain size obtained from the XRD analysis. The films without Sn segregation are rough on the nanoscale level.

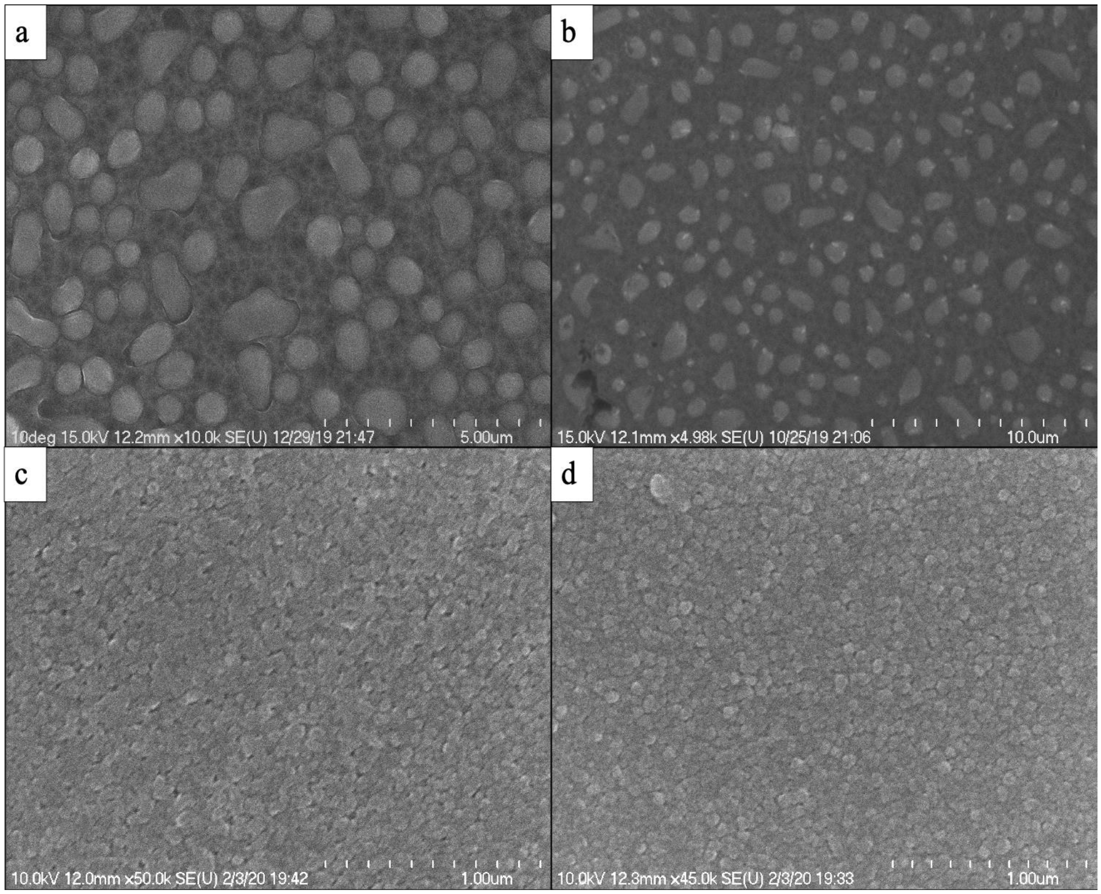

FIG. 3.1.2. Top section SEM image of (a) run 1, (b) run 2, (c) run 3 and (d) run 4. Sn segregation can be seen in fil grown in runs 1 and 2 while nano-sized grains can be seen in films grown in runs 3 and 4.

Fig. 3.1.3 shows the RBS spectra of the grown SiGeSn films. The position of the edges in the spectrum correspond to the different elements and their height is related to their atomic concentration (Wirths et al. 2014). The composition of the films is thus extracted, and the results obtained are given in Table 3.1.1. The thicknesses of the film layers were estimated by dividing the observed surface atomic density with the weighted volumetric atomic density as derived from the extracted compositions.

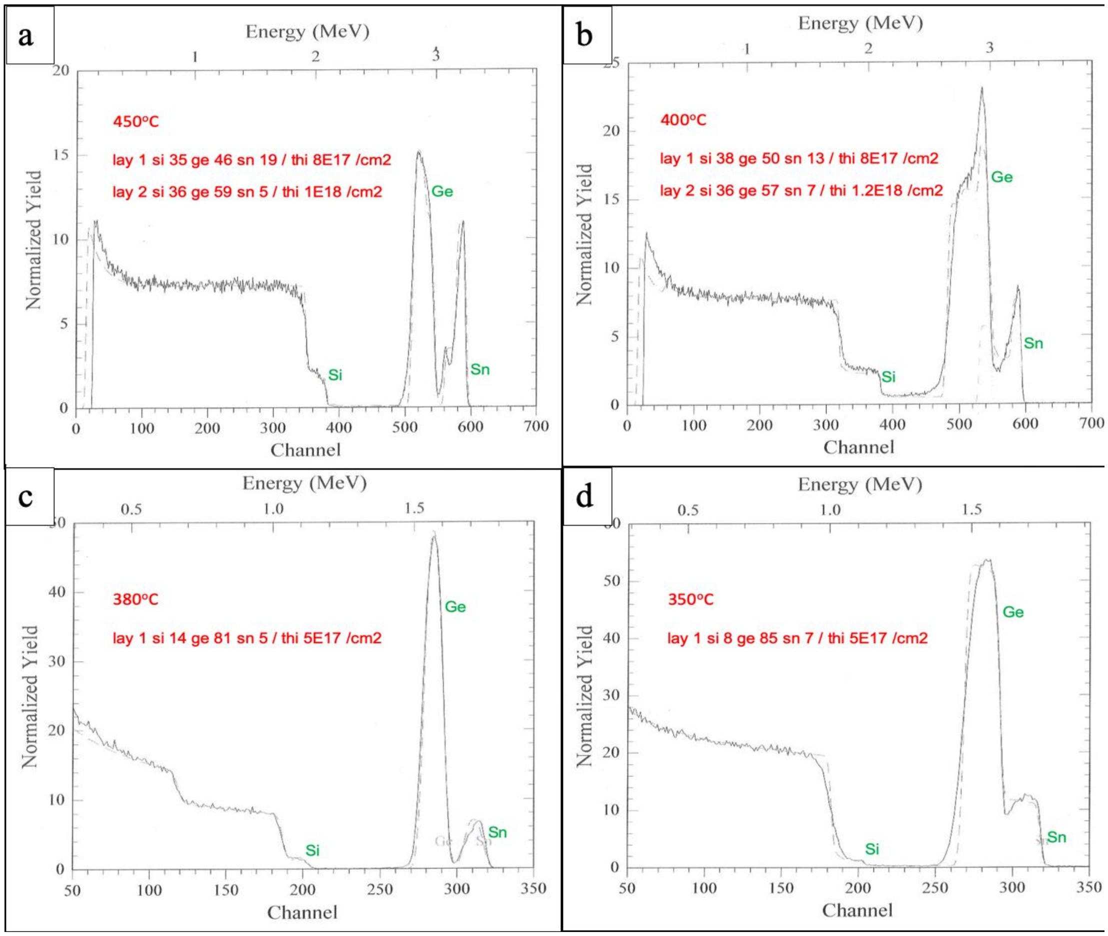

FIG. 3.1.3. RBS spectra of SiGeSn film grown at (a) 450ºC, (b) 400ºC (c) 380ºC and (d) 350ºC showing Sn segregation at growth temperatures ≥400ºC and no segregation at lower temperatures

Table 3.1.1. The concentration of Ge, Si and Sn in the different layers and the thickness of the layers of the deposited SiGeSn films as obtained from RBS analysis

Run no.	Growth temperature (^{o}C)	Layer	Ge %	Si %	Sn %	Thickness (nm)
1	450	Top	46	35	19	191
		Bottom	59	36	5	225
2	400	Top	50	38	13	187
		Bottom	57	36	7	600
3	380	-	81	14	5	114
4	350	-	85	8.5	6.5	56

It can be seen that for the films deposited at temperatures ≥ 400^{o}C, the spectra need to be modeled using two layers. This is indicative of Sn phase separating out of the film as β-Sn. This confirms the XRD results that higher growth temperatures leads to Sn phase separating out. The films grown below 400^{o}C do not exhibit this behavior confirming no β-Sn phase separation. Films grown at temperatures ≥ 400^{o}C have much higher Si content compared to films grown at lower temperatures which corroborates the XRD peak shift behavior. A higher Sn content was achieved in the film grown at 350^{o}C as opposed to the film grown at 380^{o}C. The increase in Sn concentration on lowering the growth temperature has been reported previously and is attributed to two factors - the lower thermal energy available for Sn to diffuse across the film and the reduction in germane reactivity (and subsequently the Ge deposition rate) (Von Den Driesch et al. 2015; Margetis et al. 2017; von den Driesch et al. 2017). Another observation made is that the film grown at 380°C is thicker compared to the film grown at 350°C. This is attributed to higher precursor cracking at higher substrate temperature, thus resulting in higher deposition rate (Asafa 2013).

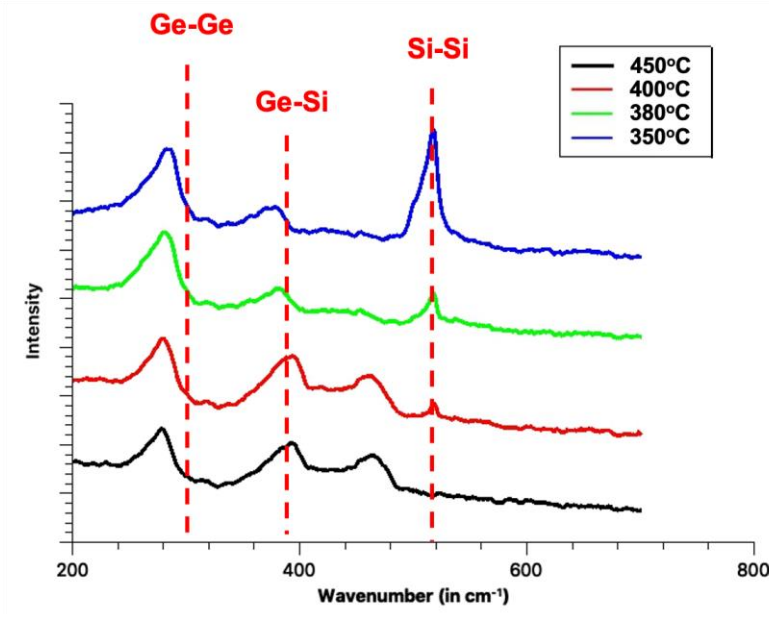

FIG. 3.1.4. Raman spectra of SiGeSn films deposited at different temperatures showing the Ge-Ge and Si-Ge phonon modes shifting to account for composition and strain

The Raman spectra of the deposited films are shown in in Fig. 3.1.4. Peaks corresponding to the Ge-Ge bond (~300 cm^{-1}) and Si-Ge bond (~390 cm^{-1}) are seen in the spectrum (Peng et al. 2019; Yamaha et al. 2015). Another peak located at ~475 cm^{-1} can be seen for the films deposited at 400°C and 450°C. This corresponds to the Si-Sn and is observed in the Raman spectra for these films due to the Sn segregation. The Ge-Ge peaks shift towards lower wavenumbers than their expected positions for all the films. The Raman peak shift ($\Delta\omega$) can be attributed to two factors – the substitution of Sn and Si in the Ge lattice ($\Delta\omega_{alloy}$) and the combination of strain and disorder present in the lattice ($\Delta\omega_{strain+disorder}$) (D’Costa et al. 2007; Zhang et al. 2017).

The source of the strain in the films is the due to two factors – the thermal stress from the difference in coefficient of thermal expansion between the film and substrate and the difference in the lattice constants of the SiGeSn films and the Si substrate. The disorder is due to the various lattice imperfections present in the polycrystalline film such as grain boundaries and lattice defects (Zhang et al. 2017). Δω and $\Delta\omega_{alloy}$ can be given as:

$$\Delta\omega = \omega_{Ge-Ge} - \omega_0^{Ge} \qquad (3.1.2)$$

$$\Delta\omega_{alloy} = y * a_{Ge-Ge}^{GeSi} + x * a_{Ge-Ge}^{GeSn} \qquad (3.1.3)$$

where ω_{Ge-Ge} is the observed Raman peak shift for the Ge-Ge bond, ω_0^{Ge} corresponds to the peak shift for the Ge-Ge bond in bulk Ge i.e $\omega_0^{Ge} = 301\ cm^{-1}$, y and x are the concentrations of Si and Sn in the films respectively, a and b are linear coefficients associated with film composition with $a_{Ge-Ge}^{GeSi} = 19.2\ cm^{-1}$, $a_{Ge-Ge}^{GeSn} = 93.5\ cm^{-1}$ .As the values of y and x are available from RBS measurements, $\Delta\omega_{strain+disorder}$ can be calculated for the films (Fournier-Lupien et al. 2013). The position of the Ge-Ge Raman peak (i.e. ω_{Ge-Ge}), the calculated Δω and the calculated $\Delta\omega_{strain+disorder}$ is given in Table 3.1.2.

It can be seen from Table 3.1.2 that the values of $\Delta\omega_{strain+disorder}$ for runs 1 and 2 are much lower than for runs 3 and 4. This is most likely because of the Sn segregation from the film releasing most of the strain present in the film lattice.

Table 3.1.2. Ge-Ge Raman peak positions for the SiGeSn films and the calculated values of $\Delta\omega$ and $\Delta\omega_{strain+disorder}$

Run No.	ω_{Ge-Ge} (cm^{-1})	$\Delta\omega$ (cm^{-1})	$\Delta\omega_{strain+disorder}$ (cm^{-1})
1	278.79	-22.21	2.275
2	280.32	-20.68	-1.229
3	283.06	-17.94	-10.577
4	284.55	-16.45	-8.561

3.2 Effect of substrate on SiGeSn film properties

3.2.1 Motivation for insulating substrates

Semiconductor on insulator technology has also drawn significant interest as a potential platform for integrated optical devices in the IR spectrum. This is because the technology allows for the coalition of the semiconductor properties and on-insulator advantages and can thus potentially lead to devices such as high mobility transistors and high frequency circuits (Li et al. 2011; Soref 2010). Silicon dioxide (SiO_2) is a widely used insulator in the semiconductor industry as its' use can lead to reduced parasitic capacitance, reduced latch up and a lower loss tangent (Gamble et al. 2008; Johnson et al.

1998). Thus, SiO_2 has potential use in the fabrication of group IV photonic devices such as waveguides and resonators. However, as SiO_2 strongly absorb above 2.5 µm, it's utilization as a substrate is restricted to the NIR region. Sapphire has been the substrate of choice for mid IR applications. This is because sapphire offers all the benefits provided by SiO_2, and it is transparent to wavelengths up to 6 µm and has low index which eliminates any potential substrate leakage (Huang et al. 2011; Wong et al. 2012). Thus, SiGeSn on sapphire can enable mid IR devices with lower power consumption and higher operating speeds (H. J. Kim et al. 2015; Blagov et al. 2014).

SiGeSn thin films of varying compositions were deposited on insulating substrates i.e. c-plane sapphire and 100 nm SiO_2 coated silicon (100) wafers as well as on highly conductive phosphorus doped Si (100) wafers. In our experiments, GeH_4 (5% in Ar), Si_2H_6 (10% in H_2) and $SnCl_4$ (99.999%) were used as the precursors for Ge, Si and Sn respectively. The composition of the films was varied by varying the precursor flow rates. Structural and optical properties of the deposited films have been studied by energy dispersive x-ray spectroscopy (EDX), Rutherford back scattering (RBS), X-ray diffraction (XRD), and Raman spectroscopy.

3.2.2 Experimental section

Films were grown on c-plane sapphire, 100 nm SiO_2 coated silicon (100) wafers and phosphorus doped Si (100) wafers (resistivity 10^{-3} Ω-cm). The Si substrates were placed in a buffered HF bath for ~ 5min, washed with DI water, blow dried with nitrogen and immediately transferred to the growth chamber. The insulating substrates were placed besides the Si substrate on the susceptor without undergoing any pre-deposition cleaning. GeH_4 and Si_2H_6 flow rates were set at 200 sccm and 50 sccm respectively for all runs (except for run 4 from Table I for which GeH_4 flow was reduced to 50 sccm). Films were deposited for 40 minutes at a substrate temperature of 380°C and chamber pressure of 1 Torr.

RBS was used in measuring the elemental profile and thickness of the deposited thin films. The RBS measurements were carried out using He^{2+} ions with 10^5 rotating random counts. The crystal structure, lattice constant and crystalline quality of the films were determined by XRD spectra, using PANalytical XPert Pro MRD diffractometer with Cu Kα radiation. Raman spectroscopy was performed at room temperature using a 532 nm 50 mW green laser coupled to a WiTec Alpha300R Confocal Raman Imaging system and a Princeton Instruments Acton SP2300 imaging spectrograph to analyze the nature of bonding and strain present in the films.

3.2.3 Results and Discussions

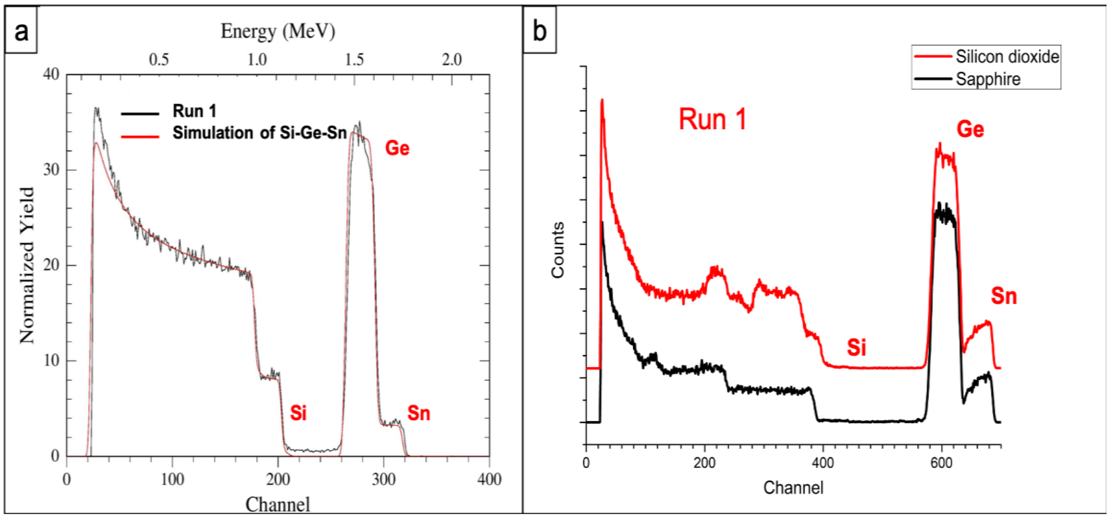

FIG. 3.2.1. (a) RBS spectrum of a representative film deposited on sapphire substrate along with the RUMP simulation (b) RBS spectra of Run 1 deposited on sapphire and silicon dioxide substrates

Fig. 3.2.1 a shows the RBS spectrum of a representative film deposited on sapphire substrate. The black line indicates the data obtained from RBS while the red line indicates the simulation fitted for the data using RUMP software. The position of the edges in the spectrum correspond to the different elements and their height is related to their atomic concentration. The signal from the different elements present in the film i.e. Si, Ge and Sn, take the form of plateaus which indicate the elements are uniformly distributed throughout the films. The thicknesses of the films were estimated by dividing the observed surface atomic density with the weighted volumetric atomic density as derived from the extracted compositions. The composition and the thickness obtained from RBS studies for grown films at different growth conditions are given in Table 3.2.1.

Table 3.2.1. The composition of the films extracted from RBS along with the various growth conditions under which the films are grown

Run no.	Sn bubbler flow rate (sccm)	Sn bubbler temperature (°C)	H_2 flow rate (sccm)	Substrate	Si content %	Ge content %	Sn content %	Film thickness (nm)
1	25	20	150	Sapphire	8.5	85.0	6.5	607.1
				SiO_2	8.4	84.9	6.7	582.8
2	15	20	150	Sapphire	25.6	71.9	2.5	233.7
				SiO_2	25.9	71.3	2.8	229.2
3	25	10	150	Sapphire	11.6	84.9	3.5	625.7
				Si	12.0	84.0	4.0	615.7
4	20	15	150	Sapphire	53.0	45.0	2.0	283.5
				Si	53.9	44.3	1.8	279.1

The analysis of the RBS spectra of the grown films indicated that Sn and Si concentrations up to 7% and 50% respectively were realized. Also, on comparing films grown on different growth substrates, it can be seen that use of different substrates did not affect the composition or thickness of the deposited films. Further, increasing the SnCl4 bubbler flow rate (Runs 1 and 3) or bubbler temperature (Runs 1 and 2) increases the Sn concentration due to the higher flux of Sn precursor reaching the substrate. Also, it can be seen that as the Sn content in the film increases, the Si content decreases correspondingly. This is most likely because Si and Sn compete for positions in the Ge lattice matrix and higher substitutional Sn leads to lesser positions for Si to incorporate in the lattice and thus lower concentration. Thus, the compositions of the films can be finely tuned by optimum variation of the operating parameters and primarily depends on the relative flows of the precursors in the gas and not on the substrate.

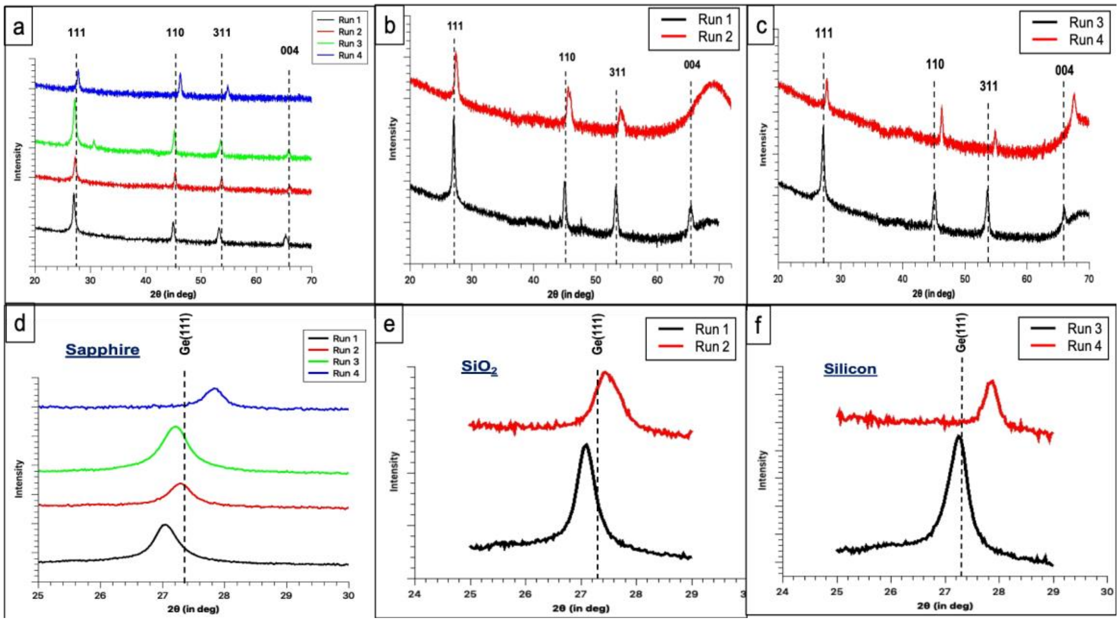

FIG. 3.2.2. XRD spectra of SiGeSn thin films with different compositions deposited on (a) sapphire (b) silicon dioxide and (c) silicon substrates. The shift of the (111) peaks of the films deposited on (d) sapphire (e) silicon dioxide and (f) silicon substrates relative to Ge indicates the varying composition of the films

Fig. 3.2.2 (a) is the XRD spectra of thin films with varying composition deposited on sapphire substrate, Fig. 3.2.2 (b) provides the XRD spectra of films grown on silicon dioxide, and Fig. 3.2.2 (c) presents the spectra of films grown on silicon substrate. Peaks correlating with the (111), (220), (311) and (004) SiGeSn peaks are observed with varying intensity in all the XRD spectra irrespective of the composition, thickness and the substrate. This implies that the deposited films are polycrystalline in nature and have a diamond cubic lattice structure (Park, King, and Choi 2008; H. J. Kim et al. 2015). The polycrystallinity on c-plane sapphire and Si (100) substrates is due to the non-UHV atmosphere employed to deposit the thin films. The vacuum established by the mechanical pump is insufficient to lower the partial pressure of oxygen and water vapor inside the chamber which is essential for epitaxial film deposition at low temperatures. This leads to the formation of SiO_2 islands on top of the substrate surface which hinder epitaxial growth. Since SiO_2 is polycrystalline in nature, the films deposited on the SiO_2 layer are also deposited in a polycrystalline manner. It can be noted that the positions of the peaks shift with respect to the Ge peaks (as can be seen in Fig 3.2.2 (d) (e) (f)). This is due to the fact the Si has a lower lattice constant while Sn has a larger lattice constant with respect to Ge causing a change in the lattice constant of the ternary alloy according to its composition(Aboozar Mosleh, Alher, Cousar, et al. 2016; Du et al. 2016).

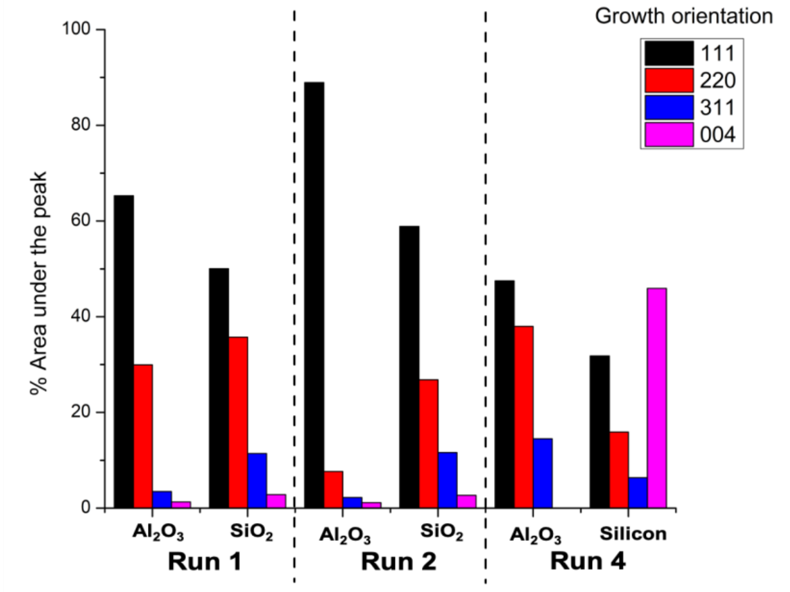

FIG. 3.2.3. The orientation preference for the grain domains depicted by percent area under the peaks for films deposited on different substrates and with varying compositions

For the films grown on sapphire, the (111) peak dominates the spectra in all films. This implies that most of the film has been deposited in the (111) orientation. This phenomenon has been previously reported for cubic structured films grown on c-plane sapphire substrates and is attributed to the low surface energy provided by the (0001) plane of sapphire to the formation of (111) crystal planes (Park, King, and Choi 2008; H. J. Kim et al. 2015). The (111) is also the strongest peak for the films deposited on silicon dioxide but it is not as dominant as for films deposited on (001) sapphire. This signals that the degree of randomness in crystal grain orientation for these films is higher than those deposited on sapphire. The grains being majorly (111) oriented has been previously recorded for cubic Ge and SiGe films grown on silicon dioxide (Sedky et al. 1998; Tsai and Reif 1995). The presence of trigonal SiO_2 grains present randomly in the silicon dioxide lattice is the most likely reason for the formation of (111) oriented grains, as is the case in trigonal c-plane sapphire (H. J. Kim et al. 2015; Park, King, and Choi 2008; Lager, Jorgensen, and Rotella 1982). The higher degree of randomness in the grain orientation is mostly due to the large number of nucleation sites offered by the amorphous SiO_2 layer. The films deposited on silicon substrate grow majorly in both the (111) and the (004) direction. The (004) orientation of the grains can be attributed to the (001) silicon substrate and the inclination of the film to grow epitaxially in (001) direction so as to minimize interface energy (Roucka et al. 2015; Zheng et al. 2015; Wirths et al. 2014). The cause of the (111) orientation is most likely due to the SiO_2 islands formed on the Si surface.

To better visualize the preference of the crystal orientation of the grain domains for the different substrates, the areas under the curves for the (111), (220), (311) and (004) XRD peaks were calculated, then added up and then the ratio of the area under each peak to the total area was obtained. In this way, the percentage of the domain growth to an orientation was obtained. This is shown in Fig. 3.2.3.

The full width at half maximum (FWHM) of the (111) XRD peaks for the different films was obtained by fitting a modified Gaussian model and the values were then used to calculate the size of the grains using the Debye Scherrer formula.

$$t = \frac{k*\lambda}{\beta*\cos\theta} \text{............................} (3.2.1)$$

where t is the average grain size, k is a dimensionless constant, λ is the X-ray wavelength (1.5405 Å for Cu Kα line), β is the FWHM (in radians) and θ is the Bragg angle. The value of k was taken as 0.9 for simplification. It was observed that the grain sizes were in the region of 20-35 nm for the films. The small size of the domains imply that deposited films have a high density of grains. This is most likely brought about by the plasma assisted high cracking rate of the precursors. The grain size of the films grown on sapphire is larger than the films grown on silicon dioxide. This is because of the large number of nucleation sites offered by the amorphous silicon dioxide. The grain size of the films grown on silicon is larger than the films grown on sapphire. The reason for this behavior is not yet known.

The lattice constant of the SiGeSn films was calculated using the position of (111) peak using Bragg's law with the assumption that the lattice is cubic in structure. The (111) peak was selected on account of its strong intensity in all the spectra. The relaxed lattice constant for a SiGeSn film with a particular composition was computed by using Vegard's law while taking into account the appropriate bowing parameter (Zheng et al. 2015; Moontragoon, Soref, and Ikonic 2012; Aboozar Mosleh 2015). The lattice constant was calculated using the following equation

$$a_{Si_yGe_{1-x-y}Sn_x} = y * a_{Si} + (1-x-y) * a_{Ge} + x * a_{Sn} + y * (1-x-y) * b_{SiGe} + x * (1-x-y) * b_{GeSn} + x * y * b_{SiSn} \text{................(3.2.2)}$$

where $a_{Si_yGe_{1-x-y}Sn_x}$ is the lattice constant of the relaxed ternary alloy, y, 1-x-y and x are the concentration of Si, Ge and Sn respectively in the ternary alloy, a_{Si}, a_{Ge} and a_{Sn} are the lattice constants of Si, Ge and Sn respectively with a_{Si} = 5.431Å, a_{Ge} = 5.658Å and a_{Sn} =6.489Å, $b_{SiGe} = -0.26$Å, $b_{GeSn} = -1.66$Å and $b_{SiSn} = 0$. The obtained values of the lattice constants, from Bragg's law and Vegard's law, are given in Table 3.2.2.

Table 3.2.2. The obtained values of the lattice constants, from Bragg's law and Vegard's law, along with the chemical compositions of the films

No.	Si (y)	Ge (1-x-y)	Sn (x)	Substrate	a_{Bragg} (Å)	a_{Vegard} (Å)	Δ a (Å)
1	0.08	0.85	0.07	Sapphire	5.70	5.59	0.11
				SiO_2	5.69	5.59	0.10
2	0.26	0.71	0.03	Sapphire	5.62	5.54	0.09
				SiO_2	5.62	5.54	0.08
3	0.12	0.84	0.04	Sapphire	5.67	5.59	0.09
				Silicon	5.66	5.59	0.08
4	0.53	0.45	0.02	Sapphire	5.55	5.48	0.07
				Silicon	5.54	5.48	0.06
-	0	1	0	N/A (bulk)	5.66	5.66	0

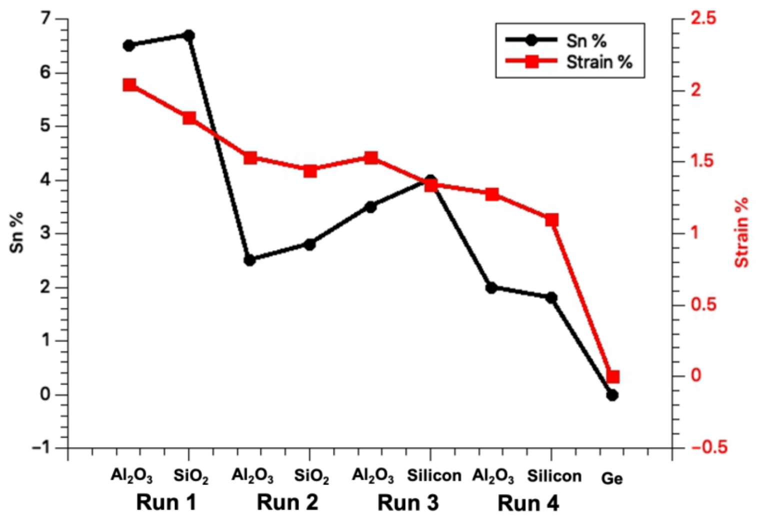

FIG. 3.2.4. The obtained strain from XRD for the films deposited on various substrates and with varying constitutions, with the tin content of the films also plotted simultaneously

The different in the lattice constant obtained from x-ray and calculated lattice constant based on composition are used for strain analysis. Understanding the strain present is in the films is of use as the bandgap of SiGeSn is also dependent on the strain. The obtained strain for the films deposited on various substrates and with varying composition are plotted and given in Fig. 3.24. The tin content of the films, obtained from RBS analysis, is also plotted simultaneously. The strain is tensile in all the films irrespective of the chemical composition or substrate. Further, the strain strongly depends on the concentration of Sn in all the films. A higher Sn content leads to a higher lattice strain while lower Sn content induces less strain. This is because of the larger atomic radius of Sn compared to Ge. Also, for films with same composition, the strain is higher for films grown for sapphire as compared to films grown on silicon dioxide or silicon. The relative lower strain when using silicon as a substrate is attributed to the smaller difference in the lattice constant of the ternary films and silicon compared to that with sapphire ($a_{Si} = 5.431Å\ vs\ a_{Sapphire} = 4.75Å$). The lesser strain in films grown on silicon dioxide is due to the higher density of grains in the films grown on silicon dioxide as compared to sapphire, leading to the larger relieving of strain through grain boundary formation.

The Raman spectra of the films with varying composition deposited on the different substrates (Runs 3 and 4 from Table I) are shown in Fig. 3.2.5. Peaks correlating to the Ge-Ge bond and Si-Ge bond are seen in all spectra while the peak correlating to the Ge-Sn bond can be delineated in some of the spectra.

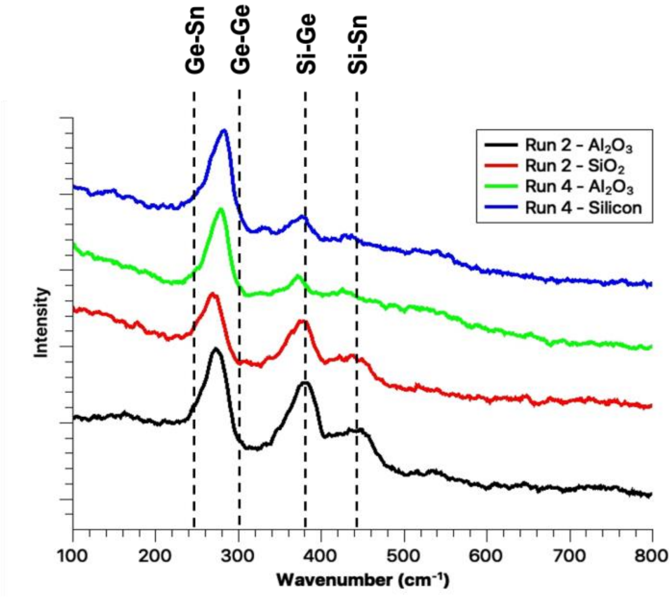

FIG. 3.2.5. Raman spectra of SiGeSn films deposited on different substrates, showing the Ge-Ge, Si-Ge and Ge-Sn bonds thus confirming the formation of the ternary alloy

The absence of the Ge-Sn in the remaining spectra is only due to the low concentration of Sn present in those films. However, the peaks in all the spectra shift towards lower wavenumbers than their expected positions implying the incorporation of Sn in the films. Thus, the presence of the bonds and their red shift confirms the formation of the ternary alloy in the deposited films. The amount of red shift of the Raman peaks of different films is due to the strain arising from the thermal stress from the difference in coefficient of thermal expansion between the film and substrate and the difference in the lattice constants between Si, Ge and Sn while the disorder is due to the various lattice imperfections present in the polycrystalline film such as grain boundaries and lattice defects.

3.3 Effect of composition grading on SiGeSn film properties

The step-graded growth approach has been employed to deposit high Sn content epitaxial GeSn films as it allows to gradually relax the built-in strain inside thick layers thereby limiting lattice imperfections and potentially inhibits Sn surface segregation.

However, to the best of our knowledge, it has not yet been evaluated for the growth of SiGeSn films. In this work, buffer-free polycrystalline SiGeSn thin films were deposited on Si using Plasma Enhanced Chemical Vapor Deposition (PECVD) with a step graded growth approach. Commercially available GeH_4 (5% in Ar), Si_2H_6 (10% in H_2) and $SnCl_4$ (99.999%) were selected as the precursors for Ge, Si and Sn respectively. Structural and optical properties of the deposited films were studied by Rutherford back scattering (RBS), X-ray diffraction (XRD), and Raman spectroscopy.

3.3.1 Experimental section

Phosphorus doped n-type Si (100) wafers (resistivity 10^{-3} Ω-cm) were used as the substrates. The wafers were cut into 1inch by 1inch pieces for growth purposes. The substrates were placed in a buffered HF bath for ~ 5min, washed with DI water, blow dried with nitrogen and immediately transferred to the growth chamber. Non-graded and graded SiGeSn films were grown at temperatures of 380^{o}C and 350^{o}C (±3^{o}C). Non graded films were deposited in a single step for low Sn (20 sccm) and high Sn precursor (60 sccm) flow rates. Composition graded SiGeSn films were deposited in 3 steps - by starting with a high Si precursor flow rate and low Sn precursor flow rate and then over

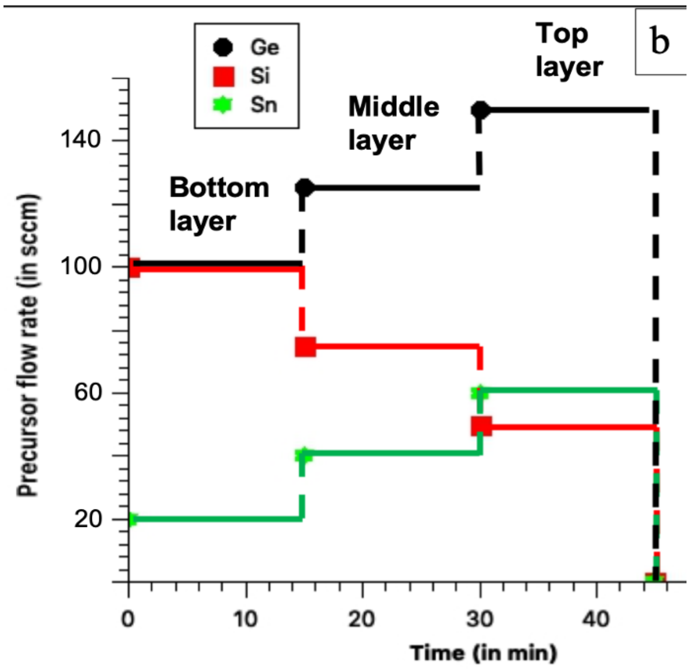

FIG. 3.3.1. Precursor flow rate profile vs time for the deposition of the graded SiGeSn film

time the Si precursor flow rate was dropped while the flow rates of the Ge and Sn precursors were ramped up (Si_2H_6 – 100, 75, 50 sccm; GeH_4 – 100, 125, 150 sccm and $SnCl_4$ – 20, 40, 60 sccm). The precursor flow rates were changed instantaneously for the different steps without stopping the precursor flows using an in-house developed software. The precursor flow rate profile vs time for the graded growth is given in Fig. 1b while the flow rates (and partial pressures) of the precursors used for film growth (both non-graded and graded) are given in Table 3.3.1. Chamber pressure was maintained at 1 Torr during growth.

Table 3.3.1. Growth conditions of Ge, Si and Sn precursors during deposition of the different layers

Run no.	Growth temperature (°C)	Layer	Si_2H_6 flow rate in sccm (partial pressure in mTorr)	GeH_4 flow rate in sccm (partial pressure mTorr)	$SnCl_4$ flow rate in sccm (partial pressure mTorr)	Flow time (min)
1	380	-	100(20.4)	100(10.2)	20(1.3)	15
2	380	-	50(9.4)	150(14.1)	60(3.5)	15
3	380	Top	50(9.4)	150(14.1)	60(3.5)	15
		Middle	75(14.7)	125(12.2)	40(2.4)	15
		Bottom	100(20.4)	100(10.2)	20(1.3)	15
4	350	-	50(9.4)	150(14.1)	60(3.5)	15
5	350	Top	50(9.4)	150(14.1)	60(3.5)	15
		Middle	75(14.7)	125(12.2)	40(2.4)	15
		Bottom	100(20.4)	100(10.2)	20(1.3)	15

The crystalline quality of the films was analyzed from XRD spectra obtained from PANalytical XPert Pro MRD diffractometer with Cu Kα radiation. The elemental profile of the deposited thin films was measured by using RBS measurements. The RBS measurements were carried out using a 1.7 MV Cockroft-Walton, gas-insulated high-frequency Tandem accelerator with a beamline and analysis chamber. 2MeV He^{2+} ions were used as the ion source and data collected at 10^5 rotating random counts with 8^o offset between ion beam and sample surface. Raman spectroscopy studies were performed at room temperature using a 532 nm 50 mW green laser coupled to a WiTec Alpha300R Confocal Raman Imaging system and a Princeton Instruments Acton SP2300 imaging spectrograph to analyze the nature of bonding and strain present in the films.

3.3.2 Results and Discussions

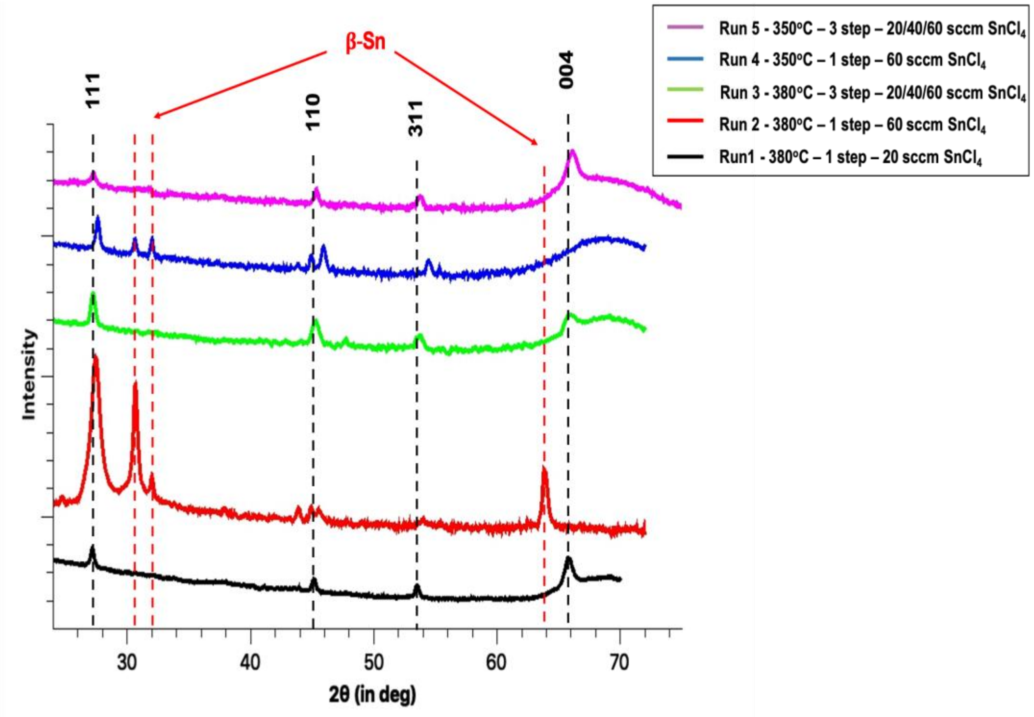

FIG. 3.3.2. XRD spectra of SiGeSn films showing Sn segregation in films grown with high $SnCl_4$ flow in 1 step and no segregation in films grown with step graded approach

Fig. 3.3.2 shows the XRD spectra of the deposited SiGeSn films. The spectra have been obtained between the angles of 20-75^o to locate peaks belonging to the Ge cubic lattice system. A 2^o ω offset was used during the scans. This was done to prevent the strong signal from the single crystalline Si substrate from saturating the detector. As a result, the peak belonging to the Si (100) plane at 69.12^o is observed as a broad peak in the scans instead of as a sharp peak. Diffraction peaks corresponding to the (111), (110), (311) and (004) SiGeSn planes are observed for the all the films (as marked in the Fig. 3.3.2) (Ohmura et al. 2015). This indicates that the films are polycrystalline in nature. The peak intensity profile for the polycrystalline films is similar to that of powder Ge. This indicates that the film has a randomly oriented structure. The reason for the polycrystallinity is the non-UHV atmosphere employed to deposit the thin films. The vacuum established by the mechanical pump is insufficient to lower the partial pressure of oxygen and water vapor inside the chamber which is essential for epitaxial film deposition at low temperatures. This leads to the formation of SiO_2 islands on top of the silicon surface which hinder epitaxial growth (Schwartz 1992). Segregated Sn also known as β-Sn can be confirmed from the corresponding X-ray peaks at 30.6^o, 32^o and 62.9^o . β-Sn peaks can be observed in the XRD spectrum of the films grown in a single step with high Sn flow (i.e. runs 2 and 4). Thus attempting to deposit films with higher Sn content by flowing higher Sn precursor flow resulted in Sn-segregation. However, no peaks belonging to β-Sn can be observed in the spectra for the graded films (i.e. run 3 and 5) confirming that no Sn segregation had taken place during film growth (A. Mosleh et al. 2015; Yamaha et al. 2015). Thus, depositing the films in a step graded manner allowed for higher Sn precursor flow without any Sn segregation. The explanation for this phenomenon will be provided in the next paragraph along with RBS analysis.

Theoretically, the XRD peaks for the composition graded films should have split in three sub-peaks due to the difference in composition between the layers. The XRD spectra were performed at the highest possible resolution (0.0125°) and a slow scan speed (0.005°/sec) on the XRD tool while focusing on the SiGeSn peaks but did not resolve the peaks any further. The plausible cause for this is that the layers are very thin (as calculated from RBS analysis) which makes it difficult to resolve the layers through XRD. The FWHM of the XRD peaks were obtained by fitting a modified Gaussian model and the values were then used to calculate the grain size using the Debye Scherrer formula.

$$t = \frac{k * \lambda}{\beta * \cos\theta} \qquad (3.3.1)$$

where t is the average grain size, k is a dimensionless constant, λ is the X-ray wavelength (1.5405 Å for Cu Kα_1 line), β is the FWHM corrected for instrument broadening (in radians) and θ is the Bragg angle. The value of k was taken as 0.9 for simplification. It was observed that the grain size was in the range of 20-30 nm for all the attempted films which did not exhibit Sn segregation. The small size of the domains imply that deposited films have a high density of grains pointing to a high nucleation rate. This is most likely brought about by the plasma assisted high cracking rate of the precursors. Also, addition of $SnCl_4$ as a precursor has been shown to increase the growth rate (i.e. precursor decomposition rate) at the substrate surface due to the exothermic reaction taking place on the decomposition of $SnCl_4$ (Margetis et al. 2017; M. Kim et al. 2015; Grant et al. 2017). The samples grown at 380°C (i.e. Runs 1 and 3) had a grain size of ~25±2 nm while the samples grown at 350°C (i.e. Run 5) had a grain size of ~20±1 nm. The samples grown at the higher temperature had a larger grain size as the additional thermal energy allowed for the smaller grains to migrate and merge into larger grains.

The top section SEM images of the films are shown in Fig. 3.3.3. The films which have undergone Sn segregation have large droplet-like structures on the surface (SEM image of run 4 not shown in figure as it is similar to run 2). These are the Sn atoms which have phase separated out of the SiGeSn film and coalesced at the surface. Nano-sized grains can be seen on the surface of the films grown in Runs 1, 3 and 5 which corroborate with the grain size obtained from the XRD analysis. The films without Sn segregation are rough on the nanoscale level.

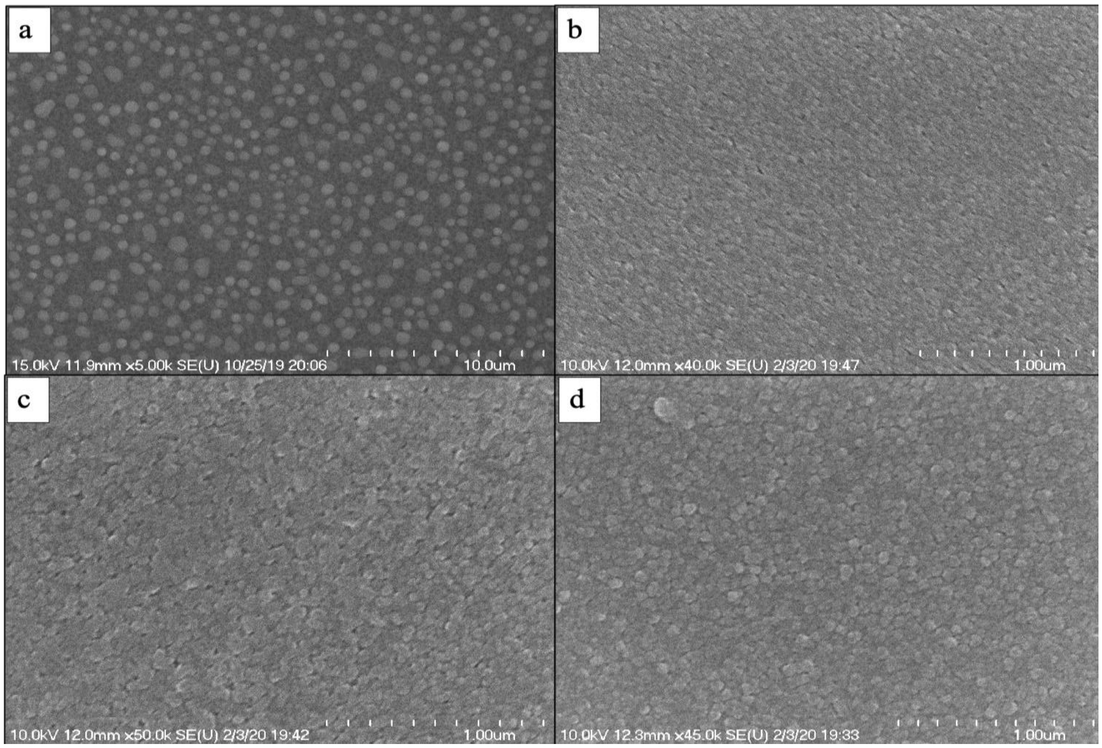

FIG. 3.3.3. Top section SEM image of (a) run 2, (b) run 1, (c) run 3 and (d) run 5. Sn segregation can be seen in fil grown in run 2 while nano-sized grains can be seen in films grown in runs 1, 3, 5.

Fig. 3.3.4 shows the RBS spectra of the grown SiGeSn films (RBS spectra of run 4 not shown in figure as it is similar to run 2).

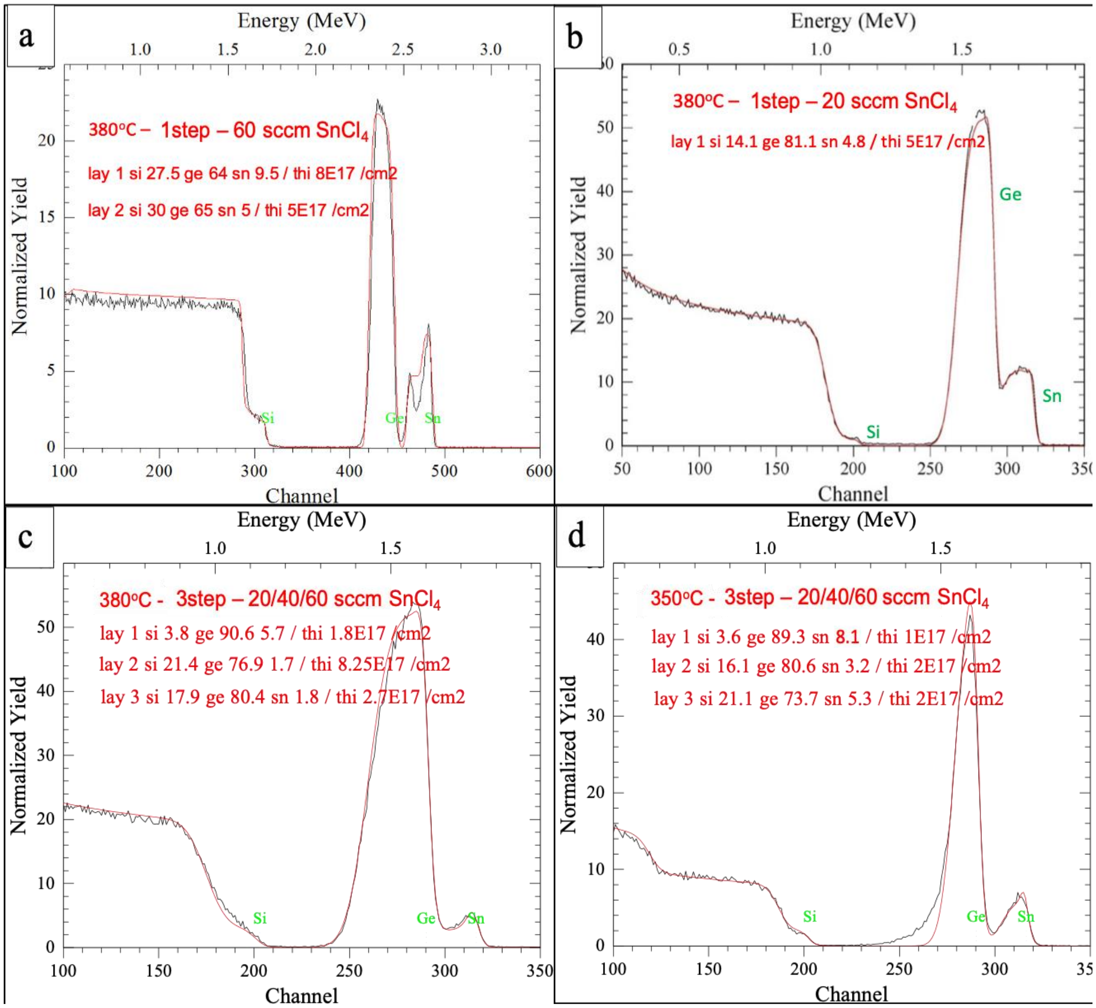

FIG. 3.3.4. RBS spectra (black) and RUMP fit (red) of (a) non-graded SiGeSn film grown at 380°C with high Sn precursor flow rate (run 2), (b) non-graded SiGeSn film grown at 380°C with low Sn precursor flow rate (run 1) (c) graded SiGeSn films grown at 380°C (run 3) and (d) graded SiGeSn films grown at 350°C (run 5)

The black line indicates the data obtained from RBS while the red line indicates the simulation fitted for the data using RUMP software. The position of the edges in the spectrum correspond to the different elements and their height is related to their atomic concentration. The composition of the films is thus extracted, and the results obtained are given in Table 3.3.2. The thicknesses of the film layers were estimated by dividing the observed surface atomic density with the weighted volumetric atomic density as derived from the extracted compositions.

Table 3.3.2. The concentration of Ge, Si and Sn in the different layers and the thickness of the layers of the deposited SiGeSn films as obtained from RBS analysis

Run no.	Growth temperature (ºC)	Layer	Ge %	Si %	Sn %	Thickness (nm)
1	380	-	81	14	5	115
2	380	Top	64	27	10	40
		Bottom	65	30	5	60
3	380	Top	90	4	6	40
		Middle	77	21	2	180
		Bottom	75	23	2	60
4	350	Top	14	63	23	35
		Bottom	58	33	9	65
5	350	Top	88	4	8	25
		Middle	81	16	3	45
		Bottom	74	21	5	45

From Fig. 3.3.4 a, it can be seen that for the non-graded film deposited with high Sn flow, the Sn peak splits into two (i.e. run 2 and 4). This is indicative of Sn phase segregating out of the film as β-Sn. This confirms the XRD results that higher Sn precursor flow leads to Sn phase separating out. For the graded films, no peak split is seen (runs 3 and 5). Also, the Si content decreases going from the substrate towards the top while the Ge and Sn concentrations show the opposite trend. Thus, the concentrations measured follow the trend of precursors flow profiles employed to deposit the graded film. The reason for the phase segregation of Sn from the films when attempting to deposit films with high Sn content in a single layer is the large strain in the film arising from the lattice mismatch between Sn (a = 6.46A^o) and Ge (a = 5.66A^o) and Si (a = 5.43A^o) (Dismukes, Ekstrom, and Paff 1964). Increase in the Sn content will lead to an increase in the lattice constant of the SiGeSn thin film (as per Vegard’s law) and thus generate higher lattice mismatch strain. For low Sn concentration in the film (run 1) the difference in lattice constant between the deposited film and the Si substrate is not large and the strain is mitigated through misfit dislocations at the film-substrate interface and the grain boundaries present in the polycrystalline films. However, with higher Sn content, the strain is too large to be relieved through the formation of lattice defects. Thus Sn phase separates out of the film when attempting to deposit films with higher Sn flows so as to diminish the strain the film (Margetis et al. 2017; M. Kim et al. 2015). Grading the layers is effective in obtaining films with no segregation as grading leads to a gradual increase in the lattice constant of the films and thus allows for strain to be relieved through the nucleation and glide of lattice defects in the bottom lower Sn-content layers allowing the upper layers to incorporate high Sn content (Aubin et al. 2017; Jo, Kim, and

Koh 2018). A higher Sn content was achieved in the top layer of the graded film grown at 350^{o}C as opposed to the graded film grown at 380^{o}C. The increase in Sn concentration on lowering the growth temperature has been reported previously and is attributed to two factors - the lower thermal energy available for Sn to diffuse across the film and undergo Ostwald ripening leading to phase separation and the reduction in germane reactivity (Margetis et al. 2017; Grant et al. 2019; Margetis et al. 2019). Thus, graded growth in conjunction with low process temperatures prevent segregation of Sn and thus can be used to grow films with high Sn content. The maximum Sn concentration achieved so far using the PECVD technique and graded growth approach is ~8%. Efforts are underway to try to increase the Sn content by increasing the Sn precursor flow and further decreasing the growth temperature. Additionally, a high Si concentration of 21% was demonstrated at low growth temperatures (<400^{o}C). This indicates that plasma assistance increased the cracking efficiency of the Si precursor. Another observation made is that the film grown at 380^{o}C is thicker compared to the film grown at 350^{o}C. This is attributed to higher precursor cracking at higher substrate temperature, thus resulting in higher deposition rate (Grant et al. 2017). It can also be seen that the thickness of the top layer of the graded films is much lower than that of the lower layers. This is due to the high $SnCl_4$ flow used during growth of the top layer. The $SnCl_4$ dissociation leads to the formation of HCl and Cl_2 as byproducts. These byproducts act as etchants during the film deposition and thus lower the film growth rate.

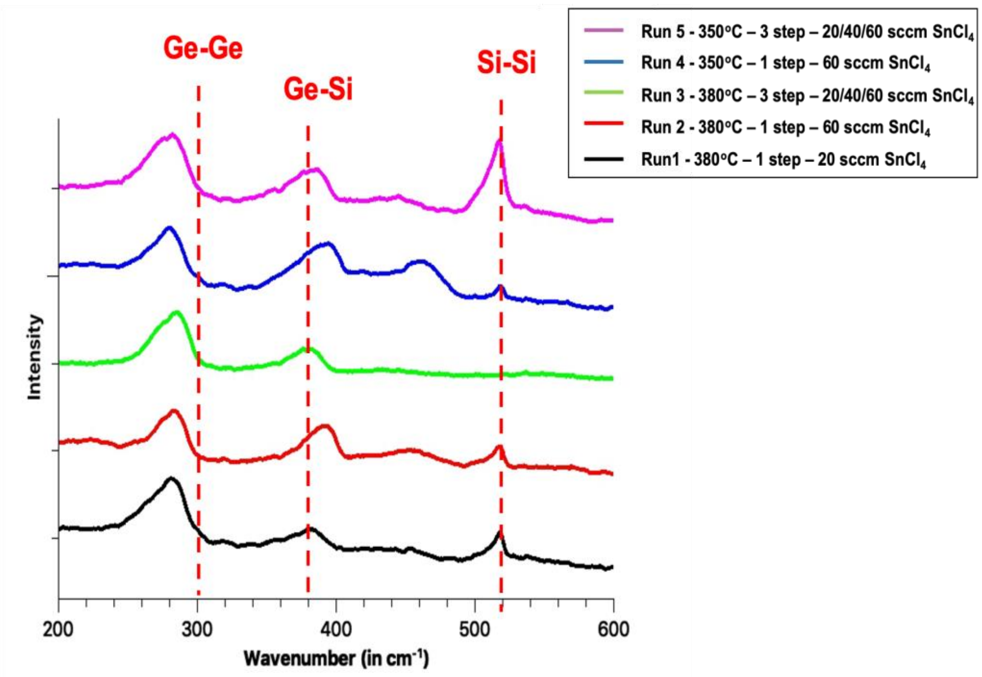

FIG. 3.3.5. Raman spectra of SiGeSn films showing the Ge-Ge and Si-Ge phonon modes shifting to account for composition and strain

The Raman spectra of the deposited films are shown in in Fig. 3.3.5. As the value of the extinction coefficient for SiGeSn films is not concretely established in literature, it is difficult to calculate the exact penetration depth of the laser beam in the deposited films. However, as the Si-Si Raman peak (521 cm^{-1}) from the substrate can be seen in all the Raman spectra (expect in Run 3 as it is thicker than the others) it is most likely that the Raman laser beam penetrates to a depth between 120-260 nm (thicknesses of run 1 and run 3 respectively) in the films and the Raman signal is coming from not just from the top layer but from all the layers. Peaks corresponding to the Ge-Ge bond (~300 cm^{-1}) and Si-Ge bond (~390 cm^{-1}) are seen in the spectrum. The absence of a distinctive Ge-Sn peak (~260 cm^{-1}) can be due to the low concentration of Sn present in the film. However, the Ge-Ge peaks shift towards lower wavenumbers than their expected positions. The Raman peak shift ($\Delta\omega$) can be attributed to two factors – the substitution of Sn and Si in the Ge lattice ($\Delta\omega_{alloy}$) and the combination of strain and disorder present in the lattice ($\Delta\omega_{strain+disorder}$). The source of the strain in the film is the thermal stress from the difference in coefficient of thermal expansion between the film and substrate and the difference in the lattice constants between Si, Ge and Sn while the disorder is due to the various lattice imperfections present in the polycrystalline film such as grain boundaries and lattice defects. $\Delta\omega$ and $\Delta\omega_{alloy}$ can be given as:

$$\Delta\omega = \omega_{Ge-Ge} - \omega_0^{Ge} \qquad (3.3.2)$$

$$\Delta\omega_{alloy} = y * a_{Ge-Ge}^{GeSi} + x * a_{Ge-Ge}^{GeSn} \qquad (3.3.3)$$

where ω_{Ge-Ge} is the observed Raman peak shift for the Ge-Ge bond, ω_0^{Ge} corresponds to the peak shift for the Ge-Ge bond in bulk Ge i.e $\omega_0^{Ge} = 301\ cm^{-1}$, y and x are the concentrations of Si and Sn in the films respectively, a and b are linear coefficients associated with film composition with $a_{Ge-Ge}^{GeSi} = 19.2\ cm^{-1}$, $a_{Ge-Ge}^{GeSn} = 93.5\ cm^{-1}$. As the values of y and x are available from RBS measurements, $\Delta\omega_{strain+disorder}$ can be calculated for the films. The position of the Ge-Ge Raman peak (i.e. ω_{Ge-Ge}), the full width half max (FWHM) of the peak and the calculated $\Delta\omega_{strain+disorder}$ is given in Table 3.3.3.

Table 3.3.3. Ge-Ge Raman peak positions for the SiGeSn films, the FWHM of the peaks and the calculated values of $\Delta\omega_{strain+disorder}$

Run no.	ω_{Ge-Ge} (cm^{-1})	FWHM (cm^{-1})	$\Delta\omega_{strain+disorder}$ (cm^{-1})
1	282.32	13.14	-11.32
2	284.75	8.54	-1.72
3	286.28	11.7	-8.34
4	280.32	7.58	-1.23
5	284.03	10.81	-8.72

It can be seen from Table 3.3.3 that the values of $\Delta\omega_{strain+disorder}$ for runs 1, 3 and 5 are similar. This is most likely because of the similar crystalline quality (as evidenced by the similar values of the FWHM of the Raman peaks) and the similar grain sizes (as seen from XRD analysis) of the films. However, the value of $\Delta\omega_{strain+disorder}$ is much lower for runs 2 and 4. This is most likely because of the Sn segregation from the film releasing most of the strain present in the film lattice.

3.4 Selective Area Growth (SAG) of SiGeSn thin films for photodiodes

SiGeSn thin films were deposited over patterned silicon substrates by selective area growth (SAG). SAG using patterned masks has been demonstrated to be an effective way to fabricate a wide range of optoelectronic devices. SAG is also effective in improving the material quality of the deposited films by lowering threading dislocation densities. The selectively grown films were fabricated into test photodiodes and tested for electrical performance.

3.4.1 Experimental section

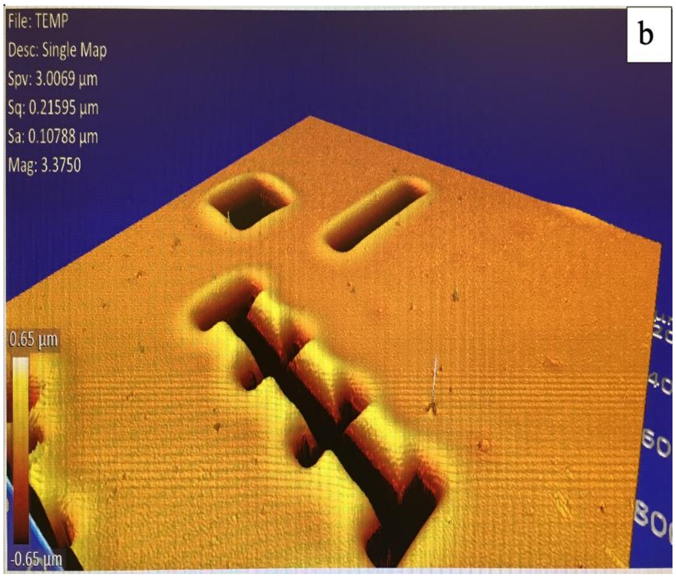

FIG. 3.4.1. Optical profile of the patterned Si substrate used for SAG and fabrication of photodiodes

100 nm SiO_2 layer was deposited on Si (100) substrates by sputtering. The wafer was then covered with photoresist and lithography was used to define the desired patterns - hall bars and rectangles. The long section of the hall bar was 675 μm in length and 75 μm wide, the rectangles at the ends of the hall bar were 175 μm in length and 50 μm wide and the smaller rectangles at the sides were 75 μm in length and 50 μm wide. The individual rectangles were 450 μm in length and 25 μm wide. Next the oxide was etched using a buffered oxide etchant (BOE) to etch away the oxide layer in the patterned areas and expose the silicon surface. The remaining photoresist was then removed by acetone. The optical profile of the fabricated patterned wafers (showing the hall bar and the rectangle shaped windows) is shown in Fig. 3.4.1. The patterned wafers underwent buffered oxide etchant cleaning (for <1 min to not etch away the deposited oxide layer) and were then introduced in the PECVD chamber to deposit the SiGeSn thin films selectively on the exposed silicon part. The films were deposited at a temperature of 350°C and chamber pressure of 1 Torr. The germane, disilane, SnCl4 flow rates were maintained at 100 sccm,

100 sccm and 20 sccm (with the partial pressures being 10 mTorr, 20 mTorr and 1.3 mTorr) respectively for the film growth. The films were grown up to a thickness of 100 nm. After deposition, the SiGeSn structures were then spin coated with image reversal photoresist and subjected to another round of lithography to deposit Cr/Au metal contacts on top of the SiGeSn films. BOE was again used to remove the oxide in the areas where metal contacts were to be deposited, and a 20/200 nm layer of Cr/Au was then grown via E- beam evaporation. The contacts were finalized using acetone lift-off and the devices were finally cleaned in an oxygen plasma.

Raman spectroscopy studies were performed at room temperature using a 532 nm 50 mW green laser coupled to a WiTec Alpha300R Confocal Raman Imaging system and a Princeton Instruments Acton SP2300 imaging spectrograph to confirm that the films were grown selectively on the patterned substrates before further fabricating them into photodiodes. Current-Voltage (I-V) measurements were performed on the photodiodes fabricated from the patterned hall bars. The metal contact deposited on the hall bar was used as the top electrode while the highly conductive Si substrate on which the films were grown was used as the bottom electrode. The I-V measurements were done using a high temperature probe station, in dark, and under illumination with a 1200 nm 5 mW LED source placed 1 cm away from the device.

3.4.2 Results and Discussions

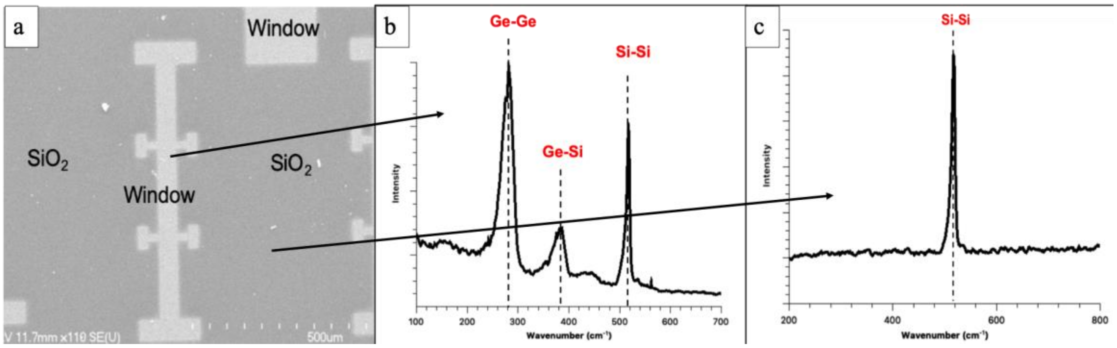

FIG. 3.4.2. (a) SEM image of patterned substrate post film growth (b) Raman spectra within window region showing bonds corresponding to SiGeSn film (c) Raman spectra on SiO_2 film outside window showing no film growth

The SEM image of SiGeSn film grown by SAG on patterned Si-substrate (before the deposition of metal contacts) and its Raman characterization is shown in Fig. 3.4.2. Raman spectra from the film deposited on the Si had peaks corresponding to Ge-Ge, Ge-Si and Si-Si bonds establishing SiGeSn growth in the window while the spectra from the region outside the window only showed Si-Si peak (corresponding to the Si substrate below the oxide layer) indicating no SiGeSn growth had taken place there[11]. This proves that the films were deposited selectively over the bare Si substrate and no deposition took place over the SiO_2 layer.

The results of the current-voltage (I-V) measurements carried out on the fabricated photodetectors are shown in Fig. 3.4.3. The fabricated devices exhibit clear rectifying behavior. Further, the photocurrent generation significantly increased under IR illumination, indicating photon absorption and carrier generation in the deposited SiGeSn film and thus proving that the films have a band edge below that of Si and can be utilized as IR photodetectors (Casalino et al. 2010; Fang et al. 2018).

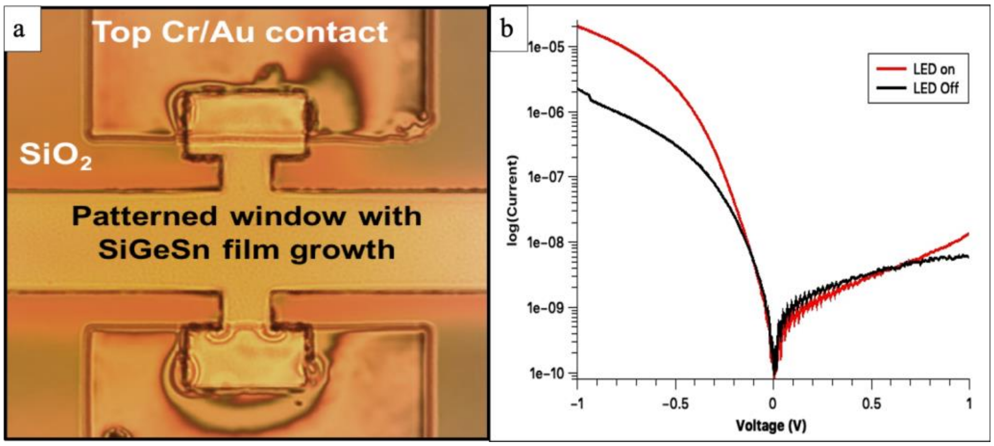

FIG. 3.4.3. (a) Optical microscope image of basic photodiode device after metal deposition using photolithography (b) IV measurements carried out on the fabricated photodetectors showing clear rectifying behavior and enhanced photocurrent generation under IR illumination

The observed value of photogenerated current (I_P) is 1.77×10^{-5} A at 1V bias and the ratio photogenerated current (I_P) to the dark current (I_D) at 1V bias is ~10. The low gain and the large reverse current can be attributed to the large number of grain boundaries and other defects present in the deposited polycrystalline film. The power density of the light arriving from the LED source is 0.022 W/sq.cm. while the surface area of the hall bar device is 8.31×10^{-4} sq.cm. Thus, the responsivity R of the fabricated photodiode at 1200 nm incident wavelength is $\frac{I_P}{P} = \frac{1.77*10^{-5}}{0.022*8.31*10^{-4}} = 0.962$ A/W.

Chapter 4 Growth of Ge and SiGeSn films using Recator No. 2

4.1 Effect of reactor parameters on Ge film uniformity

Ge films were deposited using GeH_4 (10% in Ar) as Ge precursor at various growth conditions to understand the effect of reactor parameters on film thickness uniformity. The thicknesses of the deposited films were measured using a Filmetrics F20 thickness measurement instrument.

4.1.1 Results and Discussions

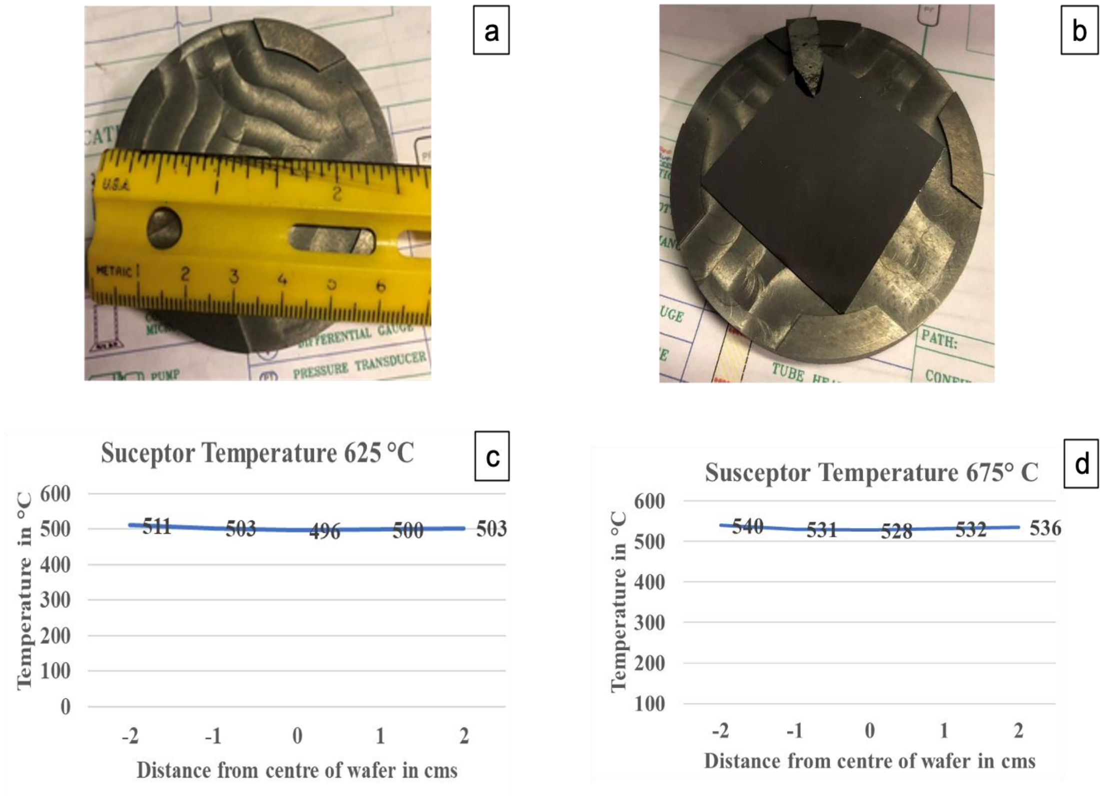

FIG. 4.1.1 (a) Photograph of susceptor (b) Photograph of susceptor with a sample placed (c) Plot of temperature at different spots of the wafer at susceptor temperature of 625°C (d) Plot of temperature at different spots of the wafer at susceptor temperature of 675°C

Temperature Uniformity: It is important to measure the temperature non-uniformity of the substrate since the CVD precursor reaction and crystallization process depends on the temperature of the process. For temperature uniformity measurements, a ~2-inch square cut wafer was placed in the middle of the susceptor, the susceptor was heated to 625°C and 670°C and the temperature of the substrate surface was measured at different spots using an external optical pyrometer. The temperature measured at each spot of the wafer is shown in figure 4.1.1 for susceptor temperatures of 625°C and 670°C. The average temperature of the substrate measured at 18 points are 504°C and 534°C with a standard deviation of 4.3°C and 4.6°C respectively. The temperature variation has standard deviation less than 0.9% indicating uniform temperature distribution over the susceptor. The average temperature of the wafer surface was ~ 130°C lower compared to susceptor and this difference is attributed to the loss of heat due to lesser contact area between wafer and susceptor and/or due to the error due to emissivity difference between substrate and the susceptor.

Thickness Uniformity: The uniformity of obtained Ge films was analyzed by depositing Ge films at 500°C susceptor temperature and chamber pressure of 1 Torr (without any susceptor rotation) by flowing germane at 50 sccm for 20 min at different ratios of uniform to hydride push and measuring the thickness profile of the films. The thickness profile of the grown Ge layers is shown in Fig 4.1.2. It was observed that films deposited using a high uniform to push ratio had a standard deviation of 31% and a M-shape profile indicating center and the edge having lower thickness while the in-between

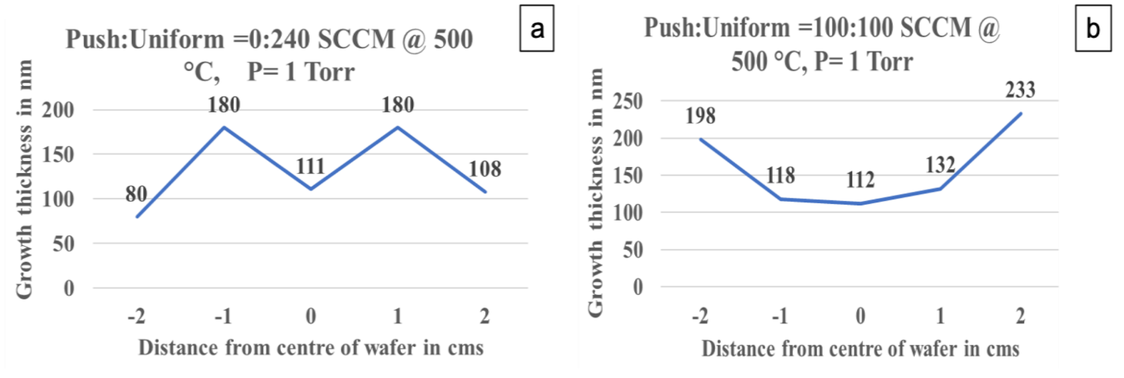

FIG. 4.1.2. Plot of thickness of Ge film grown at 625ºC susceptor temperature with (a) uniform flow of 200 sccm and no alkyl push and (b) with uniform flow of 100 sccm and hydride push of 100 sccm.

region having higher thickness. With a low uniform to push ratio, a standard deviation of 37% and a bowl shaped profile indicating the thickness increasing from center to outside. Thus a more uniform film profile can be achieved by optimizing the uniform to hydride flow rates.

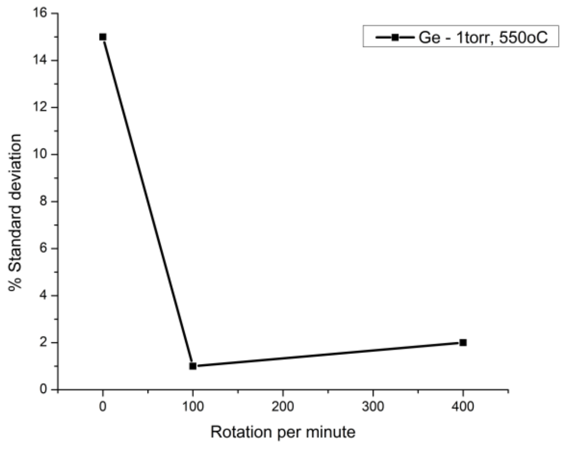

FIG. 4.1.3. Standard deviation around the mean thicknesses of Ge films with different susceptor rotation speeds showing improvement in deposition uniformity with rotation on

Rotation effect: It was seen that films grown without any susceptor rotation had a standard deviation of around 15% around the mean thickness value, films grown with susceptor rotation of 100 rpm had a standard deviation of around 1% while films grown with susceptor rotation of 400 rpm had a standard deviation of around 2%. Thus susceptor rotation helps to improve the uniformity of the deposited films. However, rotating at very high speeds also seems to lead to decrease in uniformity and thus further runs were carried out with susceptor rotation at low speeds.

4.2 Effect of growth conditions on Ge film growth

Ge films were deposited on Si (100) substrates by flowing germane at 12.5 mTorr partial pressure at growth temperatures of 300-600°C and chamber pressures of 1-5 Torr for a duration of 30 minutes with and without plasma enhancement. The thicknesses of the deposited films were measured using a Filmetrics F20 thickness measurement instrument. The crystalline quality of the films were analyzed from XRD spectra obtained using a PANalytical XPert Pro MRD diffractometer with Cu Kα radiation.

4.2.1 Results and Discussions

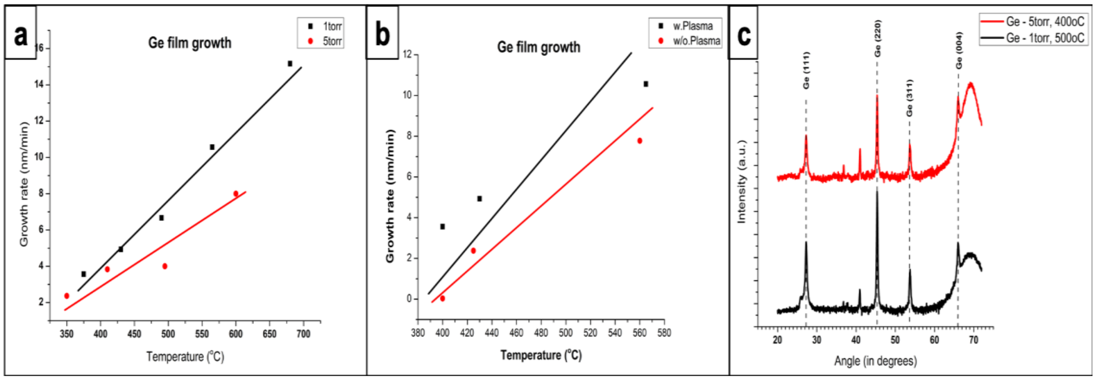

FIG. 4.2.1 (a) Ge film growth rate at different growth conditions (b) Ge film growth rate at different growth temperatures with and without plasma assistance (c) XRD spectra of Ge films grown at different conditions showing polycrystalline growth

It can be seen from Fig 4.2.1 a that the film growth rate increased linearly with temperature. This is due to the higher thermal energy available at higher temperatures leading to a larger dissociation of the precursor molecules. Also, the growth rate was higher for lower pressures compared to higher pressures. This is because the lower pressures enhanced the rate of hydrogen desorption from the surface after the reaction of the Ge hydride source which lead to increased growth rates. From Fig 4.2.1 b, it can be seen that the film growth occurred at lower growth temperatures with plasma assistance. This implies that the presence of plasma during growth increased the cracking of the Ge hydride source leading to lower growth temperature (Cariou et al. 2014; Littlejohns et al. 2015). This is important while depositing SiGeSn films efficiently temperatures which important since SiGeSn films are grown at lower growth temperatures (<500^{o}C). Even in the absence of plasma, the growth rate linearly increased with temperature.

Diffraction peaks corresponding to the (111), (110), (311) and (004) SiGeSn planes were observed in the XRD spectra for the all the films as seen in Fig 4.2.1 c. This indicates that the films are polycrystalline in nature. The reason for the polycrystallinity is the non-UHV atmosphere during the deposition of the thin films. The vacuum established by the mechanical pump is not adequate to lower the partial pressure of oxygen and water vapor inside the chamber which is essential for epitaxial film growth at low temperatures. This leads to the formation of SiO_2 islands on top of the silicon surface which impede epitaxial growth resulting in polycrystalline films.

4.3 Effect of rapid thermal annealing (RTA) on Ge film crystal quality

Ge films were deposited on Si (100) substrates by flowing germane at 50 sccm at growth temperatures of 300-600^{o}C and chamber pressures of 1-5 Torr for a duration of 30 minutes. The films were then annealed using RTA in nitrogen atmosphere for 120 s at 600^{o}C and for 20 s at 900^{o}C. The crystalline quality of the deposited films were analyzed from XRD spectra obtained using a PANalytical XPert Pro MRD diffractometer with Cu Kα radiation.

4.3.1 Results and Discussions

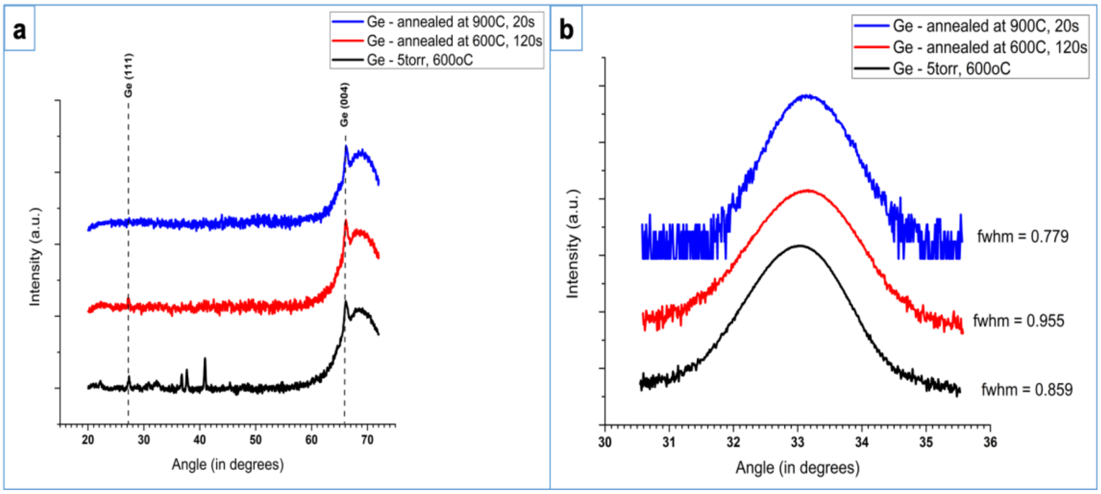

FIG 4.3.1 (a) XRD spectra and (b) Rocking curve of Ge films annealed under various conditions showing improvement in crystal quality upon annealing at high temperature

Fig. 4.3.1 shows the XRD spectra of the as-deposited and annealed SiGeSn films deposited under these conditions. It can be seen that only the peak belong to the (004) Ge plane is present in the XRD spectra of the film annealed at 900^{o}C. This is indicative that the film is epitaxial in nature. It can also be seen that that annealing the films at 600^{o}C caused an increase in the FWHM of the XRD rocking curve peaks while annealing at 900^{o}C caused a decrease in FWHM. This implies that annealing the films at lower temperature caused the film crystal quality to degrade while annealing at higher temperatures resulted in a significant improvement in the film quality. This might be because while annealing at 600^{o}C, the given annealing time might be too less for crystal planes to rearrange further than required. However, at 900^{o}C, the annealing temperature is close to the melting temperature of Ge (923^{o}C) and this causes the film to melt and recrystallize in an epitaxial manner over the Si substrate (Liu et al. 2013; Yeh et al. 2014). Thus, epitaxial Ge films with good crystal quality could be achieved with post-deposition high temperature annealing.

4.4 Effect of growth conditions on SiGeSn film deposition

GeH_4 (10% in Ar), Si_2H_6 (10% in H_2) and $SnCl_4$ (99.999%) were used as the Ge, Si and Sn precursors for the deposition of SiGeSn films. Attempts to deposit SiGeSn thin films on Si (100) substrates using Reactor No. 2 were carried out by varying the precursor flow rates, varying the growth temperature in the range of 350-500^{o}C, varying the chamber pressure in the range of 1-100 Torr and varying the $SnCl_4$ bubbler temperature in the range of 0-20^{o}C.

The crystalline quality of the deposited of films were analyzed from XRD spectra obtained from PANalytical XPert Pro MRD diffractometer with Cu Kα radiation. The elemental profile of the deposited thin films was measured by using RBS measurements carried out using a 1.7 MV Cockroft-Walton, gas-insulated high-frequency Tandem accelerator with a beamline and analysis chamber. 2MeV He^{2+} ions were used as the ion source.

4.4.1 Results and Discussions

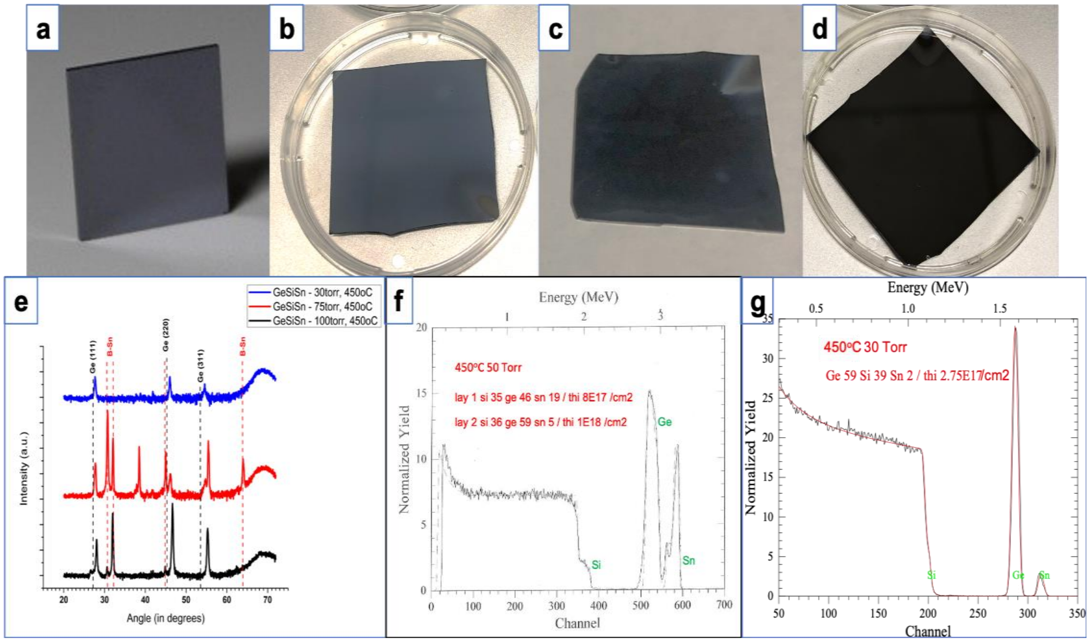

FIG. 4.4.1 (a) Picture of Si substrate with no film growth. Picture of SiGeSn film grown on Si substrate with (b) large Sn segregation (c) some Sn segregation (d) no Sn segregation. (e) XRD spectra of GeSiSn films deposited under various conditions showing polycrystalline films and Sn segregation in some films (f) RBS spectrum and RUMP simulation of GeSiSn film showing Sn segregation (g) RBS spectrum and RUMP simulation of GeSiSn film with no Sn segregation

Deposition of SiGeSn films was first attempted by using the conditions which had been successful with Reactor No. 1. The runs were done at a Sn bubbler temperature of 20°C and a chamber pressure of 1 torr. However, these attempts failed to produce any film deposition inspite of varying the growth temperature over a wide range (300-530°C) and by varying the Sn precursor flow rate in the range of 10-20 sccm while maintaining the Ge and Si precursor flow rate at 200 and 150 sccm respectively. This was confirmed by XRF and XRD characterization. This might be due to one of the following reasons. The new reactor tube had a larger cross section area compared to the old run. Also, while in the old reactor the precursors were introduced as a single stream, in the new reactor, the showerhead splits the streams into several small streams through the input nozzles thus distributing the flow. This decreased the net flux of the precursors reaching the substrate. Due to the low chamber pressures and low precursor fluxes, the residence time of the precursors over the substrate might be very less to initiate any nucleation and growth. Also, as the showerhead is made out of stainless steel, it might be inductively coupling with the heating induction coils. This might be leading to the precursors reacting in the gas phase as opposed to on the surface and depositing on the chamber walls instead of on the substrate. To counter this, for next growth runs, the flux of the precursors was increased by increasing the precursor push flows and the residence time was increased by increasing the chamber pressure from the previously used 1 Torr to >15 Torr. These changes resulted in the deposition of SiGeSn films. It was observed that film growth did not take place below recorded susceptor temperatures of 430^{o}C which might be because of the temperature being too low to crack the precursors at that temperatures. On the other hand, increasing the temperature above 490^{o}C or having growth pressures greater than 50 torr led to the deposition of a thick metallic layer on the surface. From XRD analysis, peaks associated with ß-Sn (i.e. metallic tin) were seen in the XRD spectra of films which have a silvery appearance. This implies that for films deposited under these conditions, the Sn does not completely integrate into the SiGeSn films but segregates into a separate layer. This is mostly likely because at higher temperatures, the higher thermal energy causes the Sn to diffuse and coalesce while at higher pressures, the high residence time for the Sn precursor also results in tin coalescing. Thus, the Sn coalesces and segregates into a separate layer rather than diffusing in the films at higher growth temperatures and pressures. The RBS spectra for these films need to be modeled using two layers which is also indicative of Sn phase separating out of the film as β-Sn. This situation was avoided for further runs by decreasing the Sn precursor partial pressure by lowering the $SnCl_4$ bubbler temperature (from 20^{o}C to 10^{o}C to 0^{o}C). Films deposited at 10^{o}C bubbler temperature had a hazy appearance as opposed to a silvery appearance. Also, the β-Sn peaks present in the XRD spectra of the films were not as intense as in the films have a silvery appearance. This implied that Sn segregation decreased on decreasing the bubbler temperature. Eventually, clear films with no Sn segregation were deposited by employing growth pressures of 15-30 torr, growth temperatures of around 450^{o}C and $SnCl_4$ bubbler temperature of 0^{o}C. These conditions seem to provide the adequate precursor fluxes and residence times to counter the etching effect of Cl_2 and HCl which are formed due to the dissociation of $SnCl_4$ and the hydrides and the interaction between the released chlorine and hydrogen entities. XRD data revealed that the SiGeSn films deposited were polycrystalline in nature. The reason for the polycrystallinity is the non-UHV atmosphere during the deposition of the thin films. No β-Sn peaks were present in the XRD spectra confirming Sn segregation was not present in these films. The SiGeSn XRD peaks shifted to the right relative to Ge XRD peak positions indicating a high concentration of Si was present in the films. The peaks shift to the right due to the Si (100) peak being located at 69.12^o as opposed to the Ge (004) peak being located at 66° (Sedky et al. 1998; Teh et al. 2001). From RBS analysis of the films, it can be seen that the films (where Sn segregation has not taken place) have been deposited as a single layer. The Sn content in the films is upto 2%. The thickness of the films deposited using 30 torr chamber pressure was 60 nm which computes to a growth rate of 2 nm/min. Summary of the different growth conditions employed for depositing SiGeSn films and their outcome is provided in the table 4.4.1 below.

Table 4.4.1. Summary of growth conditions utilized for depositing SiGeSn films

No.	Growth pressure (in torr)	Susceptor temperature (in °C)	Ge/Si precursor ratio	Ge/Sn precursor ratio	Film deposition/appearance/Sn segregation
1 (Reactor no. 1 conditions)	0.8-1	375-450	0.25-1	10-60	Clear film with no Sn segregation
2	0.5-1	300-535	0.33-1.1	2.7-50	No film growth
3	48-100	385-500	0.33	43-78	Silvery film with large Sn segregation
4	28-40	435-515	0.85-1.5	150-450	Hazy film with some Sn segregation
5	15 -30.7	445-460	0.33	43-150	Clear film with no Sn segregation

4.5 Use of Ge buffer films for SiGeSn film deposition

A Ge buffer film was first deposited on the Si (100) substrate by flowing GeH_4 (10% in Ar) at 50 sccm at 400°C substrate temperature and chamber pressure of 1 Torr by PECVD for a duration of 30 min. SiGeSn films were then deposited on top of the Ge buffer films by flowing GeH_4 (10% in Ar), Si_2H_6 (10% in H2) and SnCl4 (99.999%) at 150 sccm, 15 sccm and 10 sccm respectively at a substrate temperature of 315°C for a duration of 30 min.

The crystalline quality of the deposited of films were analyzed from XRD spectra obtained from PANalytical XPert Pro MRD diffractometer with Cu Kα radiation. The elemental profile of the deposited thin films was measured by using RBS measurements carried out using a 1.7 MV Cockroft-Walton, gas-insulated high-frequency Tandem accelerator with a beamline and analysis chamber. 2MeV He^{2+} ions were used as the ion source.

4.5.1 Results and Discussions

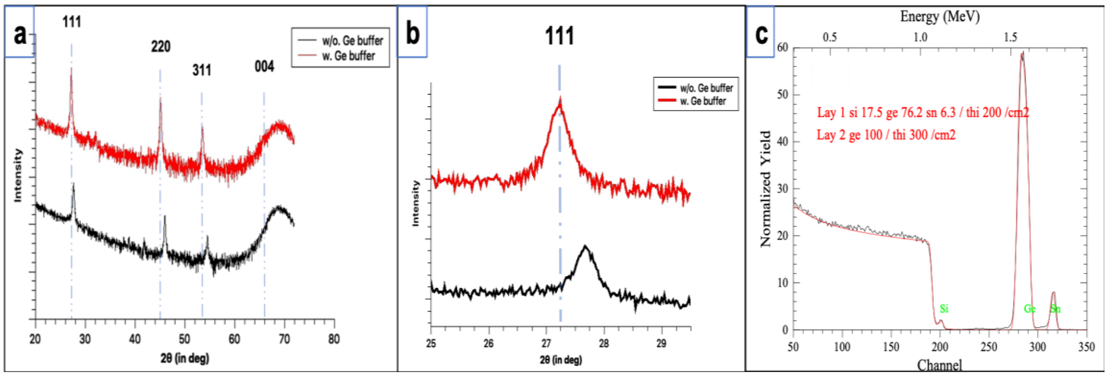

FIG. 4.5.1 (a) XRD spectra and (b) Zoomed in (111) XRD peak of SiGeSn films deposited with and without Ge buffer. (c) RBS spectrum and RUMP simulation of GeSiSn film deposited using Ge buffer

SiGeSn films obtained in initial attempts had to be deposited with a high Si% (30-40%) by using a high Si precursor flow rate during deposition in order to counter the issue of lattice mismatch between SiGeSn and Si so as to limit the strain the films and prevent Sn segregation. However, SiGeSn films with high Si % result in an indirect bandgap material and thus has limited applications for optoelectronic devices. To deposit SiGeSn films with lower Si concentration, a Ge buffer was introduced before the deposition of the SiGeSn films to help relieve the strain arising from the large lattice mismatch between the films and Si substrate (Alharthi et al. 2017). XRD data revealed that the SiGeSn films deposited were polycrystalline in nature due to the non-UHV atmosphere during the deposition of the thin films. XRD analysis of the films showed the SiGeSn peaks don't shift to the right relative to Ge XRD peak positions indicating a lower concentration of Si was present in the films. From RBS analysis, it was seen that the films with Sn concentration of 6% were achieved at a film growth rate of 2 nm/min by using a Ge:Si:Sn precursor ratio of 15:1.5:1. Thus, by employing a Ge buffer, the Si % could be decreased from 40% to 18% and the Sn% could be increased from 2% to 6% without leading to any Sn segregation in the achieved films.

As the composition of the films is available from RBS analysis, the lattice constants of the relaxed films can be calculated from Vegard's law as given in Equation 3.2.2 (from Chapter 3 subsection 3.2 Page 40). Substituting the composition values of $Si_{17.5}Ge_{76}Sn_{6.5}$ films which were achieved when depositing over a Ge buffer, the lattice constant of the alloy comes out 5.6 Å. For the $Si_{39}Ge_{59}Sn_{2}$ films which were achieved when depositing without a Ge buffer, the lattice constant of the alloy comes out 5.56 Å. As the lattice is cubic in nature, the interplanar distance for the (111) plane comes out to

3.23 Å and 3.21 Å for the $Si_{17.5}Ge_{76}Sn_{6.5}$ and $Si_{39}Ge_{59}Sn_2$ films respectively. Applying Bragg's law, the value of the XRD peak position for the (111) plane comes out as 27.5° and 27.8° for the $Si_{17.5}Ge_{76}Sn_{6.5}$ and $Si_{39}Ge_{59}Sn_2$ films respectively. Thus, there is a difference of ~ 0.3° in the peak position values. This value is in close agreement observed difference of ~0.35° in the XRD peak positions for the (111) plane of the films grown with and without Ge buffer (as seen in Fig 4.5.1 b). The small discrepancy in the observed and calculated value might be due to the films being strained to a different extent when being deposited over the Si substrate or the Ge buffer (due to differences in the lattice constants, coefficients of thermal expansion etc.)

4.6 SiGeSn film deposition using Ge_2H_6 as Ge precursor

A Ge buffer film was first deposited on the Si (100) substrate by flowing Ge_2H_6 (10% in Ar) at 20 sccm at 350°C substrate temperature and chamber pressure of 1 Torr by CVD without any plasma enhancement for a duration of 30 min. SiGeSn films were then deposited on top of the Ge buffer films by flowing Ge_2H_6 (10% in Ar), Si_2H_6 (10% in H_2) and SnCl4 (99.999%) at 100 sccm, 10 sccm and 10 sccm respectively at a substrate temperature of 300°C for a duration of 30 min.

The crystalline quality of the deposited of films were analyzed from XRD spectra obtained from PANalytical XPert Pro MRD diffractometer with Cu Kα radiation. The elemental profile of the deposited thin films was measured by using RBS measurements carried out using a 1.7 MV Cockroft-Walton, gas-insulated high-frequency Tandem accelerator with a beamline and analysis chamber. 2MeV He^{2+} ions were used as the ion source. IR spectroscopy was done at room temperature using a Perkin Lambda 950 UV/Vis/NIR spectrometer in the wavelength range of 1500-2200 nm to analyze the absorption properties of the films. The absorption spectrum of the films was obtained by collecting the reflectance (%R) and transmittance (%T) spectra of the film and then subtracting the sum of the values from 100.

4.6.1 Results and Discussions

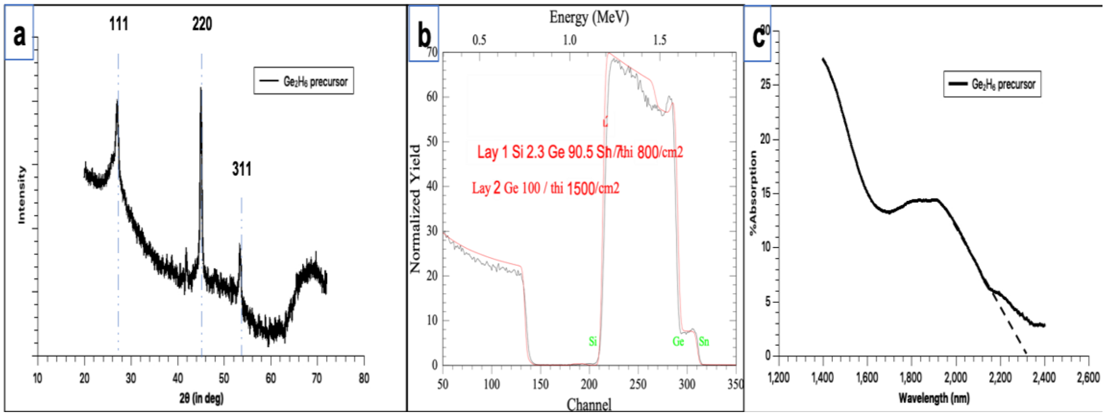

FIG. 4.6.1 (a) XRD spectra (b) RBS spectrum and RUMP simulation and (c) Absorption spectrum of SiGeSn films deposited using Ge_2H_6 as Ge precursor

In order to increase the growth rate at lower growth temperatures and increase the Sn %, SiGeSn were deposited with Ge_2H_6 as the Ge precursor. XRD data revealed that the SiGeSn films deposited were polycrystalline in nature due to the non-UHV atmosphere during the deposition of the thin films. From RBS analysis, it was seen that the films with Sn concentration of ~7% were achieved by using a Ge:Si:Sn precursor ratio of 10:1:1. The thickness of the films deposited was 180 nm which computes to a growth rate of 6 nm/min. Thus, higher Sn concentrations and higher growth rates could be achieved with Ge_2H_6 at a lower Ge precursor flow rate. This can be achieved because Ge_2H_6 has a lower dissociation energy than GeH_4 (Hartmann, Aubin, and Barnes 2016). Fig. 4.6.1 (c) shows the absorption spectrum of the SiGeSn film deposited using digermane. It can be seen that the film has a cut-off wavelength of ~2300 nm (which equates to an energy of 0.54 eV). Thus, the obtained films can be used for the fabrication of infrared detectors in the mid-IR region.

Chapter 5 Epitaxial growth of Ge and GeSn films using modified Reactor No. 2

5.1 Epitaxial Ge film growth using GeH_4 precursor

GeH_4 (10% in Ar) was used as the precursor to deposit Ge films. Ge films were deposited at substrate temperatures of 350°C-385°C. The films were deposited at chamber pressures in the range of 1 - 10 Torr while the precursor partial pressure was varied from 4 - 32 mTorr. Films were deposited with and without plasma assistance. The precursor was flown for a duration of 60 minutes to deposit the Ge films. The film growth conditions for different attempted runs is given in Table 5.1.1.

Table 5.1.1. Film growth conditions for different runs

Run no.	Substrate temperature (°C)	Chamber pressure (Torr)	GeH_4 flow rate (sccm) (Partial pressure in mTorr)	Plasma enhancement
1	385	1	20(4)	No
2	385	10	20(4)	No
3	385	10	80(16)	No
4	385	10	160(32)	No
5	350	1	20(4)	No
6	350	10	20(4)	No
7	350	10	80(16)	No

8	350	10	160(32)	No
9	350	1	20(4)	Yes
10	350	10	20(4)	Yes
11	350	10	80(16)	Yes
12	350	10	160(32)	Yes

The crystal structure and crystalline quality of the films were determined by XRD spectra and rocking curve measurements, using PANalytical XPert Pro MRD diffractometer with Cu Kα radiation. SEM images of the cross section of the films were obtained using a Hitachi S-4700-II scanning electron microscope to observe the thicknesses of the obtained films. The surface roughness of the films was measured using a Zygo Zescope optical profilometer. Raman spectroscopy was performed at room temperature by using a 532 nm 50 mW green laser coupled to a WiTec Alpha300R Confocal Raman Imaging system. A Princeton Instruments Acton SP2300 imaging spectrograph was used to analyze the nature of strain present in the films. IR spectroscopy was done at room temperature using a Perkin Lambda 950 UV/Vis/NIR spectrometer in the wavelength range of 1500-2200 nm to analyze the absorption properties of the films. The absorption spectrum of the films was obtained by collecting the reflectance (%R) and transmittance (%T) spectra of the film and subtracting the sum of the values from 100.

5.1.2 Results and Discussions

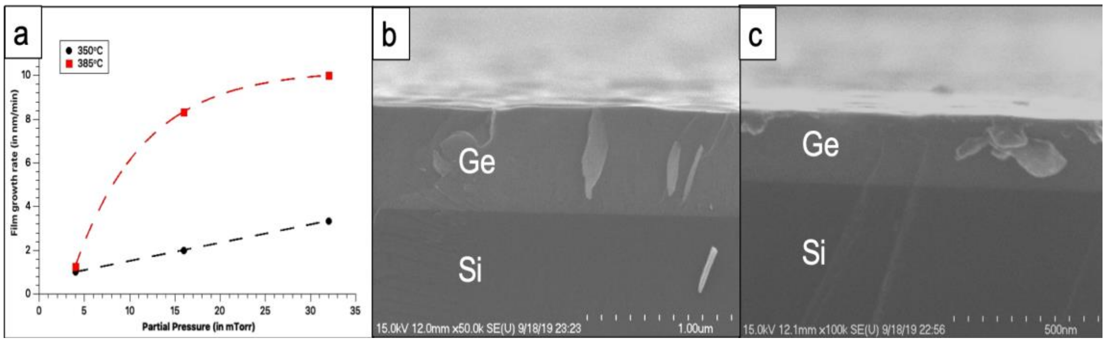

FIG. 5.1.1. (a) Growth rate of Ge films at different GeH_4 partial pressures at chamber pressure of 10 Torr and two different substrate temperatures – 350°C and 385°C (b) SEM image of the cross section of the Run 4 film (c) SEM image of the cross section of the Run 8 film

Attempts to deposit films at 1 Torr did not result in any film growth at 350°C and 385°C (runs 1 and 5). Increasing the chamber pressure to 10 Torr led to film deposition. This is because at the higher chamber pressure, the frequency of collisions between the precursor molecules increases leading to a fraction of the precursor flow undergoing dissociation in the gas phase itself which contribute to film formation (Greve 1998; Asafa 2013). X-ray diffraction spectra of the films (collected between 2θ of 20 and 75°) confirmed that all the films have been deposited in an epitaxial manner irrespective of the high chamber background pressure (>10^{-6} Torr). This is because of the optimization of the timings taken for turbo pumping of the chamber once the wafers have been transferred and the commencement of film deposition. The use of turbo pumping significantly decreases the concentration of oxygen and water vapor after the sample has been secured inside the chamber. The turbo pump is used to reduce the background pressure to ~5×10^{-5} Torr. Thus, the partial pressure of oxygen in the background after pumping is 8x10^{-6} Torr (20% of atmosphere). However, as per Greve (1998), the partial pressure of oxygen needs to be below 1.94x10^{-13} Torr at deposition temperature of 385^{o}C and below 4.69 x10^{-14} Torr at deposition temperature of 350^{o}C. The value of oxygen partial pressure during the process is therefore much higher than the required values. To overcome this, the silicon substrate surface is terminated with hydrogen by ex-situ cleaning to considerably decrease its' reactivity with oxygen. Also, hydrogen flow is maintained continuously after the turbo pumping is stopped and the substrate is only heated to a low temperature (<400^{o}C). Also, the film growth is initiated within 1 hour and a high Ge/O partial pressure ratio is used during film growth. These steps ensure that the desorption of hydrogen from the surface is inhibited till the first few monolayers of Ge have been deposited and consequently allow the Ge films to be deposited at high background chamber pressures (>10^{-6} Torr). The optimized process flow is shown in Fig. 5.1.2.

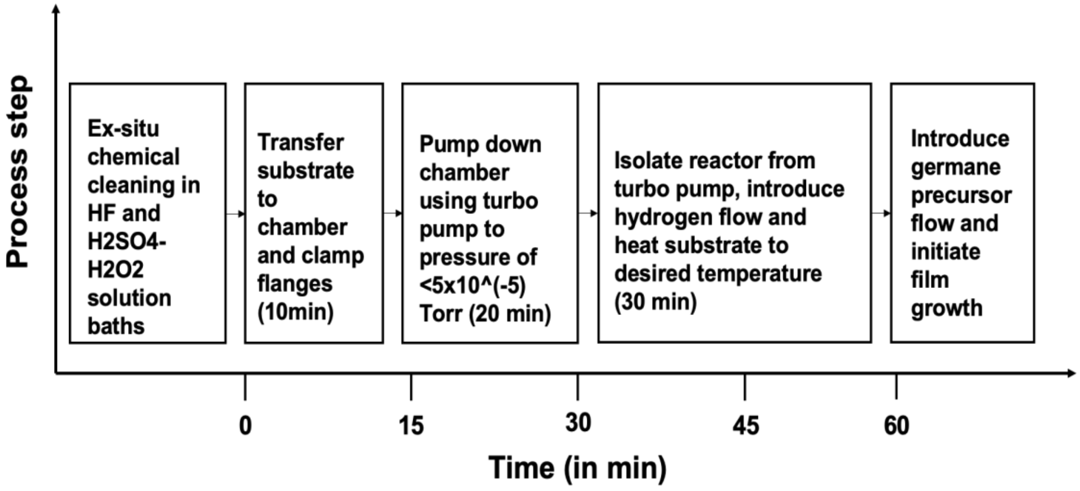

FIG. 5.1.2 Optimized process flow for deposition of epitaxial Ge films at high background chamber pressure

From Fig. 5.1.1 a, it can be seen that, with the chamber pressure maintained at 10 Torr, the film growth rate increases with increase in the GeH_4 partial pressure, for both substrate temperatures. This is because of the higher flux of precursor molecules available for dissociation and deposition at higher partial pressures. The film growth rate is higher at 385^{o}C than at 350^{o}C for the same GeH_4 partial pressure. Amongst the factors which determine the growth rate of Ge on are the availability of free sites for adsorption of reactant species and the rate of the surface reactions (i.e. dissociation and migration) (Ishii, Takahashi, and Murota 1985).

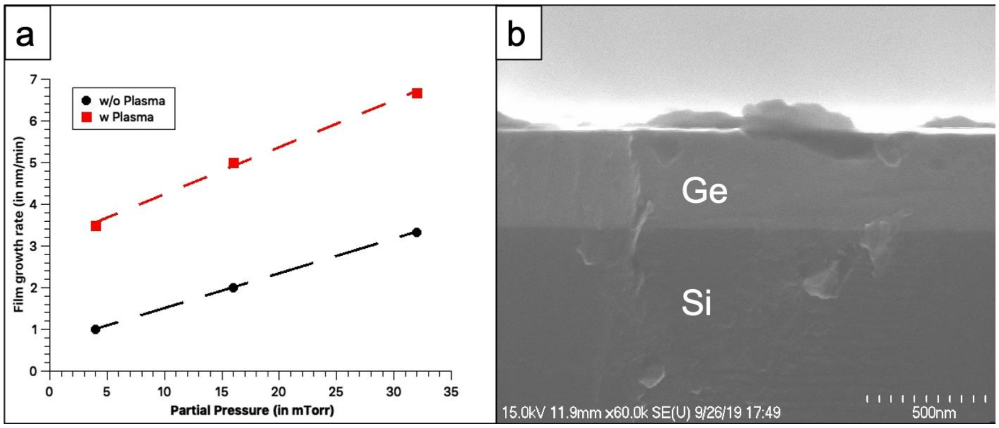

FIG. 5.1.3. (a) Growth rate of Ge films at different GeH_4 partial pressures at chamber pressure of 10 Torr and substrate temperatures 350^{o}C with and without plasma enhancement (b) SEM image of the cross section of the Run 12 film

With increasing substrate temperature, the coverage of surface by H decreases and the number of sites for adsorption increases (Eres and Sharp 1993). Also, the higher thermal energy at higher substrate temperature increases the rate of the surface reactions. Thus, the film growth rate increases with increase in temperature. However, at 350^{o}C, the film growth rate increases linearly with partial pressure while at 385^{o}C, it increases rapidly initially and then saturates. While the exact reason for this behavior is not clear, the most likely cause is that at the higher temperature and partial pressure, a fraction of the reaction species might be transported to the sides of the reactor due to the higher collision frequency and thermal energy and thus not reach the substrate to contribute to film growth (Fensham 1955; Kobayashi et al. 1990).

From Fig. 5.1.3 a, it can be seen that film growth rate is higher for films grown with plasma enhancement than without any plasma enhancement. This implies that the presence of plasma during growth increased the cracking of the Ge hydride source. This is due to the kinetic energy provided by the high energy ions and radicals present in the plasma leading to enhanced precursor dissociation (Dou, Alharthi, et al. 2018). Also, the growth rate increases linearly with increase in partial pressure indicating that the films still grow by planar growth method which is most likely due to the lower temperature (i.e 350^{o}C) used during growth.

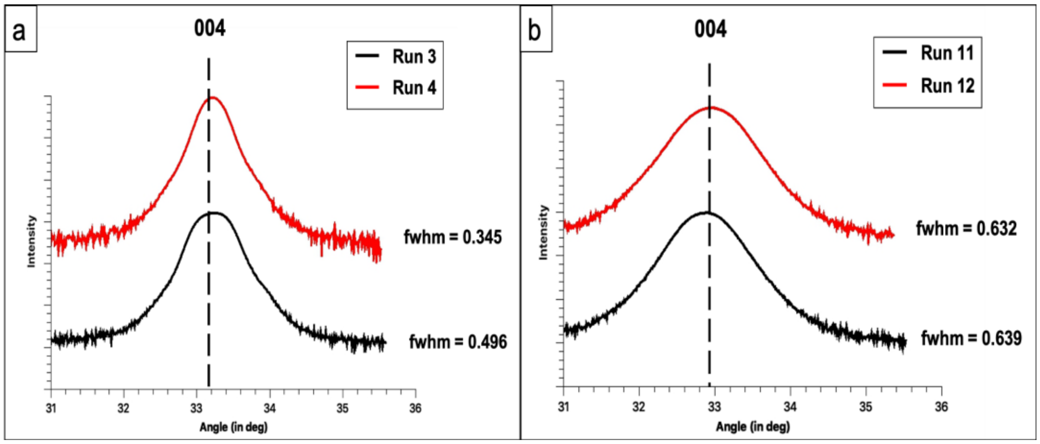

FIG. 5.1.4. (a) X-ray rocking curve of Ge films deposited at 10 Torr and different GeH_4 partial pressures at substrate temperature of 385^{o}C. (b) X-ray rocking curve of Ge films deposited at 350^{o}C with plasma enhancement

From Fig. 5.1.4 a, it can be seen that the FWHM of the X-ray rocking curves of the films deposited at 385ºC decreases with increasing GeH_4 partial pressure. Since the FWHM of the rocking curve is a measure of the crystalline quality of deposited films, this implies that higher partial pressure greatly improves the material quality of the films deposited at 385ºC. This is due to the difference in films growth rates obtained under different growth conditions. Lower growth rates would allow for impurities such as background oxygen to incorporate in the depositing film due to the non-UHV CVD conditions (Olubuyide et al. 2006). This would cause imperfections in the crystal lattice such as point defects and dislocations leading to the degradation of the crystal quality. This phenomenon would be limited at the higher growth rates and would thus result in a film with better crystalline quality. However, for the films deposited with plasma enhancement, the FWH of the X-ray rocking curves (and thus the material quality) does not change with change in GeH_4 partial pressure. While the increase in growth rate should restrict the inclusion of background impurities in the films, the bombardment of the crystal lattice from the high energy species present in the plasma might be leading to lattice defects (such as broken bonds) and thus result in material quality degradation (Alharthi et al. 2019).

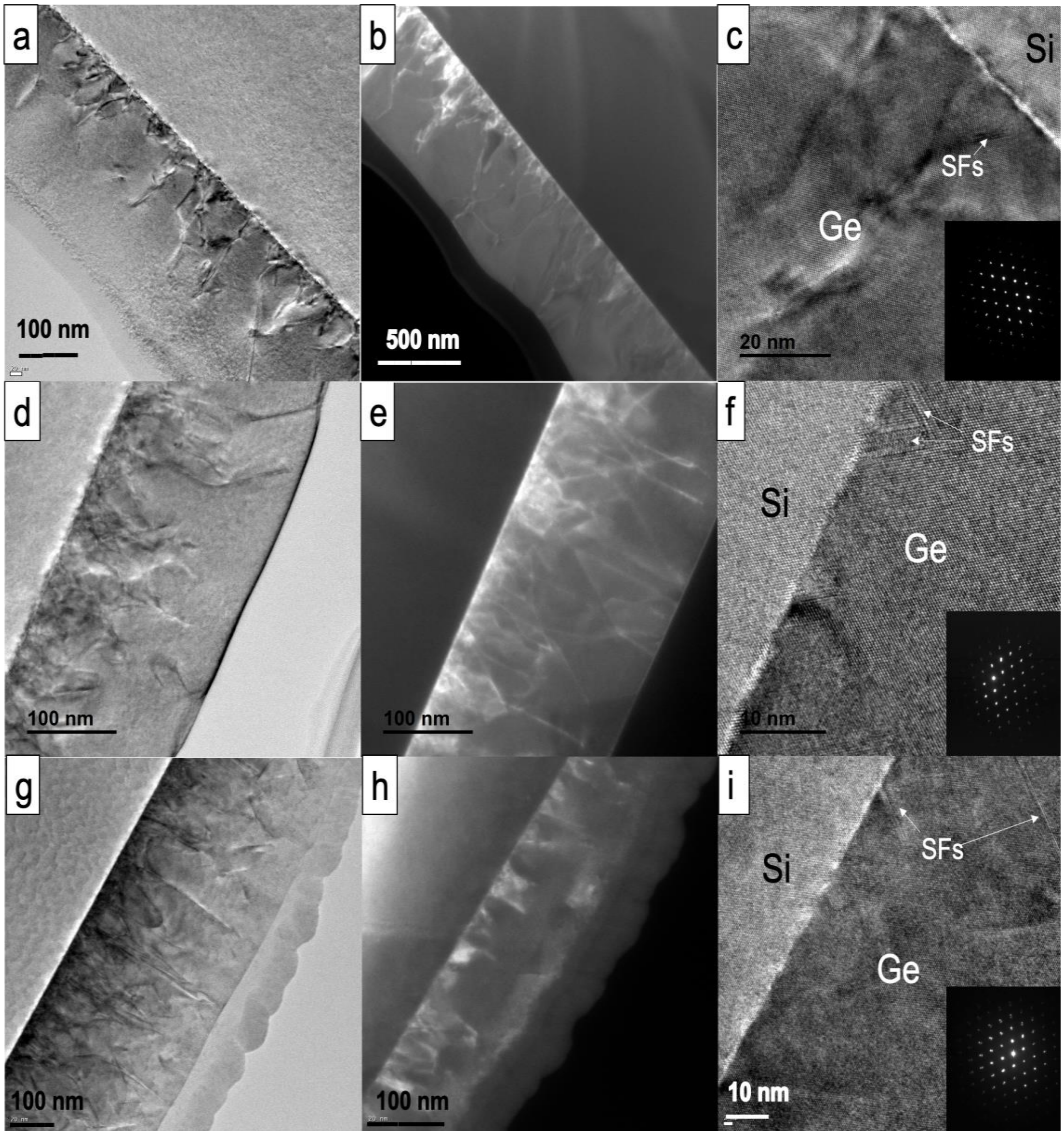

FIG. 5.1.5. (a-c) TEM image and diffraction pattern (inset in Fig 5.1.5 c) of Ge film deposited in Run 4. (d-f) TEM image and diffraction pattern (inset in Fig 5.1.5 f) of Ge film deposited in Run 8. (g-i) TEM image and diffraction pattern (inset in Fig 5.1.5 i) of Ge film deposited in Run 12. The TEM images confirm the epitaxial growth and good crystalline quality of the deposited films with electron diffraction pattern of the Ge layer showing cubic symmetry

Figure 5.1.5 shows the dark and bright field TEM images of the epitaxial Ge film deposited in Runs 4, 8 and 12 at different magnifications along with the electron diffraction pattern. As seen from the TEM images, the Ge layer has high crystallinity with periodic atomic arrangement. Some regions in the images have a dark contrast which is because of electron clouding process and stress distribution (Kil et al. 2016). A high concentration of lattice imperfections such as dislocations and stacking faults are concentrated near the interface between the Si substrate and Ge film. Some of the stacking faults (SFs) are observed in the high magnification TEM image as marked in Fig 5.1.5 c, f, i. The SFs occur to relieve the strain in the film occurring due to the large lattice mismatch between the Si and Ge and the difference in their coefficients of thermal expansion (Kil et al. 2016; Luan et al. 1999). A clear improvement in the crystalline quality is observed moving away from the interface towards the surface corresponding to decreasing strain in the lattice. The diffraction patterns confirm the cubic symmetry of the Ge films and the absence of any rings in the pattern confirm the absence of any polycrystalline or amorphous growth.

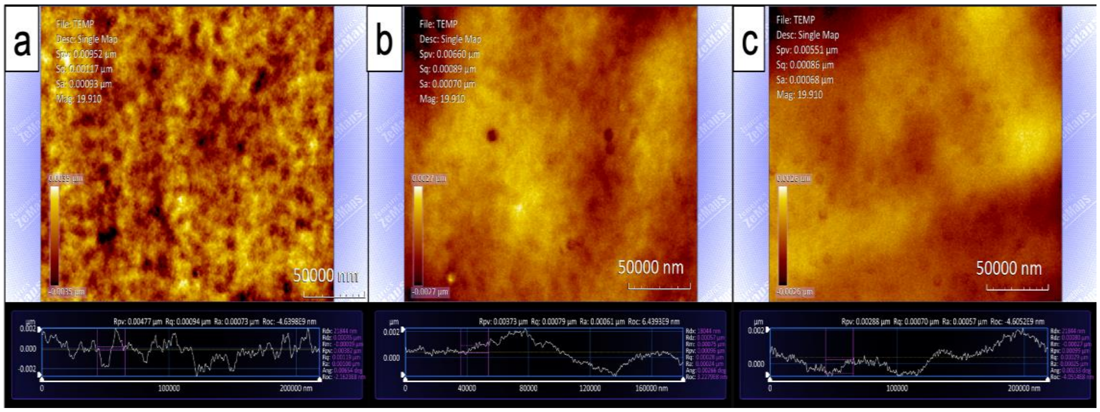

FIG. 5.1.6. Optical profile of the surface of the Ge films deposited in (a) Run 4 (b) Run 8 and (c) Run 12 showing highly smooth surfaces

Fig 5.1.6 shows the optical profile of the surface of the films deposited in Runs 4, 8 and 12. It can be seen that the roughness of the films (Ra) is less than 1 nm in all cases.

This proves that the deposited films are highly smooth which is essential when the films need to be used as buffers or waveguides. This further confirms that the films are deposited in a planar manner even with high energy plasma enhancement and no island growth takes place during film deposition. This is likely because of the low temperature maintained during film deposition.

Table 5.1.2 provides a comparison of the Ge films achieved with the process developed here with other attempts of Ge-on-Si growth using a one-step technique without any post growth annealing step.

Table 5.1.2. Comparison of material quality of Ge films demonstrated by other research groups with this work

No	Technique	Temperature (ºC)	Chamber Pressure (Torr)	GeH_4 partial pressure (mTorr)	Growth rate (nm/min)	FWHM (degrees)	RMS (nm)	Ref.
1	RPCVD	350	20	4000	0.2	NA	1.3	Kil (2016)
2	UHVCVD	350	0.5	142.8	2.4	0.478	NA	Grant (2017)

3	RPCVD	385	10	32	10	0.345	NA	This work
4	PECVD	250	0.5	10	1.09	0.707	10.5	Littlejohns (2015)*
5	PECVD	200	2	47.5	0.5	NA	1.6	Cariou (2014)
6	PECVD	350	10	32	6.7	0.639	< 1	This work

* - Sample B

It can be seen that the films achieved in this report are comparable in material quality to films reported in the other works. The films achieved without any plasma enhancement (i.e. RPCVD) demonstrated higher growth rates and lower FWHM values at lower precursor partial pressures. Also, a higher growth temperature (and thus a higher growth rate) could be utilized while depositing films with plasma enhancement without any deterioration in the film quality.

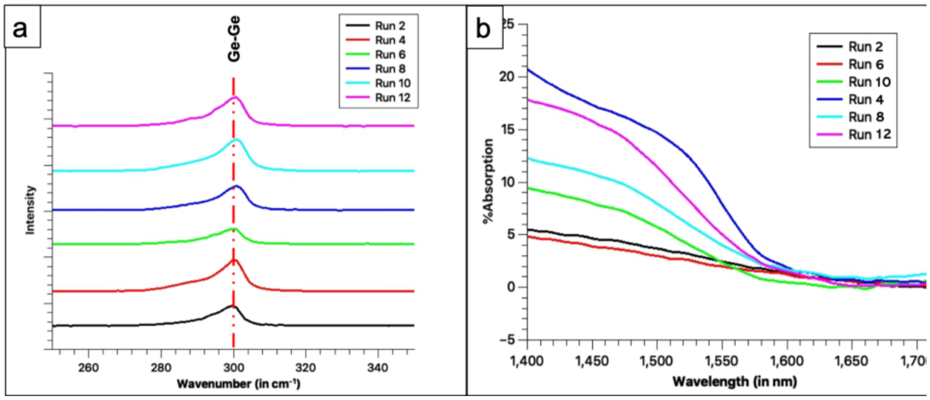

FIG. 5.1.7. (a) Raman spectra of Ge films deposited under various conditions (b) Room temperature IR absorption spectra of Ge films deposited under various conditions

The Raman spectra of the films deposited at low partial pressure (4 mTorr) and high partial pressure (32 mTorr) at different substrate temperatures is shown in Fig. 5.1.7 a. A sharp peak corresponding to the Ge-Ge phonon mode can be seen in all the spectra indicating the high material quality of the films. The strain present in the films can be calculated from the peak shift using the following equation:

$$\varepsilon = \frac{\omega_{Ge-Ge} - \omega_0^{Ge}}{b_{Ge-Ge}} \qquad (5.1.1)$$

where ε is the strain in the film, ω_{Ge-Ge} is the observed Raman peak shift for the Ge-Ge bond, ω_0^{Ge} corresponds to the peak shift for the Ge-Ge bond in bulk Ge i.e $\omega_0^{Ge} = 301\ cm^{-1}$ and $b_{Ge-Ge} = -415\ cm^{-1}$ (Fournier-Lupien et al. 2013). The observed peak position and the calculated strain for the films are given in Table 5.1.3.

Table 5.1.3. Raman peak positions and calculated strain for Ge films

Run no.	Film thickness (nm)	Ge-Ge peak position (cm-1)	Calculated strain %
2	75	300.27	0.17
4	600	300.87	0.03
6	60	300.14	0.21
8	200	300.88	0.03
10	210	300.88	0.03
12	400	300.97	0.007

It can be seen that the films obtained from runs 2 and 6 have a larger strain present (0.2%) while the remaining films have negligible strain (<0.05%). This is most likely due to the difference in the thickness of the deposited films. The films from runs 2 and 6 have thickness ≤100 nm while the remaining films are much thicker. The thicker films relieved the strain arising from the difference in the lattice parameter between Ge and Si substrate through the formation of misfit dislocation at the film-substrate interface and thus are completely relaxed (Kil et al. 2016; Luan et al. 1999). The thickness of the films from runs 2 and 6 might not be sufficient to cause misfit dislocations and thus larger strain is present in the films. Fig. 5.1.7 b shows the absorption spectrum of the films. It can be seen that all the films have a cut-off wavelength of ~1600 nm which is close to bulk Ge (Dash and Newman 1955). It can also be seen that the films from runs 2 and 6 have much lower absorption than the remaining films. This can again be attributed to the difference in thicknesses of the films. Since the amount of incident light absorbed is directly proportional to the thickness of the semiconducting film, the thinner films will be able to absorb a lower fraction of the incident light as opposed to the thicker films as observed (Aly and Akl 2015).

5.2 Epitaxial Ge film growth using Ge_2H_6 precursor

While Ge_2H_6 is more expensive than the conventionally used reactive GeH_4, it is more reactive at low growth temperatures compared to GeH_4 and thus provides higher growth rates, better crystallinity and smooth surface morphology at low process temperatures (Aubin et al. 2016; Gencarelli et al. 2012).

Ge_2H_6 (10% in Argon) and GeH_4 (10% in Argon) were used as the Ge precursors for this study. The partial pressure of the pressure of the precursor was maintained at 4 mTorr and was calculated by obtaining the ratio of the precursor flow rate to the total gas flow rate and then multiplying the ratio with the total chamber pressure. Ge films were deposited at a substrate temperature of 350^{o}C. The films were deposited at chamber pressures in the range of 1-10 Torr. The precursors were flown for a duration of 50-75 minutes to deposit the Ge films. The conditions used to deposit the films are given in the table 5.2.1.

The crystal structure and crystalline quality of the films were determined by XRD spectra and rocking curve measurements, using PANalytical XPert Pro MRD diffractometer with Cu Kα radiation. SEM images of the cross section of the films were obtained using a Hitachi S-4700-II scanning electron microscope to observe the morphology and thicknesses of the obtained films. TEM was carried out using a Philips CM200-FEG high resolution TEM at an accelerating voltage of 200kV to analyze crystalline structure and defects in the films. Room temperature PL measurement was carried out using a standard off-axis configuration with a 1064 nm 500mW pulsed laser (6 ns 45kHz) as the excitation source. The emission was collected by a spectrometer equipped with a thermoelectrically cooled lead sulfide detector with response cut-off at 3.0 μm. IR spectroscopy was done at room temperature using a Perkin Lambda 950 UV/Vis/NIR spectrometer in the wavelength range of 1500-2200 nm to analyze the absorption properties of the films. The absorption spectrum of the films was obtained by collecting the reflectance (%R) and transmittance (%T) spectra of the film and then subtracting the sum of the values from 100. Raman spectroscopy was performed at room temperature by using a 532 nm 50 mW green laser coupled to a WiTec Alpha300R Confocal Raman Imaging system. A Princeton Instruments Acton SP2300 imaging spectrograph was used to analyze the nature of strain present in the films.

Table 5.2.1. Conditions used to deposit Ge films using Ge_2H_6 precursor

Run No.	Ge precur-sor	Turbo-pumping before growth	Substrate temperat-ure (^oC)	Chamber pressure (Torr)	Precursor flow rate (sccm) (Partial pressure in mTorr)	Hydrogen flow rate (sccm)	Deposi-tion time (min)	Film thick-ness (nm)
1	Ge_2H_6	No	350	10	20 (4)	4980	50	650
2	Ge_2H_6	Yes	350	1	20 (4)	480	75	750
3	Ge_2H_6	Yes	350	10	20 (4)	4980	50	675
4	GeH_4	Yes	350	1	20 (4)	480	50	NA
5	GeH_4	Yes	350	10	20 (4)	4980	50	NA

5.2.1 Results and Discussions

Figure 5.2.1 (a) shows the 2θ-ω powder XRD spectra of Ge films deposited using Ge_2H_6.The spectra have been obtained between the angles of 25-75^o to locate peaks belonging to the Ge cubic lattice system. A 2^o ω offset was used during the scans. This was done to prevent the strong signal from the single crystalline Si substrate saturating the detector. As a result, the peak belonging to the Si (100) plane at 69.12^o is observed as a broad peak in the scans instead of as a sharp peak.

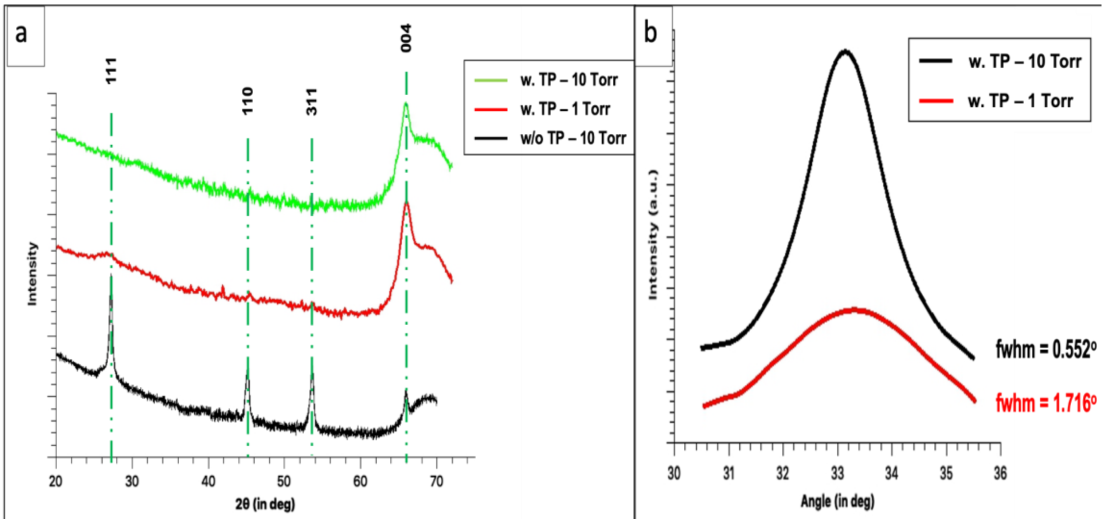

FIG. 5.2.1. (a) XRD spectra of Ge films grown using Ge_2H_6 at 350^{o}C and different chamber pressures showing epitaxial growth after turbo pumping (w. TP) and polycrystalline growth without turbo pumping (w/o TP) and (b) Rocking curve of the epitaxial Ge films showing better crystalline growth at higher chamber pressure

The cause of the background is the noise from the XRD tool. For the film deposited without any turbo pumping prior to film growth, peaks belonging to the Ge (111), Ge (110), Ge (311) and Ge (004) planes can be observed. For the films deposited after turbo pumping of the chamber, only peaks belonging to the Ge (004) orientation (located at 66^{o}) can be observed. This proves that the Ge films are deposited in an epitaxial manner over the Si substrate under these conditions (Grant et al. 2017). Since the mechanical pumps can only pump the chamber pressure down to ~10^{-2} Torr, a high concentration of oxygen and water vapor is still present in the chamber. This reacts with the Si surface and lead to the formation of SiO_2 islands on the surface which hinder epitaxial growth of the Ge films. The use of turbo pumping before film growth significantly decreases the concentration of oxygen and water vapor. The turbo pump reduces the background pressure to ~$5x10^{-5}$ Torr. Inspite of the high chamber background pressure (>10^{-6} Torr), the optimization of the timings taken for turbo pumping of the chamber once the wafers have been transferred and the commencement of film deposition allows for epitaxial deposition of good quality films. From the values of the full-width half maximum (FWHM) of the rocking curve peaks (which is calculated by fitting a Gaussian model to the peaks), it is clear that the film deposited at 10 Torr is of a much better crystalline quality than the film deposited at 1 Torr. The explanation for this will be provided in the following section along with the SEM imaging discussion.

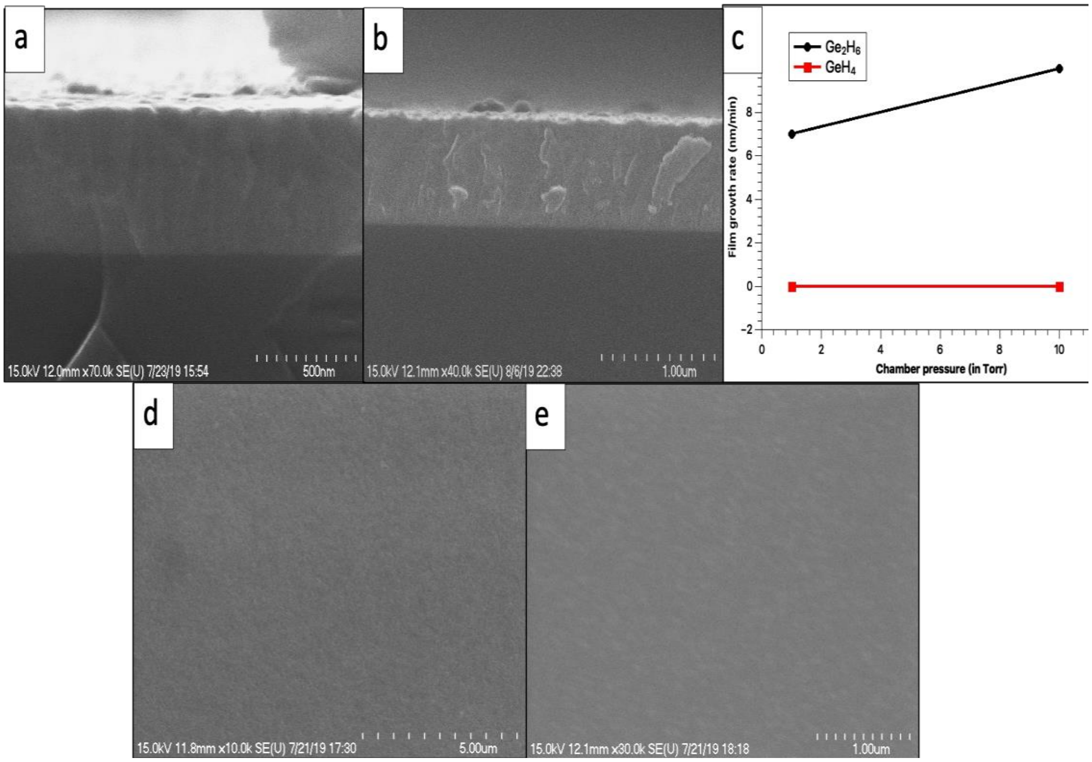

FIG. 5.2.2. Cross section SEM image of the epitaxial Ge films grown using Ge_2H_6 at (a) 10 Torr and (b) 1 Torr. (c) Film Growth rate vs chamber pressure for Ge films grown using Ge_2H_6 and GeH_4. Top section SEM image of the epitaxial Ge films grown using Ge_2H_6 at (d) 10 Torr and (e) 1 Torr.

Figure 5.2.2 a and b shows the cross section and Figure 5.2.2 d and e the top section SEM images of the epitaxial films grown using Ge_2H_6. It is evident from the surface SEM images that the surface morphology is smooth. The calculated growth rates for the films were 7 nm/min for the film growth at 1 Torr and 10 nm/min for the film grown at 10 Torr. The growth rates observed are similar to those reported in other works for similar conditions (Gencarelli et al. 2012). The increase in film growth rate with increase in chamber pressure can be attributed to the difference in the mean free path of the moieties inside the growth chamber and the residence time of the precursor at the substrate surface at the different chamber pressures (Senftleben, Baumgärtner, and Eisele 2008; Asafa 2013). The mean free path λ is given by the following equation:

$$\lambda = \frac{k_B * T}{\sqrt{2}\pi * d^2 * P} \quad (5.2.1)$$

Where k_B is the Boltzmann constant, T is the growth temperature, d is the gas molecule diameter (3.99Å for digermane) and P is the chamber pressure. The value of λ is 87.8 μm for chamber pressure of 1 Torr and 8.78 μm for chamber pressure of 10 Torr. As the chamber pressure increases, the mean free path decreases leading to higher frequency of collisions between the precursor molecules in the gas phase (Alharthi et al. 2018). The energy from the collisions leads to a portion of the precursor molecules dissociating before reaching the substrate and thus result in a higher growth rate at the higher pressure . The reactions more likely to occur at higher chamber pressures are shown below ($\underline{X}$ indicates a surface adsorbed atom).

a. $Ge_2H_6 + Ge_2H_6 \rightarrow GeH_3 + GeH_3 + Ge_2H_6$

b. $GeH_3 + H - \underline{Ge} \rightarrow H - \underline{Ge} - \underline{Ge} + 1.5H_2$

c. $GeH_3 + H - \underline{Ge} \rightarrow GeH_4 + -\underline{Ge}$

The higher chamber pressure also leads to a higher residence of the precursor molecules at the substrate surface leading to a higher probability of the precursor adsorbing to the surface and contributing to film growth.

The difference in the growth rates also explains the difference in the film crystalline quality observed from the XRD results. The lower growth rate at 1 Torr would allow for impurities such as background oxygen to incorporate in the depositing film due to the non-UHV CVD conditions. This would cause imperfections in the crystal lattice such as point defects and dislocations leading to the degradation of the crystal quality. This phenomenon would be limited at the higher growth rate achieved at 10 Torr and would thus result in a film with better crystalline quality.

Attempts to deposit films using GeH_4 as the precursor at the same conditions did not result in any growth (this was confirmed by XRD and Raman characterization). This is because the Ge-Ge bond in Ge_2H_6 is much weaker than the Ge-H bond In GeH_4 and breaks much more efficiently at lower temperatures. This shows that Ge_2H_6 is a useful Ge precursor for applications having thermal constraints.

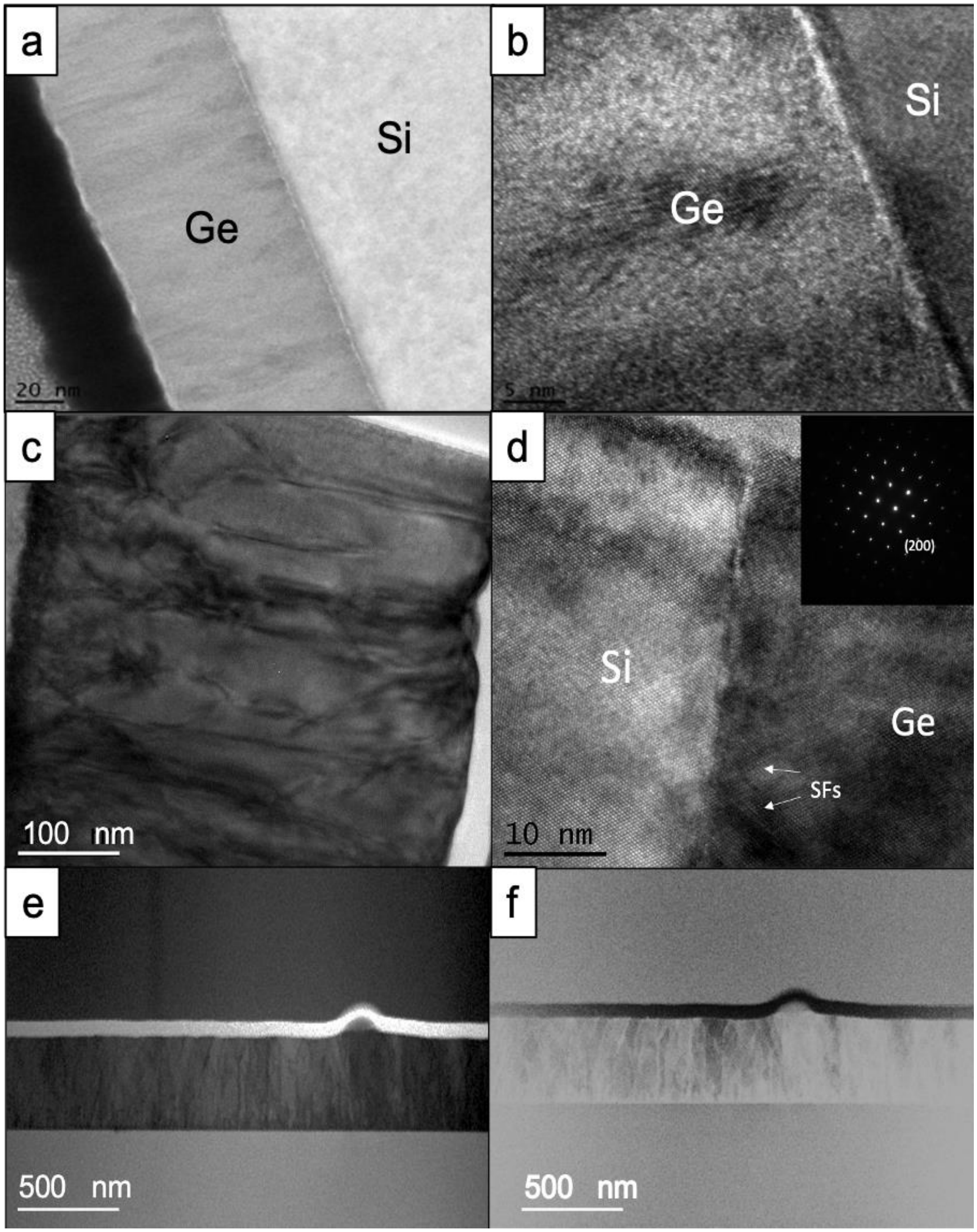

FIG. 5.2.3. (a) Low magnification and (b) High magnification TEM image of Ge film and Si interface showing presence of native oxide due to film grown without any turbo pumping. (c-f) TEM images of Ge film grown at 10 Torr after turbo pumping using Ge_2H_6 showing epitaxial growth and good crystalline quality with electron diffraction pattern of the Ge layer showing cubic symmetry (inset in Fig. 5.2.3 d)

Figure 5.2.3 a and b shows TEM images of Ge films deposited without any turbo pumping. The polycrystalline nature was of the films was confirmed by TEM imaging of the cross section of the deposited films. Short range domains were observed in the high magnification (500kX) TEM images. The TEM images confirm the presence of native oxide several angstroms thick present on the substrate (the white band at the interface in the high magnification TEM image). Thus, films deposited without turbo pumping are polycrystalline due to the presence of the oxide layer at the interface. Figure 5.2.3 c and d shows TEM images the epitaxial Ge film deposited using Ge_2H_6 at 350^{o}C with a chamber pressure of 10 Torr after turbo pumping at different magnifications along with the electron diffraction pattern. As seen from the TEM images, the Ge layer has high crystallinity with periodic atomic arrangement. Some regions in the images have a dark contrast which is because of electron clouding process and stress distribution. A high concentration of lattice imperfections such as dislocations and stacking faults are concentrated near the interface between the Si substrate and Ge film. Some of the stacking faults (SFs) are observed in the high magnification TEM image as marked in Fig 5.2.3 d. The SFs occur to relieve the strain in the film occurring due to the large lattice mismatch between the Si and Ge and the difference in their coefficients of thermal expansion. A clear improvement in the crystalline quality is observed moving away from the interface towards the surface corresponding to decreasing strain in the lattice. Figure 5.2.3 e and f are bright-field and dark-field STEM images of the Ge film with gold contact deposited on top of the film as part of TEM sample preparation. The images show the film at a lower magnification than in Fig 5.2.3 c and d. The images demonstrate the achieved high crystalline quality of the film over a wider area (in micron range). The lattice constant was calculated using the Eq. 5.2.2 and the diffraction spot along the [200] direction in the electron diffraction pattern:

$$R * d_{hkl} = L * \lambda \qquad (5.2.2)$$

Where R is the distance between collision points of transmitted and diffracted beams on the screen, d_{hkl} is the interplanar distance, L is the effective camera length and λ is the wavelength associated with the electron beam. The obtained value of the film lattice constant was 5.66Å. This is similar to bulk Ge indicating that the deposited Ge layer is fully strain relaxed.

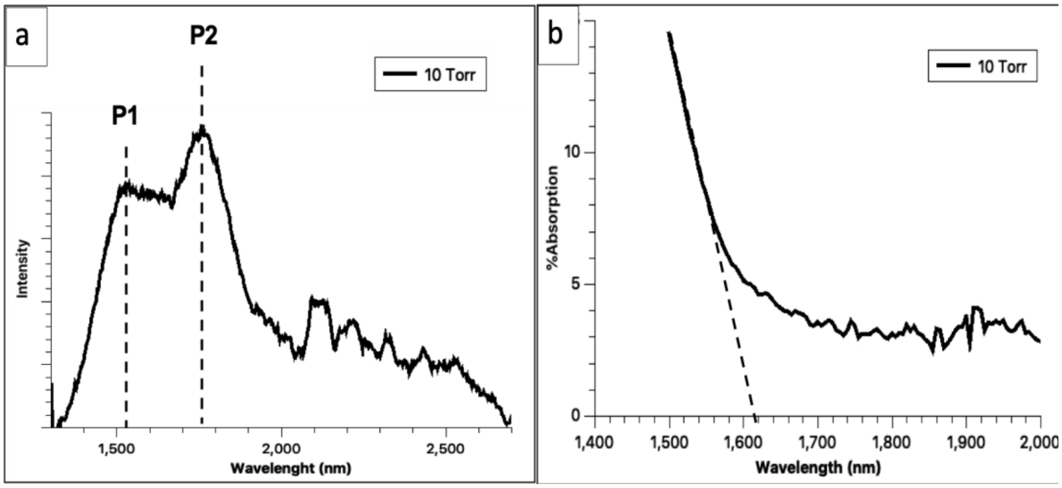

FIG. 5.2.4. (a) Room temperature PL spectrum of epitaxial Ge film grown at 10 Torr using Ge_2H_6 showing indirect and direct band gap transitions and (b) Absorption spectrum of Ge film grown at 10 Torr showing onset of absorption at wavelength corresponding to indirect band gap

Fig. 5.2.4 (a) shows the PL spectrum of the epitaxial Ge film deposited at chamber pressure of 10 Torr. It can be seen that the films exhibit strong photoluminescence at room temperature which is indicative of high crystalline quality. Two peaks can be observed in the PL spectrum marked as P1 and P2 in Fig. 5.2.4 (a).

These peaks are centered at 1530 nm (0.81 eV) and 1775 nm (0.69 eV) respectively and thus correspond to the direct band gap transition (at the Γ-point) and indirect band gap transition (at the L-point) in Ge(Alharthi et al. 2018; Grant et al. 2017). At room temperature, the thermal activation energy is sufficient to transfer a portion of the photo generated electrons from the L-valley to the Γ-valley due to the small energy difference between the bands resulting in significantly enhanced direct band gap emission (Zhou et al. 2016). No PL signal could be obtained from the film deposited at 1 Torr due to its relatively poor crystalline quality. Fig. 5.2.4 (b) shows the absorption spectrum of the Ge film deposited at chamber pressure of 10 Torr. This was obtained by collecting the reflectance (%R) and transmittance (%T) spectra of the film and then subtracting the sum of the values from 100. It can be seen that the film has a cut-off wavelength of ~1600 nm which is close to bulk Ge. The strong room temperature PL and optical absorption further corroborate the high crystalline quality of the deposited film.

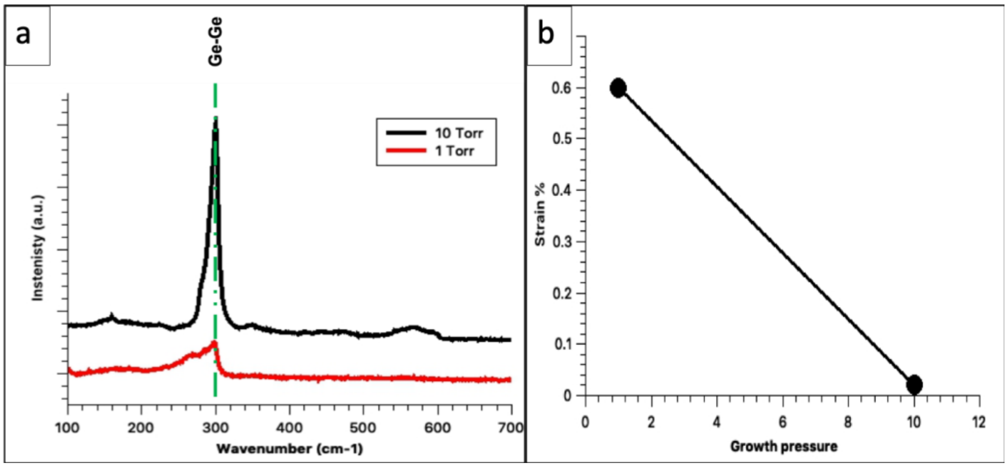

FIG. 5.2.5. (a) Raman spectra of Ge films grown using Ge_2H_6 at 350ºC and different pressures and (b) Strain in the Ge films obtained from Raman peak shifts

The Raman spectra of the epitaxial films is shown in Fig. 5.2.5. Peaks belonging to the Ge-Ge bond is clearly seen for both films. However, the film deposited at 10 Torr has a narrow high intensity peak while the one deposited at 1 Torr has a broad peak. This can be assigned to the difference in crystalline quality between these two films. The strain in the films was calculated by Eq. (5.2.3) given in Lupien et al (2013).

$$\varepsilon = \frac{\omega_{Ge-Ge} - \omega_0^{Ge}}{b_{Ge-Ge}} \qquad (5.2.3)$$

where ε is the strain in the film, $\omega_{Ge-Ge}$is the observed Raman peak shift for the Ge-Ge bond, ω_0^{Ge} corresponds to the peak shift for the Ge-Ge bond in bulk Ge i.e $\omega_0^{Ge} = 301\ cm^{-1}$ and $b_{Ge-Ge} = -415\ cm^{-1}$. The film deposited at 10 Torr has negligible strain (<0.02%) which matches the result of TEM electron diffraction pattern analysis of the film. The obtained strain for the film deposited at 1 Torr was 0.6%. The strain in the film deposited at 1 Torr arises from the various microstructural imperfections present in the films due to the lower growth rate, as discussed in the XRD analysis. Since the higher growth at the higher chamber pressure limits this occurrence and majority of the strain is relieved in the lower portion of the film (i.e. at the Si substrate interface through dislocations), the strain observed for the film deposited at 10 Torr is significantly lower.

5.3 Deposition of epitaxial GeSn films without any plasma enhancement

A Ge buffer film was first deposited on the Si (100) substrate by flowing GeH_4 (10% in Ar) at 80 sccm at 385^{o}C substrate temperature and chamber pressure of 10 Torr by CVD without any plasma enhancement for a duration of 60 min. GeSn films were then deposited on top of the Ge buffer films by flowing GeH_4 (10% in Ar) and SnCl4 (99.999%) at 150 sccm and 10 sccm respectively without any plasma enhancement at substrate temperature of 320-350^{o}C and chamber pressure of 10 Torr for a duration of 45 min.

The crystalline quality of the deposited of films were analyzed from XRD spectra obtained from PANalytical XPert Pro MRD diffractometer with Cu Kα radiation. The elemental profile of the deposited thin films was measured by using RBS measurements carried out using a 1.7 MV Cockroft-Walton, gas-insulated high-frequency Tandem accelerator with a beamline and analysis chamber. 2MeV He^{2+} ions were used as the ion source.

5.3.1 Results and Discussions

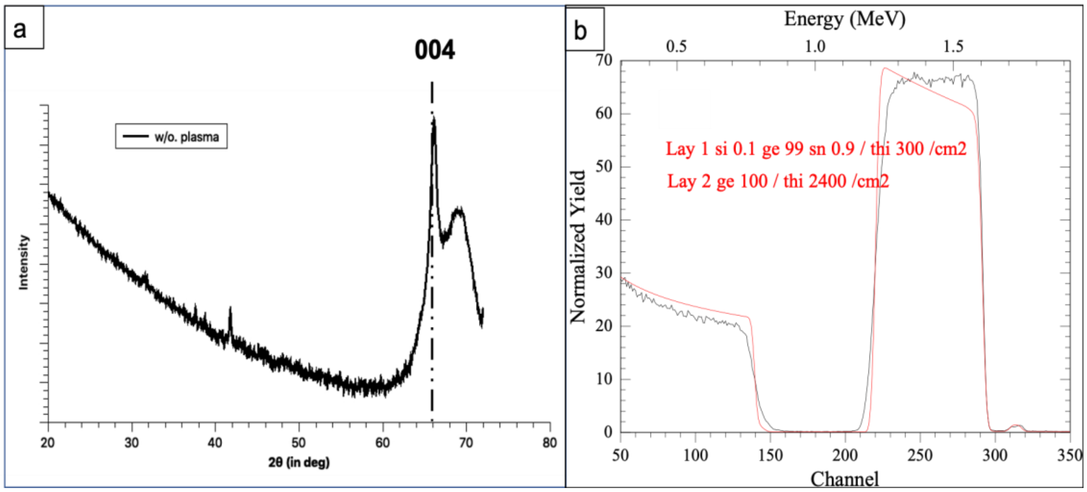

FIG. 5.3.1 (a) XRD spectra and (b) RBS spectrum and RUMP simulation of epitaxial GeSn films deposited without plasma enhancement

Fig 5.3.1 a shows the XRD spectra of GeSn film without any using plasma enhancement at substrate temperature of 350^{o}C. Only peaks belonging to the Ge (004) orientation (located at 66^o) can be observed. This proves that the GeSn films are deposited in an epitaxial manner over the Si substrate. Fig 5.3.1 b shows the RBS spectra of GeSn film. RBS analysis showed that films with Sn% of up to 1% were achieved with Ge:Sn precursor ratio of 10:1. The thickness of the films deposited was ~60 nm which computes to a growth rate of 2 nm/min. Trying to increase the Sn% by decreasing the growth temperature or by decreasing the Ge:Sn precursor ratio was not successful as it resulted in no film growth taking place. At the lower temperature, the thermal energy provided is insufficient to break down the precursors leading to no film deposition. At high Sn:Ge ratios, the etching effects due to the Cl_2 and HCl which are formed due to the dissociation of $SnCl_4$ dominate over the film growth rate.

5.4 Deposition of epitaxial GeSn films with plasma enhancement

A Ge buffer film was first deposited on the Si (100) substrate by flowing GeH_4 (20% in Ar) at 40 sccm at 385^{o}C substrate temperature and chamber pressure of 10 Torr by CVD without any plasma enhancement for a duration of 30 min. GeSn films were then deposited on top of the Ge buffer films by flowing GeH_4 (20% in Ar) and SnCl4 (99.999%) at varying flow rate ratios (by varying the Ge precursor flow rate from 200-300 sccm and keeping the Sn precursor flow rate at 10 sccm) with plasma enhancement at substrate temperatures in the range of 300-350^{o}C and chamber pressure of 15 Torr for a duration of 35 min.

The crystalline quality of the deposited of films were analyzed from XRD spectra obtained from PANalytical XPert Pro MRD diffractometer with Cu Kα radiation. The elemental profile of the deposited thin films was measured by using RBS measurements carried out using a 1.7 MV Cockroft-Walton, gas-insulated high-frequency Tandem accelerator with a beamline and analysis chamber. 2MeV He^{2+} ions were used as the ion source.

5.4.1 Results and Discussions

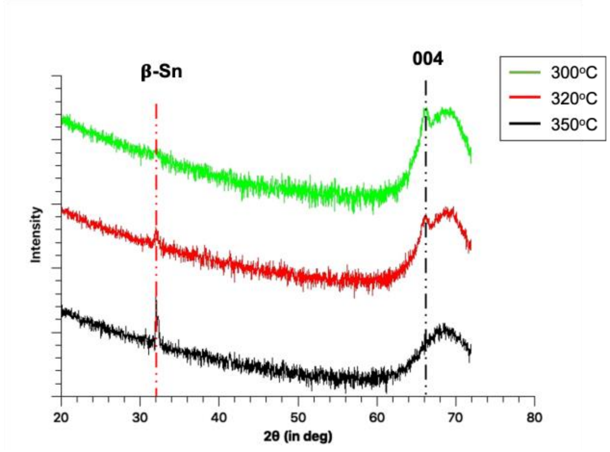

FIG. 5.4.1. XRD spectra of epitaxial GeSn films deposited with plasma enhancement at different substrate temperatures

Fig 5.4.1 shows the XRD spectra of GeSn films deposited at chamber pressure of 15 Torr and Ge and Sn precursor flow rates of 300 sccm and 10 sccm respectively at different substrate temperatures using plasma enhancement. Film growth could be achieved at temperatures below 350^{o}C with plasma assistance as the plasma provided additional energy along with the thermal energy to cause a fraction of the precursors in the gas phase to undergo dissociation leading to film deposition. β-Sn peaks can be seen in the spectra for the films grown at 350^{o}C and 320^{o}C but it is not present in the film grown at 300^{o}C. This proves that no Sn segregation takes place in the film grown at 300^{o}C while films grown at higher temperature undergo Sn segregation. This is because at the higher thermal energy available at the higher growth temperatures, the Sn radicals diffuse through the film and undergo coalescence and Ostwald ripening leading to Sn segregation.

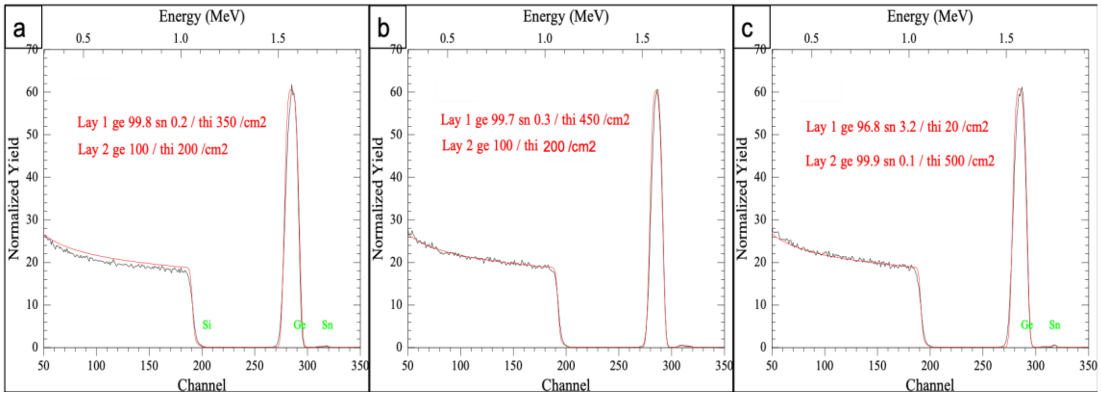

FIG. 5.4.2 RBS spectrum and RUMP simulation of epitaxial GeSn films deposited at different Ge:Sn precursor flow rates

Fig 5.4.2 shows the RBS spectra of GeSn films deposited at different ratios of Ge/Sn precursor flow rates at growth conditions of 300^{o}C and chamber pressure 15 Torr. It can be seen that as the ratio of Ge/Sn decreases the Sn concentration in the film increases. Thus, the composition of the film can be tuned by varying the precursor flow ratios. Films with Sn% from 0.2 - 3% were achieved. This is higher than the thermodynamic solubility of Sn in Ge implying that the process is nonequilibrium in nature. Attempting to increase the Sn% in the films by further decreasing the Ge/Sn resulted in no film growth. This is because as the Ge concentration in the gas phase decreases, the film growth rate decreases. Also, dissociation of $SnCl_4$ leads to Cl_2 and HCl being formed as by products. These species act as etchants and further diminish the overall film growth rate.

5.5 Doping of GeSn films using diborane and phosphine

A Ge buffer film was first deposited on the Si (100) substrate by flowing GeH_4 (20% in Ar) at 40 sccm at 385^{o}C substrate temperature and chamber pressure of 10 Torr by CVD without any plasma enhancement for a duration of 30 min. GeSn films were then deposited on top of the Ge buffer films by flowing GeH_4 (20% in Ar) and SnCl4 (99.999%) at 250 sccm and 15 sccm respectively with plasma enhancement at substrate temperature of 300^{o}C and chamber pressure of 15 Torr for a duration of 30 min. The films were doped with boron and phosphorus by flowing diborane (B_2H_6 100 ppm in H_2) and phosphine (PH_3 100 ppm in H_2) respectively along with the Ge and Sn precursors. The dopant flow rates were varied from 20-150 sccm.

The crystalline quality of the deposited of films were analyzed from XRD spectra obtained from PANalytical XPert Pro MRD diffractometer with Cu Kα radiation. The elemental profile of the deposited thin films was measured by using SIMS measurements carried out using a Cameca IMS 3f secondary ion mass spectrometer and an O_2^+ ion beam.

5.5.1 Results and Discussions

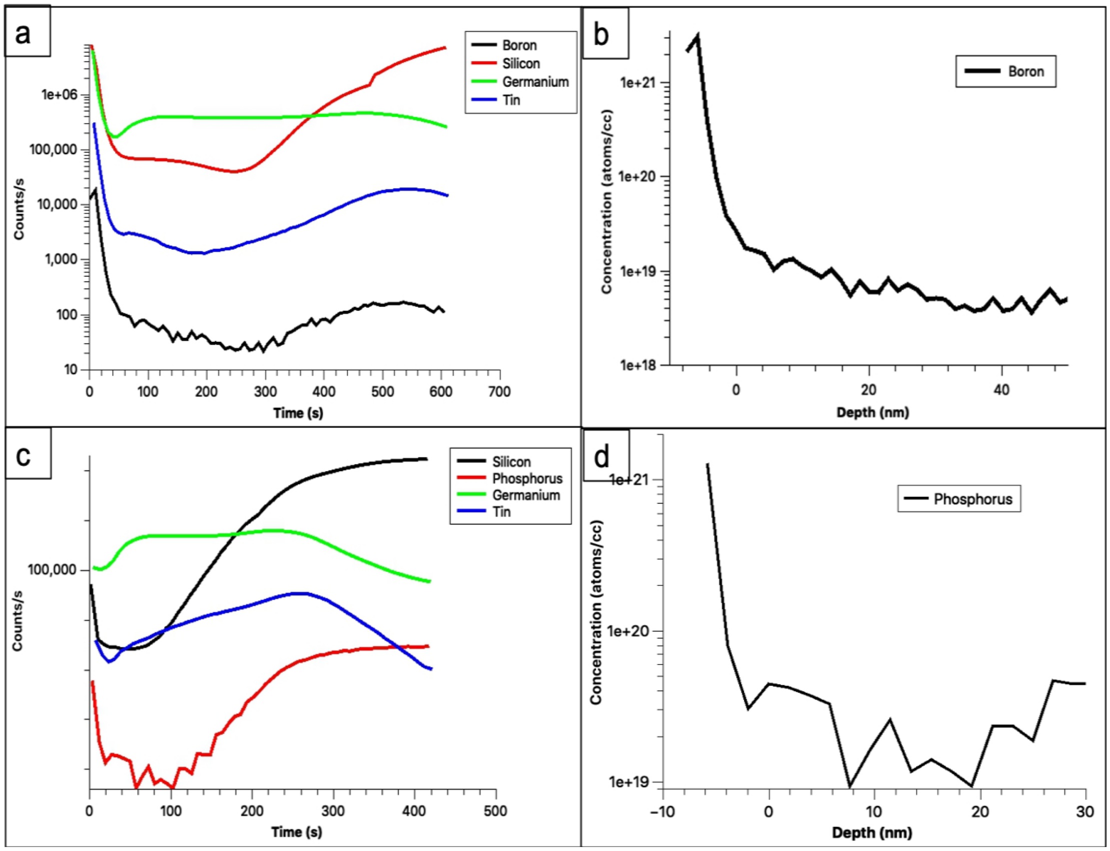

FIG. 5.5.1 (a) SIMS spectra and (b) boron concentration profile of GeSn films doped with diborane. (c) SIMS spectra and (d) phosphorus concentration profile of GeSn films doped with phosphine

The epitaxial deposition of the doped GeSn films was confirmed by XRD analysis (not shown here). Fig 5.5.1 shows the concentration profile spectra of GeSn films doped with boron and phosphorus and Table 5.5.1 gives the dopant concentration calculated from SIMS analysis achieved using different dopant gas flow rates. The dopant concentrations were calculated from the element counts data by obtaining the ratio of the dopant element counts to the Ge counts and multiplying it with the relative sensitivity factor (RSF) for the dopant element (Wilson 1995). It can be seen that high dopant concentrations (>10^{19} atoms/cc) can be achieved at low growth temperatures and low precursor flow rates using PECVD. This is due to the higher kinetic energy provided by the plasma for precursor dissociation. Also, the dopant concentration increases as the precursor flow rate increases. Thus, the doping level in the films can be tailored for various device applications by adjusting the precursor flows.

Table 5.5.1. Dopant concentrations achieved with different precursor flow rates

No.	Dopant gas	Dopant gas Flow rate (in sccm)	Dopant concentration observed by SIMS (in atoms/cm^3)
1	Diborane	20	1.49E19
2		60	2.4E19
3		150	1.45E20
4	Phosphine	20	4.2E19
5		60	6.34E19
6		150	9.23E19

Chapter 6 Modeling of device components based on Group IV semiconductors

The advancement of Si photonics requires the modeling of both optics (optical solutions of mode profile and propagation) and electro-optics (electron and hole carrier density and their response to applied voltage) of active components such as lasers and LEDs as well as passive components such as waveguides and resonators (Wirths, Buca, and Mantl 2016). Simulating the performance of these components offers the possibility to test hypothetical devices which have not (or could not) yet been manufactured and offers unique insight into device behavior by allowing the observation of phenomena that cannot be measured on real devices (Imtiaz, El-Ghazaly, and Grondin 1998). Device simulation helps users understand and depict the physical processes in a device and to make reliable predictions of the behavior of the next device generation. Two-dimensional device simulations with properly selected calibrated models and a very well-defined appropriate mesh structure are very useful for predictive parametric analysis of novel device structures. Two- and three-dimensional modeling and simulation processes help obtain a better understanding of the properties and behavior of new and current devices. This helps provide improved reliability and scalability, while also help to increase development speed and reduce risks and uncertainties.

Silvaco Atlas is a 2D and 3D device simulator that performs DC, AC, and transient analysis for silicon, binary, ternary, and quaternary material-based devices. The software is capable of simultaneously modeling both electrical and optical characteristics of material structures. It allows to solve yield and process variation problems for optimal combination of speed, power, density, breakdown, leakage, luminosity, and reliability. Optical modeling capabilities for all materials and layer structures include FDTD, transfer matrix method, ray tracing, and beam propagation. In addition to the in-built available materials' library (which include silicon, III-, II-VI, IV-IV semiconductors), it also allows for the addition of new materials by entering relevant material properties such as bandgap, dielectric constant, index of refraction, recombination coefficients and thus can be used to simulate devices based on a wide variety of materials.

Presently, two dimensional simulations of waveguides based on Ge and GeSn, photodiodes based on SiGe and GeSn and LEDs based on GeSn were performed using Silvaco Atlas for analysis of the optical performance and optimization of the device parameters such as device dimensions and material composition The simulation work (i.e script writing and executing the program) were primarily carried out by my colleague Todd Houghton.

6.1 Modeling of group IV-based waveguides

An optical waveguide is a physical structure that guides electromagnetic waves between two active components of an integrated circuit. Light is confined during transmission within the waveguide by total internal reflection (TIR). In order to prevent loss of optical power to the atmosphere or the substrate during transmission, the waveguide has to be designed based on a material such that its' index of refraction allows for TIR and the waveguide dimensions allow only the appropriate modes to be transmitted (i.e single mode vs multi-mode).

Silvaco Atlas features a comprehensive waveguide simulator which solves the vectoral 2D Helmholtz equation for waveguide cross sections. The optical and electrical constants required to solve this equation are available for the region of interest of a simulated waveguide. The simulator can solve for both TE and TM modes. Additionally, Atlas can compute solutions using user-defined materials by importing a user-edited optical property list.

Ge waveguides showing single mode and multi-mode transmission at an incident wavelength of 1550 and 5000 nm were modelled in order to carry out a systematic study of the effect of structure on the linear and nonlinear optical properties of the waveguides, as well as for the design of the optimal waveguide structure. The results of the simulation are given in Fig 6.1.1. It can be seen that as the number of transmission modes are increased, the loss of data to the surroundings also increase. Thus, from the simulations, the dimensions of the waveguides can be optimized for minimizing loss during light propagation. These simulations can then provide guidance of the thickness of the Ge film required for constructing waveguides that will eventually connect the GeSn/SiGeSn light emitters to the detectors on the same integrated Si photonic chip.

GeSn waveguides were modeled and simulated using Silvaco Atlas to optimize light confinement for increased propagation distance at a wavelength of 1900 nm. The results of the simulation are given in Fig 6.1.2. Materials for the core and cladding layers were assigned ($Ge_{88}Sn_{12}$ core with Si as substrate and air as cladding were used for the simulations). The material properties such as bandgap and index of refraction for GeSn were obtained from available literature. The height and width of the guide were varied systemically starting with a waveguide dimension of 2x2 μm. After each change in width or height, the simulation was re-run to observe the degree of optical confinement, maximum optical power, and intensity distribution within the guide. Waveguide designs were optimized to exhibit strong confinement of TE_{00} or TM_{00} mode intensity distribution as such designs have the potential to transfer light over long distances. It was seen that waveguides with thickness of 2 μm and 1 μm displayed TE_{11} and TE_{10} modes respectively. Such modes exhibit poor optical power transfer in the z direction for distances longer than λ and thus are not desired. Decreasing the thickness to 0.5 μm causes the waveguide to only accommodate the TE_{00} mode. However, with this thickness, some transmission loss occurs through the substrate. As a result, the thickness is increased to 0.6 μm which demonstrates optimal transmission.

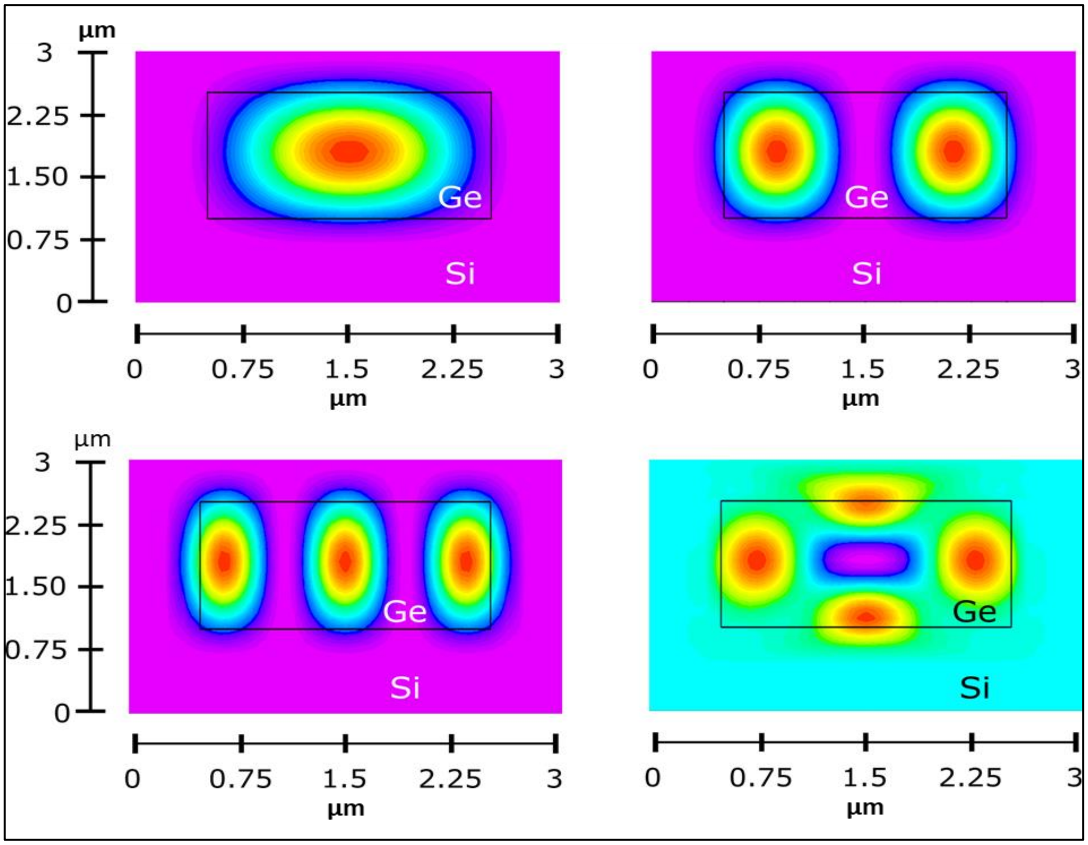

FIG. 6.1.1 (a-c) Various simulated optical mode cross-sections of 1550nm light confined to a Ge waveguide imbedded in bulk Si, from single mode to two and three modes, with the highest intensity being shown in red. The Ge core dimensions were 2μm in the horizontal direction and 1.5μm in the vertical direction. (d) A higher order mode can exist at longer wavelength of 5000 nm.

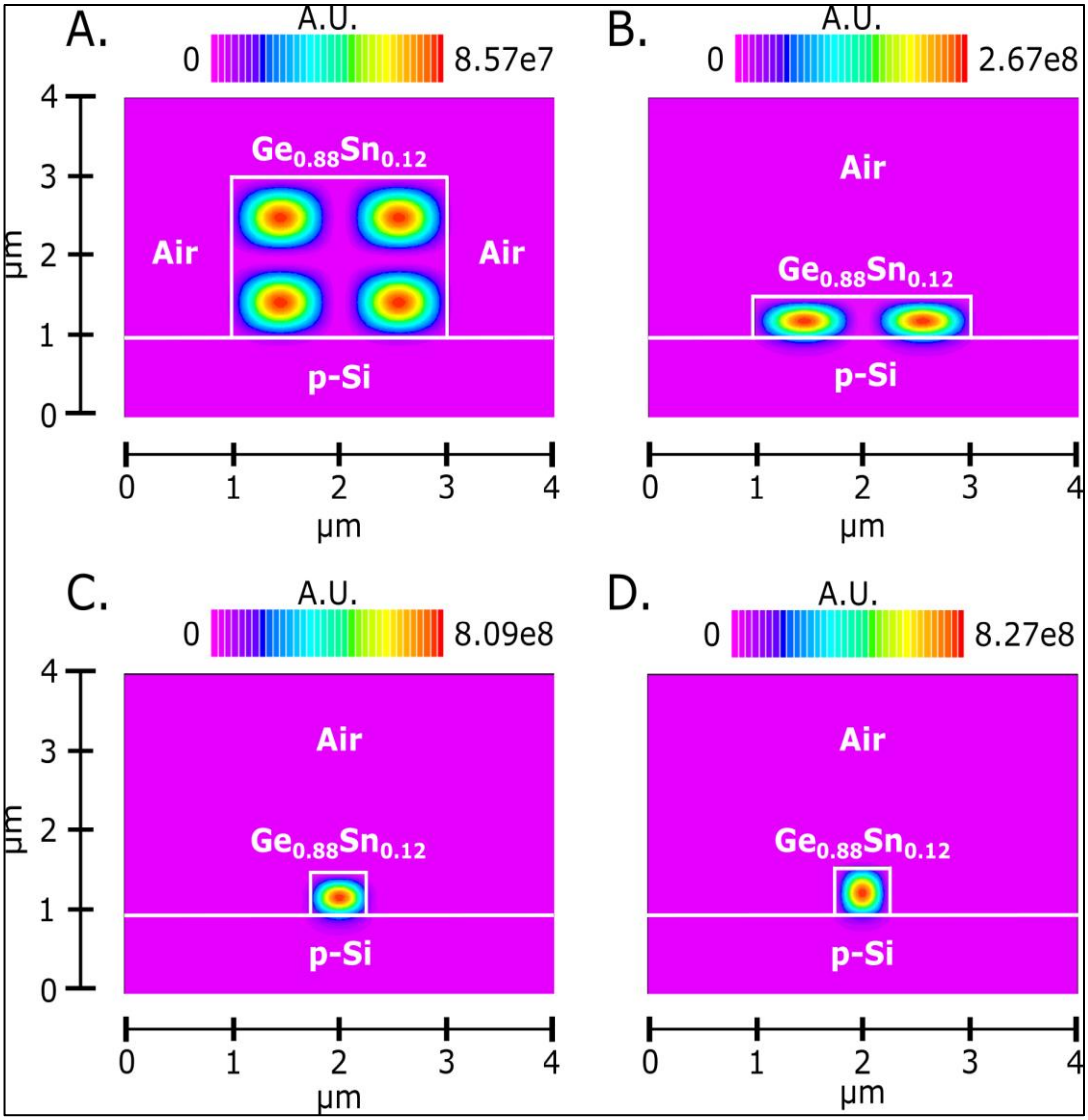

FIG. 6.1.2. Illustration of the waveguide mode-optimization process for an asymmetric $Ge_{0.88}Sn_{0.12}$ waveguide located on the surface of a p-type Si substrate with a doping concentration of $1*10^{16}cm^{-3}$. All images represent the waveguide's x,y cross-section with light λ=1900nm in wavelength propagating in the z direction and white lines denote interfaces between different materials. (A) starting waveguide geometry with a 2μm x 2μm $Ge_{0.88}Sn_{0.12}$ core showing a TE_{11} optical mode confined to the core region. (B) $Ge_{0.88}Sn_{0.12}$ core height reduced to 0.5μm, generating a TE_{10} mode with each lobe exhibiting an increase in maximum confined optical power compared to the TE_{11} case. (C) $Ge_{0.88}Sn_{0.12}$ core width is reduced to 0.5μm, producing a single TE_{00} mode and further increasing the optical power of the single lobe. (D) $Ge_{0.88}Sn_{0.12}$ core height increased to 0.6μm, reducing further increasing the maximum optical power of the TE_{00} mode while reducing the optical power lost to the p-Si substrate.

6.2 Modeling of group IV-based photodiodes

A photodiode is a semiconductor device that converts light into an electrical current through the photoelectric effect. When light with energy greater than the bandgap of the diode material is incident of the photodiode, it leads to the generation of electrons and holes in the material. The transport of these carriers to the electrodes causes a photocurrent to be generated in the devices. The photocurrent generated depends on the intensity and wavelength of the incident light and thus the device can be used for photodetection. A PIN diode, in which an undoped intrinsic semiconductor is sandwiched between a p-doped and n-doped semiconductor, is one of the most commonly used structures for photodiodes. This is because the undoped region allows for a larger depletion region than with a PN diode and thus can lead to photodiodes with higher sensitivity for incident light.

Two dimensional simulations of a SiGe PIN Diode photodetector was modeled using Silvaco Atlas. SiGe was initially used as the material parameters for SiGe are widely available in literature and established in the software library. The diode model consisted of three layers as shown in Figure 6.2.1. The i-layer was a 700 nm thick layer of SiGe while the p and n regions were 500 nm thick p-doped and n-doped Si. To gauge model effectiveness and assess results, a simulated collimated light source was used which is projected normal to the top (p-type Si) surface of the PIN diode. The PIN diode’s current vs. voltage characteristics were then modeled while varying the incoming intensity and wavelength parameters. It can be seen that the amount of photocurrent generated increases with increase in either the incident light wavelength or the incident light power. This is due to the larger number of carriers generated with increasing the energy or power of the incident light.

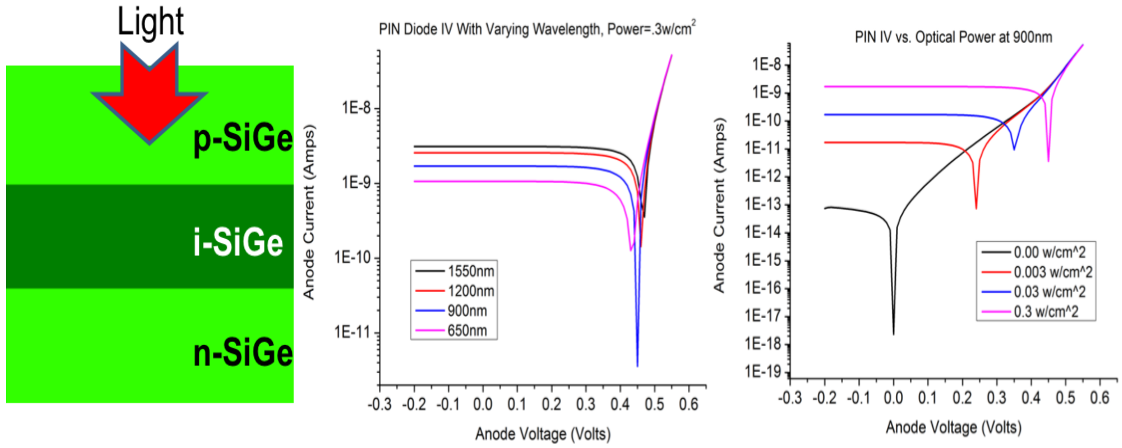

FIG. 6.2.1. Silvaco simulation of a PIN diode's response to light of different wavelength and intensity showing increase in photocurrent generation with increasing incident light wavelength or power

Next, 2D simulations of a GeSn based PIN Diode photodetector was modeled using Silvaco Atlas. The diode model consisted of three layers as shown in Fig 6.2.2 - a first layer of 500 nm thick and made of n-type silicon; a second layer made of $Ge_{88}Sn_{12}$; a third layer of 200 nm thick and made of p-type SiGeSn. Custom defined indices of refection, band gap energy and photogeneration rates (obtained from data available in literature) were added to the GeSn and SiGeSn layers to account for different composition ratios. The layer of n-type silicon is the anticipated CMOS substrate to be used in practice. Both the p-$Si_{10}Ge_{80}$ Sn_{10} and n-Si regions are doped to a concentration of $1*10^{18}$ cm^{-3}. The intensity and wavelength of light entering the device were set to $0.100 W/cm^2$ and 1900 nm for this simulation. The thickness of the GeSn layer was then optimized to maximize the carrier generation and photon absorption in the layer.

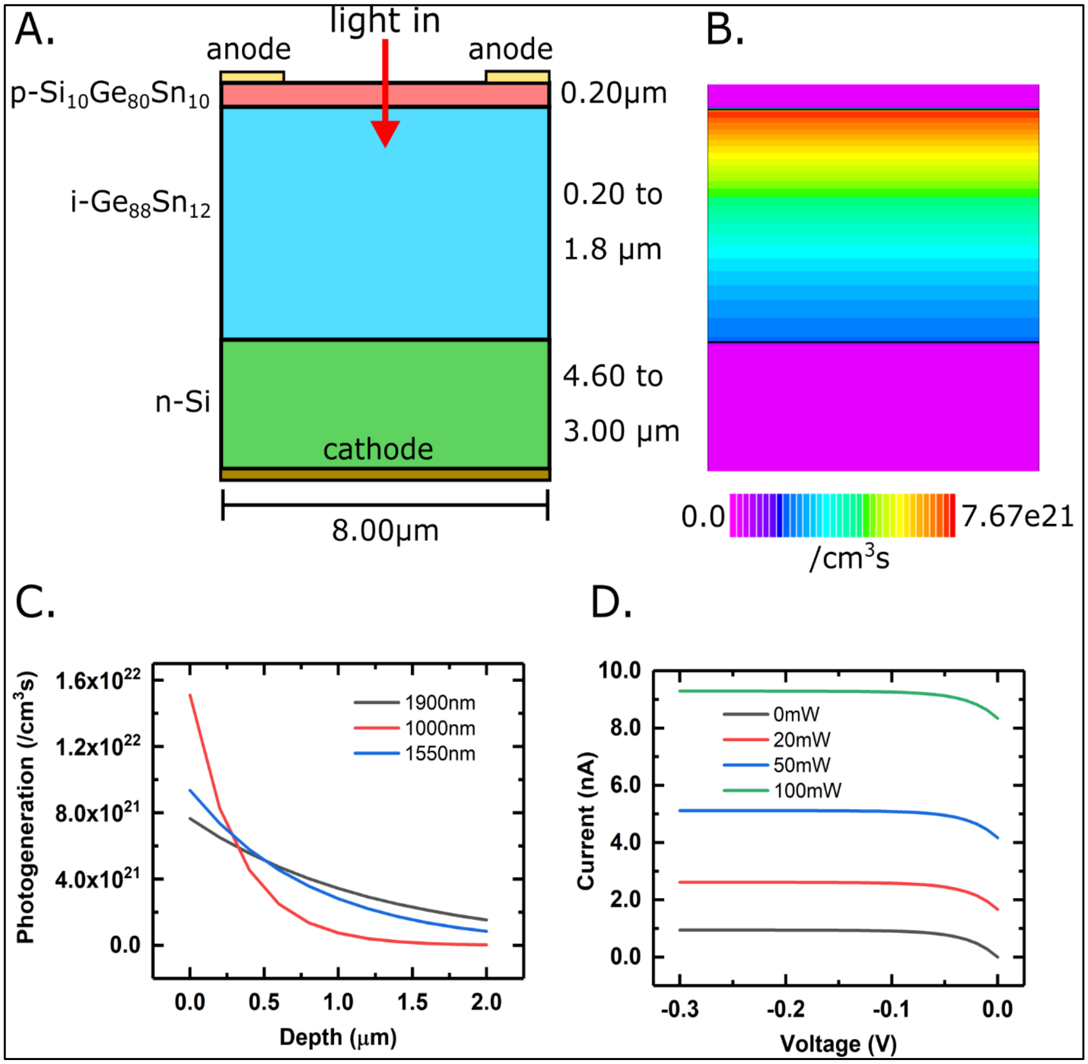

FIG. 6.2.2: (A) structure of PIN diode simulated in Silvaco Atlas. (B) photo-generation rate profile of the device, showing an exponential decrease in electron-hole pairs as light propagates deeper into a Ge_{88} Sn_{12} intrinsic region (C) plot of photogeneration vs. depth for various wavelengths of light entering a bulk layer of Ge_{88} Sn_{12}. (D) IV characteristics at various intensities of 1900nm light incident on the top surface of an optimized PIN diode structure under reverse bias.

The optimal thickness of the GeSn layer was found to be 1.60µm. It can be seen in Fig 6.2.2. c that the photogeneration is strongest at the top and decreases as the light propagates the material. This is because at the topmost of the photogenerated carriers reach the electrodes while deeper in to the material the carriers undergo recombination processes leading to a drop in the output. From the IV plot of the diode given in Fig 6.2.2 d, it can be seen that the observed photocurrent increases with increasing the power density of the incident light. This is due to the larger number of carriers generated with increasing the power of the incident light.

6.3 Modeling of group IV-based LEDs

LEDs are semiconductor devices which generate light when an electric current is passed through it. The current causes the electrons in the semiconductor to be excited to a higher energy level. When the electrons jump down back to the ground state level and recombine with holes, photons are released in the process with energy corresponding to the difference in energy between the excited state and ground state levels. Quantum wells based LEDS are an emerging technology for designing LEDS as in quantum wells the energy levels are discretized which results in higher device efficiency and smaller wavelength spread.

Silvaco Atlas allows for the simulation of photoemission from semiconductor materials after imputing relevant data such as radiative and non-radiative recombination rates, material bandgap and index of reflection. Because of this, it is possible to design light emitting materials using the software. Light emitted from a material is treated using the optical models included in Atlas.

GeSn-based LED devices were modeled using Silvaco device simulation software. Quantum well devices were simulated in which $Ge_{0.88}Sn_{0.12}$ film was the well layer and $Si_{0.1}Ge_{0.8}Sn_{0.1}$ film was the barrier material, grown on a Si substrate as shown in

Fig 6.3.1. The values needed for the simulation such as bandgap, recombination coefficient and dielectric constant were obtained from available literature. The software used models such as K.P model and Fermi model that provided simulated I-V curve, carrier concentration vs voltage plots, optical power density vs wavelength and 2D device emission simulations. The simulations were performed for various device parameters such as Sn concentration and film layer thicknesses to optimize the radiative recombination in the well region. With the K.P. and Fermi models enabled, it was found that quantum wells larger than 20nm are sub-optimal for photon generation due to the separation of the electron and hole wavefunctions. It was also found that wells smaller than 7 nm result in a weak, two-peak emission spectra due to significant wavefunction penetration into the surrounding SiGeSn buffer layers. A well thickness of approximately 10 nm provides good electron and hole wavefunction overlap without large portions of the wavefunction tails present in the non-emitting SiGeSn buffer regions. From Fig 6.3.1 e, it can be seen that the maximum spectral power density is obtained at ~2.5 μm which corresponds with the bandgap of $Ge_{0.88}Sn_{0.12}$. Thus, the emission wavelength can be varied by varying device parameters such as GeSn composition and well film thickness.

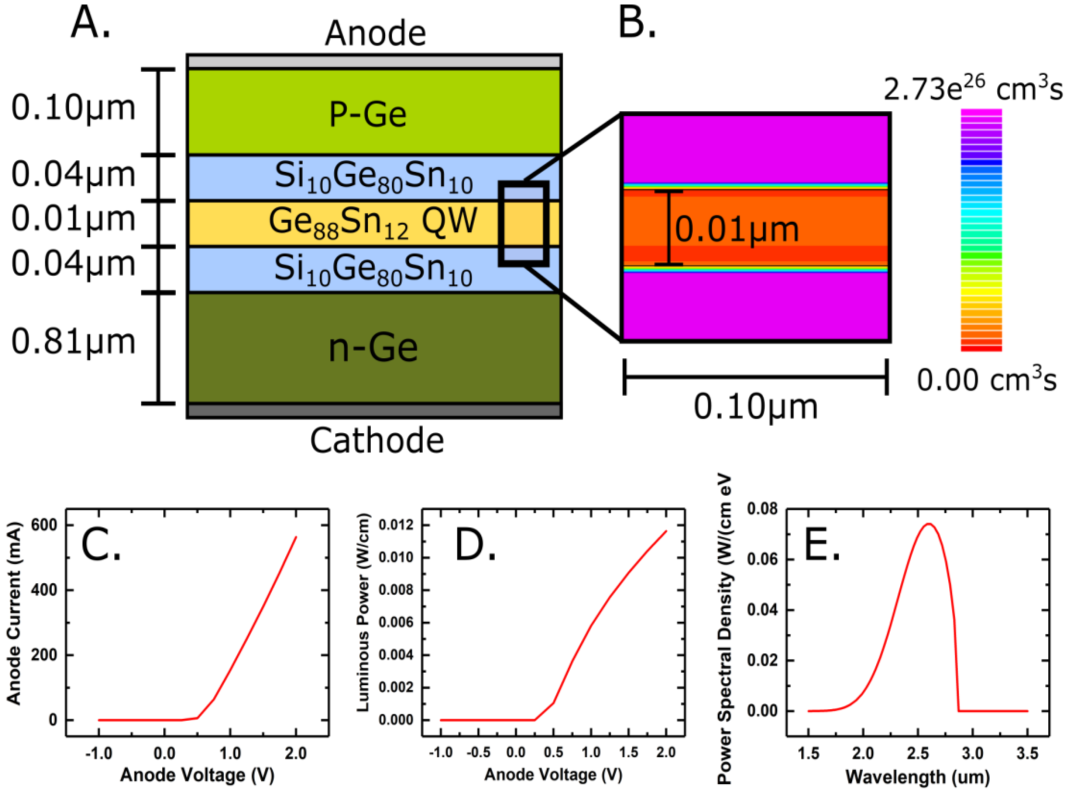

FIG. 6.3.1. (A) Depiction of LED device layer cross-section for achieving single-band emission from a 10nm thick $Ge_{88}Sn_{12}$ quantum well. (B) Depiction of radiative recombination inside the 10nm quantum well layer at an input voltage of 2V, with a small degree of recombination taking place in surrounding $Si_{10}Ge_{20}Sn_{10}$ barrier due to wave function tails. (C) IV curve of a simulated 1cm x 1cm areal LED device. (D) luminous power normalized across a 1cm x 1cm areal device at the 2.6μm peak wavelength vs anode voltage. (E) emission spectrum of simulated 1cm x 1cm areal LED device.

Chapter 7 Conclusions and Future Work

7.1 Conclusions

In this dissertation, Ge, GeSn and SiGeSn thin films were deposited using in-house assembled simplified PECVD reactors. The reactor assembly included a reaction quartz chamber, a gas injection provision and a vacuum assembly. Reactor No. 1 was assembled using a quartz tube, two inlets for Sn and Ge+Si precursor gases injection and a mechanical vacuum pump. Reactor No. 2 improved upon the design of Reactor No. 1 by having a larger quartz tube, an industrial showerhead, an induction heating set-up and a susceptor rotation assembly.

Polycrystalline SiGeSn thin films on bare Si substrates were achieved using Reactor No. 1 for deposition. The films were polycrystalline due to non-UHV conditions present during the growth of the films. SiGeSn thin films up to 8% were demonstrated at growth temperatures of 350^{o}C. This was achieved by using a composition graded approach to reduce the strain developed in the SiGeSn films from the lattice mismatch between SiGeSn and Si substrate. Films were also grown on insulating substrates – sapphire and silicon dioxide and it was seen that the choice of substrate did not affect the composition of the deposited films provided other growth conditions remain the same. Selective area growth (SAG) of the SiGeSn films was also achieved by depositing films on patterned Si substrates. The selectively grown films were used to fabricate basic photodetectors and the fabricated devices exhibited enhanced current generation under IR illumination and a photogenerated to dark current value of ~10 and thus and can be utilized as IR photodetectors.

Polycrystalline Ge and SiGeSn thin films were achieved using Reactor No. 2 for deposition. The films were polycrystalline due to non-UHV conditions present during the growth of the films. Plasma enhancement was shown to result in a higher rate of film deposition (2-3 times higher) without affecting the material quality of the grown films and thus can be useful for low temperature growth. Rapid thermal annealing of the Ge films at high temperatures (>900^{o}C) resulted in the formation of epitaxial films. SiGeSn thin films up to 7% were attained at growth temperatures of 350^{o}C. This was achieved by using either Ge buffer films as virtual substrates or using digermane as the Ge precursor source. No film growth was observed when using high precursor pressures of stannic chloride due to the production of HCl and Cl_2 etchants during $SnCl_4$ dissociation and the lower dissociation energy of $SnCl_4$ than Ge precursors.

Epitaxial Ge and GeSn thin films were achieved by modifying Reactor No. 2 to include a turbomolecular pump in its' vacuum assembly and by adopting a rigorous ex-situ chemical cleaning process. Higher film growth rates could be achieved with Ge_2H_6 than GeH_4 as Ge precursor due to the lower dissociation energy of digermane. Improvement in the film material quality was observed with increasing Ge precursor partial pressure due to higher growth rates. GeSn thin films up to 0.2 - 3% were attained at growth temperatures of 300^{o}C by systematic varying of the Ge/Sn precursor ratio. The GeSn films were doped with boron and phosphorus by flowing diborane and phosphine respectively along with the Ge and Sn precursors during film growth. High dopant concentration in the range of 10^{19} – 10^{20} atoms/cm^3 were demonstrated at low growth temperatures and low precursor flow rates using PECVD.

7.2 Future works

Based on the results of the dissertation work, the following suggestion are offered for future growth of group IV alloys using the PECVD reactor.

1. Since $SnCl_4$ decomposes to a greater extent in the presence of plasma, a remote plasma facility should be incorporated in which only the Ge and Si precursors are subjected to plasma so as to dissociate them before introducing them in the main growth chamber along with the Sn precursor.
2. Since digermane has a higher dissociation rate than germane at lower temperatures, using it as the Ge precursor for GeSn/ SiGeSn growth is recommended.
3. Since depositing GeSn/SiGeSn in multiple steps with increasing Sn flow rates leads to higher Sn incorporation, graded growth should be studied more.
4. A longer quartz tube should be used in order to minimize the induction between the induction heating coils and the showerhead and flanges so as to prevent the heating and pre-reacting of the precursors before reaching the substrate.
5. Incorporation of in-situ monitors such as Lay Tec, k-space and Filmetrix to measure reflectivity, roughness, thickness of the film and temperature process to provide real time feedback of the growth of the thin films will be beneficial.
6. Using a susceptor of a larger dimeter in order to achieve better coupling between the susceptor and induction coils will help to reach higher temperatures at lower powers. It will also lead to film deposition over a larger substrate size.

Bibliography

Aella, P., C. Cook, J. Tolle, S. Zollner, A. V.G. Chizmeshya, and J. Kouvetakis. 2004. “Optical and Structural Properties of Si XSn YGe 1-x-y Alloys.” *Applied Physics Letters* 84 (6): 888–90. https://doi.org/10.1063/1.1645324.

Alharthi, Bader, Wei Dou, Perry C. Grant, Joshua M. Grant, Timothy Morgan, Aboozar Mosleh, Wei Du, et al. 2019. “Low Temperature Epitaxy of High-Quality Ge Buffer Using Plasma Enhancement via UHV-CVD System for Photonic Device Applications.” *Applied Surface Science* 481 (March): 246–54. https://doi.org/10.1016/j.apsusc.2019.03.062.

Alharthi, Bader, Joshua M. Grant, Wei Dou, Perry C. Grant, Aboozar Mosleh, Wei Du, Mansour Mortazavi, Baohua Li, Hameed Naseem, and Shui Qing Yu. 2018. “Heteroepitaxial Growth of Germanium-on-Silicon Using Ultrahigh-Vacuum Chemical Vapor Deposition with RF Plasma Enhancement.” *Journal of Electronic Materials* 47 (8): 4561–70. https://doi.org/10.1007/s11664-018-6315-5.

Alharthi, Bader, Joe Margetis, Huong Tran, Sattar Al-kabi, Wei Dou, Seyed Amir Ghetmiri, Aboozar Mosleh, et al. 2017. “Study of Material and Optical Properties of Si_xGe_1-x-YSn_y Alloys for Si-Based Optoelectronic Device Applications.” *Optical Materials Express* 7 (10): 3517. https://doi.org/10.1364/ome.7.003517.

Aly, S. A., and Alaa A. Akl. 2015. “Influence of Film Thickness on Optical Absorption and Energy Gap of Thermally Evaporated CdS0.1Se0.9 Thin Films.” *Chalcogenide Letters* 12 (10): 489–96.

Asafa, T B. 2013. “Influence of Deposition Temperature and Pressure on Structural and Electrical Properties of Boron Doped Poly-Si 13 Ge 87 Films Grown by Chemical Vapour Deposition.” *Nanoscience and Nanotechnology* 3 (5): 123–29. https://doi.org/10.5923/j.nn.20130305.03.

Asano, Takanori, Tatsuya Terashima, Takashi Yamaha, Masashi Kurosawa, Wakana Takeuchi, Noriyuki Taoka, Osamu Nakatsuka, and Shigeaki Zaima. 2015. “Epitaxial Growth and Crystalline Properties of Ge1-x-YSixSny on Ge(0 0 1) Substrates.” *Solid-State Electronics* 110: 49–53. https://doi.org/10.1016/j.sse.2015.01.006.

Attiaoui, Anis, and Oussama Moutanabbir. 2014. “Indirect-to-Direct Band Gap Transition in Relaxed and Strained Ge 1-x-y Si x Sn y Ternary Alloys.” *Journal of Applied Physics* 116 (6). https://doi.org/10.1063/1.4889926.

Aubin, J., J. M. Hartmann, M. Bauer, and S. Moffatt. 2016. “Very Low Temperature Epitaxy of Ge and Ge Rich SiGe Alloys with Ge2H6 in a Reduced Pressure - Chemical Vapour Deposition Tool.” *Journal of Crystal Growth* 445: 65–72. https://doi.org/10.1016/j.jcrysgro.2016.04.018.

Aubin, J., J. M. Hartmann, A. Gassenq, J. L. Rouviere, E. Robin, V. Delaye, D. Cooper, N. Mollard, V. Reboud, and V. Calvo. 2017. “Growth and Structural Properties of Step-Graded, High Sn Content GeSn Layers on Ge.” *Semiconductor Science and Technology* 32 (9). https://doi.org/10.1088/1361-6641/aa8084.

Bauer, Matthew, Cole Ritter, P. A. Crozier, Jie Ren, J. Menendez, G. Wolf, and J. Kouvetakis. 2003. “Synthesis of Ternary SiGeSn Semiconductors on Si(100) via Sn XGe1-x Buffer Layers.” *Applied Physics Letters* 83 (11): 2163–65. https://doi.org/10.1063/1.1606104.

Beeler, R. T., J. Menéndez, D. J. Smith, and J. Kouvetakis. 2012. “High Performance Group IV Photodiodes with Tunable Absorption Edges Based on Ternary SiGeSn Alloys.” *ECS Transactions* 50 (9): 591–99. https://doi.org/10.1149/05009.0591ecst.

Blagov, A. E., A. L. Vasiliev, A. S. Golubeva, I. A. Ivanov, O. A. Kondratev, Yu V. Pisarevsky, M. Yu Presnyakov, P. A. Prosekov, and A. Yu Seregin. 2014. “Study of the Structural Quality of Heteroepitaxial Silicon-on-Sapphire Structures by High-Resolution X-Ray Diffraction, X-Ray Reflectivity, and Electron Microscopy.” *Crystallography Reports* 59 (3): 315–22. https://doi.org/10.1134/S1063774514030043.

Camacho-Aguilera, Rodolfo E., Yan Cai, Neil Patel, Jonathan T. Bessette, Marco Romagnoli, Lionel C. Kimerling, and Jurgen Michel. 2012. “An Electrically Pumped Germanium Laser.” *Optics Express* 20 (10): 11316. https://doi.org/10.1364/oe.20.011316.

Cariou, R., R. Ruggeri, X. Tan, Giovanni Mannino, J. Nassar, and P. Roca I Cabarrocas. 2014. “Structural Properties of Relaxed Thin Film Germanium Layers Grown by Low Temperature RF-PECVD Epitaxy on Si and Ge (100) Substrates.” *AIP Advances* 4 (7). https://doi.org/10.1063/1.4886774.

Casalino, Maurizio, Giuseppe Coppola, Mario Iodice, Ivo Rendina, and Luigi Sirleto. 2010. “Near-Infrared Sub-Bandgap All-Silicon Photodetectors: State of the Art and Perspectives.” *Sensors* 10 (12): 10571–600. https://doi.org/10.3390/s101210571.

Chang, Guo En, Shu Wei Chang, and Shun Lien Chuang. 2010. “Strain-Balanced GezSn1-z-SixGe YSn1-x-y Multiple-Quantum-Well Lasers.” *IEEE Journal of Quantum Electronics* 46 (12): 1813–20. https://doi.org/10.1109/JQE.2010.2059000.

D’Costa, V. R., J. Tolle, C. D. Poweleit, J. Kouvetakis, and J. Menéndez. 2007. “Compositional Dependence of Raman Frequencies in Ternary Ge1-x-y Six Sny Alloys.” *Physical Review B - Condensed Matter and Materials Physics* 76 (3): 1–9. https://doi.org/10.1103/PhysRevB.76.035211.

Dash, W. C., and R. Newman. 1955. “Intrinsic Optical Absorption in Single-Crystal Germanium and Silicon at 77Â°K and 300Â°K.” *Physical Review* 99 (4): 1151–55. https://doi.org/10.1103/PhysRev.99.1151.

Den Driesch, N. Von, D. Stange, S. Wirths, G. Mussler, B. Holländer, Z. Ikonic, J. M. Hartmann, et al. 2015. “Direct Bandgap Group IV Epitaxy on Si for Laser Applications.” *Chemistry of Materials* 27 (13): 4693–4702. https://doi.org/10.1021/acs.chemmater.5b01327.

den Driesch, Nils von, Daniela Stange, Stephan Wirths, Denis Rainko, Ivan Povstugar, Aleksei Savenko, Uwe Breuer, et al. 2017. “SiGeSn Ternaries for Efficient Group IV Heterostructure Light Emitters.” *Small* 13 (16): 1–9. https://doi.org/10.1002/smll.201603321.

Dismukes, J. P., L. Ekstrom, and R. J. Paff. 1964. “Lattice Parameter and Density in Germanium-Silicon Alloys.” *Journal of Physical Chemistry* 68 (10): 3021–27. https://doi.org/10.1021/j100792a049.

Dou, Wei, Bader Alharthi, Perry C. Grant, Joshua M. Grant, Aboozar Mosleh, Huong Tran, Wei Du, et al. 2018. “Crystalline GeSn Growth by Plasma Enhanced Chemical Vapor Deposition.” *Optical Materials Express* 8 (10): 3220. https://doi.org/10.1364/ome.8.003220.

Dou, Wei, Mourad Benamara, Aboozar Mosleh, Joe Margetis, Perry Grant, Yiyin Zhou, Sattar Al-Kabi, et al. 2018. “Investigation of GeSn Strain Relaxation and Spontaneous Composition Gradient for Low-Defect and High-Sn Alloy Growth.” *Scientific Reports* 8 (1): 1–11. https://doi.org/10.1038/s41598-018-24018-6.

Du, W., S. Al-Kabi, S. A. Ghetmiri, H. Tran, T. Pham, B. Alharthi, A. Mosleh, et al. 2016. “Development of SiGeSn Technique towards Mid-Infrared Devices in Silicon Photonics.” *ECS Transactions* 75 (8): 231–39. https://doi.org/10.1149/07508.0231ecst.

Eres, Gyula, and J. W. Sharp. 1993. “The Role of Hydride Coverage in Surface-Limited Thin-Film Growth of Epitaxial Silicon and Germanium.” *Journal of Applied Physics* 74 (12): 7241–50. https://doi.org/10.1063/1.355014.

Fang, Cizhe, Yan Liu, Yibo Wang, Jibao Wu, Genquan Han, Yao Shao, Jincheng Zhang, and Yue Hao. 2018. “Buffer-Free GeSn with High Relaxation Degree Grown on Si(001) Substrate for Photodetection.” *IEEE Photonics Journal* 10 (6): 1–9. https://doi.org/10.1109/JPHOT.2018.2873734.

Fensham, P. J. 1955. “The Thermal Decomposition of Germane. II. Mechanism.” *Journal of Physical Chemistry* 59 (9): 806–8. https://doi.org/10.1021/j150531a002.

Fischer, Inga A., Torsten Wendav, Lion Augel, Songchai Jitpakdeebodin, Filipe Oliveira, Alessandro Benedetti, Stefan Stefanov, et al. 2015. "Growth and Characterization of SiGeSn Quantum Well Photodiodes." *Optics Express* 23 (19): 25048. https://doi.org/10.1364/oe.23.025048.

Fournier-Lupien, J. H., D. Chagnon, P. Lévesque, A. A. AlMutairi, S. Wirths, E. Pippel, G. Mussler, et al. 2014. "In Situ Studies of Germanium-Tin and Silicon-Germanium-Tin Thermal Stability." *ECS Transactions* 64 (6): 903–11. https://doi.org/10.1149/06406.0903ecst.

Fournier-Lupien, J. H., S. Mukherjee, S. Wirths, E. Pippel, N. Hayazawa, G. Mussler, J. M. Hartmann, P. Desjardins, D. Buca, and O. Moutanabbir. 2013. "Strain and Composition Effects on Raman Vibrational Modes of Silicon-Germanium-Tin Ternary Alloys." *Applied Physics Letters* 103 (26). https://doi.org/10.1063/1.4855436.

Gallagher, J. D., Chi Xu, Liying Jiang, John Kouvetakis, and José Menéndez. 2013. "Fundamental Band Gap and Direct-Indirect Crossover in Ge 1-x-YSixSny Alloys." *Applied Physics Letters* 103 (20). https://doi.org/10.1063/1.4829621.

Gamble, H. S., B. M. Armstrong, P. T. Baine, Y. H. Low, P. V. Rainey, Y. W. Low, D. W. McNeill, S. J N Mitchell, J. H. Montgomery, and F. H. Ruddell. 2008. "Germanium on Sapphire Substrates for System on a Chip." *Materials Science in Semiconductor Processing* 11 (5): 195–98. https://doi.org/10.1016/j.mssp.2008.09.011.

Gencarelli, F., B. Vincent, L. Souriau, O. Richard, W. Vandervorst, R. Loo, M. Caymax, and M. Heyns. 2012. "Low-Temperature Ge and GeSn Chemical Vapor Deposition Using Ge 2H 6." *Thin Solid Films* 520 (8): 3211–15. https://doi.org/10.1016/j.tsf.2011.10.119.

Grant, Perry C., Wei Dou, Bader Alharthi, Joshua M. Grant, Aboozar Mosleh, Wei Du, Baohua Li, Mansour Mortazavi, Hameed A. Naseem, and Shui-Qing Yu. 2017. "Comparison Study of the Low Temperature Growth of Dilute GeSn and Ge." *Journal of Vacuum Science & Technology B, Nanotechnology and Microelectronics: Materials, Processing, Measurement, and Phenomena* 35 (6): 061204. https://doi.org/10.1116/1.4990773.

Grant, Perry C., Wei Dou, Bader Alharthi, Joshua M. Grant, Huong Tran, G. Abernathy, Aboozar Mosleh, et al. 2019. " UHV-CVD Growth of High Quality GeSn Using SnCl 4 : From Material Growth Development to Prototype Devices ." *Optical Materials Express* 9 (8): 3277. https://doi.org/10.1364/ome.9.003277.

Greve, D W. 1998. "UHV / CVD and Related Growth Techniques for Si and Other Materials," no. October: 1–20. http://www.ece.cmu.edu/~dwg.

Harris, Thomas R., Mee Yi Ryu, Yung Kee Yeo, Richard T. Beeler, and John Kouvetakis. 2014. “Electrical Characterization Studies of P-Type Ge, Ge1-YSn y, and Si0.09Ge0.882Sn0.028 Grown on n-Si Substrates.” *Current Applied Physics* 14 (SUPPL. 1): S123–28. https://doi.org/10.1016/j.cap.2013.11.009.

Hartmann, J.-M., J. Aubin, and J.-P. Barnes. 2016. “A Benchmark of Germane and Digermane for the Low Temperature Growth of Intrinsic and Heavily In-Situ Boron-Doped SiGe.” *ECS Transactions* 75 (8): 281–93. https://doi.org/10.1149/07508.0281ecst.

Huang, Y., E. K. Tien, S. Gao, S. K. Kalyoncu, Q. Song, F. Qian, E. Adas, D. Yildirim, and O. Boyraz. 2011. “Electrical Signal-to-Noise Ratio Improvement in Indirect Detection of Mid-IR Signals by Wavelength Conversion in Silicon-on-Sapphire Waveguides.” *Applied Physics Letters* 99 (18): 1–4. https://doi.org/10.1063/1.3651292.

Imtiaz, S. M.Sohel, Samir M. El-Ghazaly, and Robert O. Grondin. 1998. “Advantages of Semiconductor Device Simulator Combining Electromagnetic and Electron Transport Models.” *VLSI Design* 8 (1–4): 495–500. https://doi.org/10.1155/1998/85608.

Ishii, Hiromu, Yasuo Takahashi, and Junichi Murota. 1985. “Selective Ge Deposition on Si Using Thermal Decomposition of GeH 4.” *Applied Physics Letters* 47 (8): 863–65. https://doi.org/10.1063/1.96011.

Jiang, Liying, Chi Xu, James D. Gallagher, Ruben Favaro, Toshi Aoki, José Menéndez, and John Kouvetakis. 2014. “Development of Light Emitting Group IV Ternary Alloys on Si Platforms for Long Wavelength Optoelectronic Applications.” *Chemistry of Materials* 26 (8): 2522–31. https://doi.org/10.1021/cm403801b.

Jo, Gae Hun, Sun Ho Kim, and Jung Hyuk Koh. 2018. “Enhanced Electrical and Optical Properties Based on Stress Reduced Graded Structure of Al-Doped ZnO Thin Films.” *Ceramics International* 44 (1): 735–41. https://doi.org/10.1016/j.ceramint.2017.09.240.

Johnson, Robb A., Paul R. De La Houssaye, Charles E. Chang, Pin Fan Chen, Michael E. Wood, Graham A. Garcia, Isaac Lagnado, and Peter M. Asbeck. 1998. “Advanced Thin-Film Silicon-on-Sapphire Technology: Microwave Circuit Applications.” *IEEE Transactions on Electron Devices* 45 (5): 1047–54. https://doi.org/10.1109/16.669525.

Kasper, E., J. Werner, M. Oehme, S. Escoubas, N. Burle, and J. Schulze. 2012. “Growth of Silicon Based Germanium Tin Alloys.” *Thin Solid Films* 520 (8): 3195–3200. https://doi.org/10.1016/j.tsf.2011.10.114.

Khazaka, Rami, Emmanuel Nolot, Joris Aubin, and Jean Michel Hartmann. 2018. “Growth and Characterization of SiGeSn Pseudomorphic Layers on 200 Mm Ge Virtual Substrates.” *Semiconductor Science and Technology* 33 (12). https://doi.org/10.1088/1361-6641/aaea32.

Kil, Yeon Ho, Sim Hoon Yuk, Joung Hee Kim, Taek Sung Kim, Yong Tae Kim, Chel Jong Choi, and Kyu Hwan Shim. 2016. “The Low Temperature Epitaxy of Ge on Si (1 0 0) Substrate Using Two Different Precursors of GeH4 and Ge2H6.” *Solid-State Electronics* 124: 35–41. https://doi.org/10.1016/j.sse.2016.07.027.

Kim, Hyun Jung, Yeonjoon Park, Hyung Bin Bae, and Sang H. Choi. 2015. “High-Electron-Mobility SiGe on Sapphire Substrate for Fast Chipsets.” *Advances in Condensed Matter Physics* 2015: 785415. https://doi.org/10.1155/2015/785415.

Kim, Munho, Wenjuan Fan, Jung Hun Seo, Namki Cho, Shih Chia Liu, Dalong Geng, Yonghao Liu, et al. 2015. “Polycrystalline GeSn Thin Films on Si Formed by Alloy Evaporation.” *Applied Physics Express* 8 (6). https://doi.org/10.7567/APEX.8.061301.

Kobayashi, Shin ichi, Min Lin Cheng, Armin Kohlhase, Taketoshi Sato, Junichi Murota, and Nobou Mikoshiba. 1990. “Selective Germanium Epitaxial Growth on Silicon Using CVD Technology with Ultra-Pure Gases.” *Journal of Crystal Growth* 99 (1–4): 259–62. https://doi.org/10.1016/0022-0248(90)90523-N.

Lager, G. A., J. D. Jorgensen, and F. J. Rotella. 1982. “Crystal Structure and Thermal Expansion of α-Quartz SiO2 at Low Temperatures.” *Journal of Applied Physics* 53 (10): 6751–56. https://doi.org/10.1063/1.330062.

Li, F., S. Jackson, E. Magi, C. Grillet, S. J. Madden, Y. Moghe, A. Read, et al. 2011. “Low Propagation Loss Silicon-on-Sapphire Nanowires for the Mid-IR.” *Optics InfoBase Conference Papers* 19 (16): 971–73.

Littlejohns, C. G., A. Z. Khokhar, D. J. Thomson, Y. Hu, L. Basset, S. A. Reynolds, G. Z. Mashanovich, G. T. Reed, and F. Y. Gardes. 2015. “Ge-on-Si Plasma-Enhanced Chemical Vapor Deposition for Low-Cost Photodetectors.” *IEEE Photonics Journal* 7 (4). https://doi.org/10.1109/JPHOT.2015.2456069.

Liu, Zhi, Bu Wen Cheng, Ya Ming Li, Chuan Bo Li, Chun Lai Xue, and Qi Ming Wang. 2013. “Effects of High Temperature Rapid Thermal Annealing on Ge Films Grown on Si(001) Substrate.” *Chinese Physics B* 22 (11). https://doi.org/10.1088/1674-1056/22/11/116804.

Luan, Hsin Chiao, Desmond R. Lim, Kevin K. Lee, Kevin M. Chen, Jessica G. Sandland, Kazumi Wada, and Lionel C. Kimerling. 1999. “High-Quality Ge Epilayers on Si with Low Threading-Dislocation Densities.” *Applied Physics Letters* 75 (19): 2909–

11. https://doi.org/10.1063/1.125187.

Margetis, Joe, Aboozar Mosleh, Seyed Amir Ghetmiri, Sattar Al-Kabi, Wei Dou, Wei Du, Nupur Bhargava, et al. 2017. “Fundamentals of Ge1−xSnx and SiyGe1−x-YSnx RPCVD Epitaxy.” *Materials Science in Semiconductor Processing* 70 (December 2016): 38–43. https://doi.org/10.1016/j.mssp.2016.12.024.

Margetis, Joe, Shui-Qing Yu, Baohua Li, and John Tolle. 2019. “ Chemistry and Kinetics Governing Hydride/Chloride Chemical Vapor Deposition of Epitaxial Ge 1−x Sn X .” *Journal of Vacuum Science & Technology A* 37 (2): 021508. https://doi.org/10.1116/1.5055620.

Moontragoon, P., R. A. Soref, and Z. Ikonic. 2012. “The Direct and Indirect Bandgaps of Unstrained Si XGe 1-x-YSn y and Their Photonic Device Applications.” *Journal of Applied Physics* 112 (7). https://doi.org/10.1063/1.4757414.

Mosleh, A., M. A. Alher, L. Cousar, H. Abusafe, W. Dou, P. Grant, S. Al-Kabi, et al. 2015. “Enhancement of Material Quality of (Si)GeSn Films Grown by SnCl4 Precursor.” *ECS Transactions* 69 (5): 279–86. https://doi.org/10.1149/06905.0279ecst.

Mosleh, Aboozar. 2015. “Epitaxial Growth of Si-Ge-Sn Alloys for Optoelectronic Device Application.” University of Arkansas.

Mosleh, Aboozar, Murtadha Alher, Larry C. Cousar, Wei Du, Seyed Amir Ghetmiri, Sattar Al-Kabi, Wei Dou, et al. 2016. “Buffer-Free GeSn and SiGeSn Growth on Si Substrate Using In Situ SnD4 Gas Mixing.” *Journal of Electronic Materials* 45 (4): 2051–58. https://doi.org/10.1007/s11664-016-4402-z.

Mosleh, Aboozar, Murtadha Alher, Wei Du, Larry C. Cousar, Seyed Amir Ghetmiri, Sattar Al-Kabi, Wei Dou, et al. 2016. “ Si y Ge 1−x−y Sn x Films Grown on Si Using a Cold-Wall Ultrahigh-Vacuum Chemical Vapor Deposition System .” *Journal of Vacuum Science & Technology B, Nanotechnology and Microelectronics: Materials, Processing, Measurement, and Phenomena* 34 (1): 011201. https://doi.org/10.1116/1.4936892.

Moto, K., N. Saitoh, N. Yoshizawa, T. Suemasu, and K. Toko. 2019. “Solid-Phase Crystallization of Densified Amorphous GeSn Leading to High Hole Mobility (540 Cm2/V S).” *Applied Physics Letters* 114 (11). https://doi.org/10.1063/1.5088847.

Oehl, N., L. Hardenberg, M. Knipper, J. Kolny-Olesiak, J. Parisi, and T. Plaggenborg. 2015. “Critical Size for the β- to α-Transformation in Tin Nanoparticles after Lithium Insertion and Extraction.” *CrystEngComm* 17 (19): 3695–3700. https://doi.org/10.1039/c5ce00148j.

Ohmura, Takuma, Takashi Yamaha, Masashi Kurosawa, Wakana Takeuchi, Mitsuo

Sakashita, Noriyuki Taoka, Osamu Nakatsuka, and Shigeaki Zaima. 2015. “Mobility Behavior of Polycrystalline $Si_{1\text{-}x\text{-}y}Ge_xSn_y$ Grown on Insulators.” *Transactions of the Materials Research Society of Japan* 40 (4): 351–54. https://doi.org/10.14723/tmrsj.40.351.

Olubuyide, Oluwamuyiwa O., David T. Danielson, Lionel C. Kimerling, and Judy L. Hoyt. 2006. “Impact of Seed Layer on Material Quality of Epitaxial Germanium on Silicon Deposited by Low Pressure Chemical Vapor Deposition.” *Thin Solid Films* 508 (1–2): 14–19. https://doi.org/10.1016/j.tsf.2005.06.120.

Park, Yeonjoon, Glen C. King, and Sang H. Choi. 2008. “Rhombohedral Epitaxy of Cubic SiGe on Trigonal C-Plane Sapphire.” *Journal of Crystal Growth* 310 (11): 2724–31. https://doi.org/10.1016/j.jcrysgro.2008.02.010.

Peng, Ying, Lei Miao, Jie Gao, Chengyan Liu, Masashi Kurosawa, Osamu Nakatsuka, and Shigeaki Zaima. 2019. “Realizing High Thermoelectric Performance at Ambient Temperature by Ternary Alloying in Polycrystalline Si1-x-YGexSny Thin Films with Boron Ion Implantation.” *Scientific Reports* 9 (1): 1–9. https://doi.org/10.1038/s41598-019-50754-4.

Roucka, Radek, Andrew Clark, Nam Pham, and Barbara Landini. 2015. “Si-Ge-Sn Based Compound Semiconductors for Photonic Applications.” In *CS MANTECH 2015 - 2015 International Conference on Compound Semiconductor Manufacturing Technology*, 359–62. Scottsdale.

Roucka, Radek, Andrew Clark, Tom Wilson, Tomos Thomas, Markus Führer, Nicholas Ekins-Daukes, Andrew Johnson, Rick Hoffman, and David Begarney. 2016. “Demonstrating Dilute-Tin Alloy SiGeSn for Use in Multijunction Photovoltaics: Single- and Multijunction Solar Cells with a 1.0-EV SiGeSn Junction.” *IEEE Journal of Photovoltaics* 6 (4): 1025–30. https://doi.org/10.1109/JPHOTOV.2016.2559785.

Schulte-Braucks, C., N. Von Den Driesch, S. Glass, A. T. Tiedemann, U. Breuer, A. Besmehn, J. M. Hartmann, et al. 2016. “Low Temperature Deposition of High-k/Metal Gate Stacks on High-Sn Content (Si)GeSn-Alloys.” *ACS Applied Materials and Interfaces* 8 (20): 13133–39. https://doi.org/10.1021/acsami.6b02425.

Schwartz, Peter V. 1992. “OXYGEN INCORPORATION DURING LOW - TEMPERATURE CHEMICAL VAPOR DEPOSmON AND ITS EFFECTS ON THE ELECTRONIC PROPERTIES OF EPITA XIAL Si AND Sil-XGex FILMS,” no. October.

Sedky, Sherif, Paolo Fiorini, Matty Caymax, Stefano Loreti, Kris Baert, Lou Hermans, and Robert Mertens. 1998. “Structural and Mechanical Properties of Polycrystalline Silicon Germanium for Micromachining Applications.” *Journal of*

Microelectromechanical Systems 7 (4): 365–72. https://doi.org/10.1109/84.735343.

Senftleben, Oliver, Hermann Baumgärtner, and Ignaz Eisele. 2008. “Cleaning of Silicon Surfaces for Nanotechnology.” *Materials Science Forum* 573–574: 77–117. https://doi.org/10.4028/www.scientific.net/msf.573-574.77.

Shimura, Yosuke, Takanori Asano, Takashi Yamaha, Masahiro Fukuda, Wakana Takeuchi, Osamu Nakatsuka, and Shigeaki Zaima. 2017. “EXAFS Study of Local Structure Contributing to Sn Stability in SiyGe1-y-ZSnz.” *Materials Science in Semiconductor Processing* 70 (November 2016): 133–38. https://doi.org/10.1016/j.mssp.2016.11.013.

Soref, Richard. 2010. “Mid-Infrared Photonics in Silicon and Germanium.” *Nature Photonics* 4 (8): 495–97. https://doi.org/10.1038/nphoton.2010.171.

———. 2014. “Silicon-Based Silicon – Germanium – Tin Heterostructure Photonics Subject Areas : Author for Correspondence :” *Philosophical Transactions of the Royal Society A* 372: 20130113. https://doi.org/10.1098/rsta.2013.0113.

Stefanov, S., J. C. Conde, A. Benedetti, C. Serra, J. Werner, M. Oehme, J. Schulze, and S. Chiussi. 2012. “Laser Assisted Formation of Binary and Ternary Ge/Si/Sn Alloys.” *Thin Solid Films* 520 (8): 3262–65. https://doi.org/10.1016/j.tsf.2011.10.101.

Takahashi, Kouta, Hiroshi Ikenoue, Mitsuo Sakashita, Osamu Nakatsuka, Shigeaki Zaima, and Masashi Kurosawa. 2019. “Operation of Thin-Film Thermoelectric Generator of Ge-Rich Poly-Ge1-XSnx on SiO2 Fabricated by a Low Thermal Budget Process.” *Applied Physics Express* 12 (5): 8–13. https://doi.org/10.7567/1882-0786/ab1969.

Takeuchi, Wakana, Noriyuki Taoka, Masashi Kurosawa, Mitsuo Sakashita, Osamu Nakatsuka, and Shigeaki Zaima. 2015. “High Hole Mobility Tin-Doped Polycrystalline Germanium Layers Formed on Insulating Substrates by Low-Temperature Solid-Phase Crystallization.” *Applied Physics Letters* 107 (2): 022103. https://doi.org/10.1063/1.4926507.

Talochkin, A. B., V. A. Timofeev, A. K. Gutakovskii, and V. I. Mashanov. 2017. “Sn – Induced Decomposition of SiGeSn Alloys Grown on Si by Molecular-Beam Epitaxy.” *Journal of Crystal Growth* 478: 205–11. https://doi.org/10.1016/j.jcrysgro.2017.09.005.

Teh, L. K., W. K. Choi, L. K. Bera, and W. K. Chim. 2001. “Structural Characterisation of Polycrystalline SiGe Thin Film.” *Solid-State Electronics* 45 (11): 1963–66. https://doi.org/10.1016/S0038-1101(01)00241-6.

Thomson, David J., Callum G. Littlejohns, Steven Stanković, Milos Nedeljkovic, and

Scott A. Reynolds. 2015. “Silicon Photonics.” Edited by John G. Webster. *Wiley Encyclopedia of Electrical and Electronics Engineering*. https://doi.org/10.1002/047134608X.W8287.

Tsai, Julie A., and Rafael Reif. 1995. “Polycrystalline Silicon–Germanium Films on Oxide Using Plasma- enhanced Very- low- pressure Chemical Vapor Deposition.” *Applied Physics Letters* 66 (14): 1809–11. https://doi.org/10.1063/1.113329.

Wilson, R. G. 1995. “SIMS Quantification in Si, GaAs, and Diamond - an Update.” *International Journal of Mass Spectrometry and Ion Processes* 143 (C): 43–49. https://doi.org/10.1016/0168-1176(94)04136-U.

Wirths, S., D. Buca, Z. Ikonic, P. Harrison, A. T. Tiedemann, B. Holländer, T. Stoica, et al. 2014. “SiGeSn Growth Studies Using Reduced Pressure Chemical Vapor Deposition towards Optoelectronic Applications.” *Thin Solid Films* 557: 183–87. https://doi.org/10.1016/j.tsf.2013.10.078.

Wirths, S., D. Buca, and S. Mantl. 2016. “Si-Ge-Sn Alloys: From Growth to Applications.” *Progress in Crystal Growth and Characterization of Materials* 62 (1): 1–39. https://doi.org/10.1016/j.pcrysgrow.2015.11.001.

Wong, Chi Yan, Zhenzhou Cheng, Xia Chen, Ke Xu, Christy K Y Fung, Yi Min Chen, and Hon Ki Tsang. 2012. “Characterization of Mid-Infrared Silicon-on-Sapphire Microring Resonators with Thermal Tuning.” *IEEE Photonics Journal* 4 (4): 1095–1102. https://doi.org/10.1109/JPHOT.2012.2204734.

Xie, Junqi, Andrew V.G. Chizmeshya, John Tolle, Vijay R. Dcosta, Jose Menendez, and John Kouvetakis. 2010. “Synthesis, Stability Range, and Fundamental Properties of Si-Ge-Sn Semiconductors Grown Directly on Si(100) and Ge(100) Platforms.” *Chemistry of Materials* 22 (12): 3779–89. https://doi.org/10.1021/cm100915q.

Yamaha, Takashi, Masashi Kurosawa, Takuma Ohmura, Wakana Takeuchi, Noriyuki Taoka, Osamu Nakatsuka, and Shigeaki Zaima. 2015. “Effect of Sn on Crystallinity and Electronic Property of Low Temperature Grown Polycrystalline-Si1-x-YGexSny Layers on SiO2.” *Solid-State Electronics* 110: 54–58. https://doi.org/10.1016/j.sse.2015.01.005.

Yeh, Wenchang, Akihiro Matsumoto, Keisuke Sugihara, and Hisataka Hayase. 2014. “Sputter Epitaxial Growth of Flat Germanium Film with Low Threading-Dislocation Density on Silicon (001).” *ECS Journal of Solid State Science and Technology* 3 (10): Q195–99. https://doi.org/10.1149/2.0091410jss.

Zaima, S., O. Nakatsuka, T. Yamaha, T. Asano, S. Ike, A. Suzuki, M. Kurosawa, W. Takeuchi, and M. Sakashita. 2015. “Challenges of Energy Band Engineering with New Sn-Related Group IV Semiconductor Materials for Future Integrated Circuits.”

ECS Transactions 69 (10): 89–98. https://doi.org/10.1149/06910.0089ecst.

Zhang, Lu, Hai Yang Hong, Yi Sen Wang, Cheng Li, Guang Yang Lin, Song Yan Chen, Wei Huang, and Jian Yuan Wang. 2017. “Formation of High-Sn Content Polycrystalline GeSn Films by Pulsed Laser Annealing on Co-Sputtered Amorphous GeSn on Ge Substrate.” *Chinese Physics B* 26 (11): 1–5. https://doi.org/10.1088/1674-1056/26/11/116802.

Zheng, Jun, Suyuan Wang, Tianwei Zhou, Yuhua Zuo, Buwen Cheng, and Qiming Wang. 2015. “Single-Crystalline Ge_1-X_-YSixSny Alloys on Si (100) Grown by Magnetron Sputtering.” *Optical Materials Express* 5 (2): 287. https://doi.org/10.1364/ome.5.000287.

Zhou, Yiyin, Wei Dou, Wei Du, Thach Pham, Seyed Amir Ghetmiri, Sattar Al-Kabi, Aboozar Mosleh, et al. 2016. “Systematic Study of GeSn Heterostructure-Based Light-Emitting Diodes towards Mid-Infrared Applications.” *Journal of Applied Physics* 120 (2): 1–8. https://doi.org/10.1063/1.4958337.